

# Synchrotron-Based Infrared Spectrum of Oxetane

by

Omar Mahassneh

A Thesis submitted to the Faculty of Graduate Studies of

The University of Manitoba

in partial fulfilment of the requirements of the degree of

MASTER OF SCIENCE

Department of Chemistry

University of Manitoba

Winnipeg

Copyright© 2016 by Omar Mahassneh

## Abstract

The rovibrational spectrum of oxetane (c-C<sub>3</sub>H<sub>6</sub>O) was measured between 400 cm<sup>-1</sup> and 1180 cm<sup>-1</sup> using the far-infrared beamline at the Canadian Light Source (CLS) with a resolution of 0.00096 cm<sup>-1</sup>. Analysis of this spectrum shows that the low frequency vibration ring puckering mode ( $\nu_{18}$ ) at 53 cm<sup>-1</sup> couples with the other modes, which has consequences on the spectrum of higher frequency vibrations: many hot and combination bands appear in this region in addition to significant perturbations due to Coriolis interactions. The distinguished rotational structure of the observed bands allowed their assignment confidently and reveals bands unseen in the low resolution infrared spectrum. Chapter 2 provides a description of the experimental and theoretical techniques used in this work. Chapter 3 discusses the analysis of the spectrum between 700 cm<sup>-1</sup> and 900 cm<sup>-1</sup> including the ring deformation fundamental ( $\nu_8$ ) and combination bands of the ring puckering ( $\nu_{18}$ ) and the  $\beta$ -CH<sub>2</sub>-rocking ( $\nu_{17}$ ) modes that were first recognized in this work. In Chapter 4, the preliminary rovibrational analysis of the C-O asymmetric stretch ( $\nu_{23}$ ) at 1008 cm<sup>-1</sup>, two hot bands and also perturbations in  $\nu_{23}$  are discussed. Chapter 5 discusses the rovibrational analysis of the C-C symmetric stretch ( $\nu_6$ ) at 1033 cm<sup>-1</sup> and the analysis of the Coriolis interactions of this band with  $\nu_{23}$ . Chapter 6 describes the analysis of the Coriolis interactions between ( $\nu_{23}$ ) and C-C asymmetric stretch hot band ( $\nu_{18} + \nu_{24} - \nu_{18}$ ) at 944 cm<sup>-1</sup> and a global fit of these two bands and the  $\nu_6$  band. Analysis of the Coriolis interactions in this study represents the first perturbation analysis in oxetane, which gives an idea about the effect of Coriolis interactions among other states in this molecule. This

work tells us what to anticipate in the spectrum of molecules that have low frequency modes.

## **Acknowledgments**

I would like to express my gratitude to my supervisor Dr. Jennifer van Wijngaarden for your expertise, wisdom and the great support you provided to me since day one in your lab, not only in building research skills but also to benefit from the student life at the University of Manitoba.

I would like to thank my advisory committee Dr. Philip Hultin and Dr. Michael Gericke for your valuable feedback.

Also, I would like to thank Dr. Brant Billingham, the far-infrared beamline scientist, at the Canadian Light Source for your help with recording the high resolution spectrum of oxetane.

I would like to thank the current and past Dr. van Wijngaarden group members for the great discussions in the group Seminars.

## Table of Contents

Abstract.....	I
Acknowledgments.....	III
Table of Contents.....	IV
List of Figures.....	VIII
List of Tables.....	XII
Chapter 1. Introduction.....	1
1.1 Spectroscopy of oxetane .....	5
1.2 Rovibrational spectroscopy.....	10
1.2.1 Rotational energy levels of asymmetric tops .....	10
1.2.2 Centrifugal distortion .....	13
1.2.3 Vibrational spectroscopy of diatomic molecules .....	14
1.2.4 Vibrational spectroscopy of polyatomic molecules .....	15
1.2.5 Selection rules of rovibrational transitions in asymmetric tops .....	16
1.2.6 Combination differences.....	18
1.2.7 Coriolis interactions in molecules .....	19
References.....	22
Chapter 2. High resolution Fourier transform infrared (FTIR) spectroscopy of oxetane.....	25
2.1 High resolution spectroscopy.....	25
2.1.1 Michelson interferometer.....	25
2.1.2 Light Source (Synchrotron Radiation).....	27

2.1.2.1 How does a synchrotron work? .....	28
2.1.2.2 Synchrotron advantage.....	28
2.2 Experimental details.....	29
2.3 Structure of the rotational resolved infrared spectrum.....	33
2.4 Previous studies on the low resolution infrared spectrum of oxetane.....	35
2.5 Frequency calculations.....	37
References.....	40
Chapter 3: Analysis of bands located between 700 and 900 cm <sup>-1</sup> .....	42
3.1 Introduction.....	42
3.2 General procedure for the rovibrational analysis.....	43
3.3 Analysis of the combination bands between the ring puckering ( $\nu_{18}$ ) and the $\beta$ -CH <sub>2</sub> -rocking ( $\nu_{17}$ ) modes .....	48
3.3.1 The combination band $\nu_{17}+\nu_{18}$ .....	49
3.3.2 The hot combination band $\nu_{17}+2\nu_{18} - \nu_{18}$ .....	51
3.3.3 The combination band $\nu_{17}+3\nu_{18} - 2\nu_{18}$ .....	53
3.3.4 The combination band $\nu_{17}+4\nu_{18} - 3\nu_{18}$ .....	54
3.4 Analysis of the ring deformation fundamental band ( $\nu_8$ ).....	56
3.5 Summary.....	59
References.....	60
Chapter 4: Preliminary analysis of C-O asymmetric stretch fundamental ( $\nu_{23}$ ) at 1008 cm <sup>-1</sup> and its hot bands $\nu_{23}$ , $\nu_{18}+\nu_{23} - \nu_{18}$ and $2\nu_{18}+\nu_{23} - 2\nu_{18}$ .....	61
4.1 Introduction.....	61
4.2 Assignment of the C-O asymmetric stretch fundamental ( $\nu_{23}$ ).....	61

4.3 Analysis of the C-O asymmetric stretch hot bands $\nu_{18} + \nu_{23} - \nu_{18}$ and $2\nu_{18} + \nu_{23} - 2\nu_{18}$ .....	64
4.4 Perturbations in the C-O asymmetric stretch fundamental.....	69
4.5 Summary.....	70
References.....	72
Chapter 5 Coriolis interaction between the fundamental vibrations: C-O asymmetric stretch ( $\nu_{23}$ ) at $1008\text{ cm}^{-1}$ and the C-C symmetric stretch ( $\nu_6$ ) at $1033\text{ cm}^{-1}$ .....	
5.1 Introduction .....	73
5.2 Preliminary analysis of the C-C symmetric stretch fundamental ( $\nu_6$ ) .....	74
5.2.1 Perturbations in the C-C symmetric stretch fundamental ( $\nu_6$ ) band .....	75
5.3 Analysis of the Coriolis interactions between the C-O asymmetric stretch fundamental ( $\nu_{23}$ ) and the C-C symmetric stretch ( $\nu_6$ ) .....	77
5.4 Summary.....	81
References.....	82
Chapter 6: Global analysis of perturbations in the C-O asymmetric stretch ( $\nu_{23}$ ), C-C symmetric stretch ( $\nu_6$ ) and the C-C asymmetric stretch hot band ( $\nu_{18} + \nu_{24} - \nu_{18}$ ).....	
6.1 Introduction .....	83
6.2 Candidates for the lower perturbing state .....	83
6.2.1 The C-C asymmetric stretch fundamental ( $\nu_{24}$ ) and the hot band ( $\nu_{18} + \nu_{24} - \nu_{18}$ )..	83
6.2.2 The C-O symmetric stretch fundamental ( $\nu_7$ ) and the hot band ( $\nu_7 + \nu_{18} - \nu_{18}$ ).....	85
6.3 Analysis of the Coriolis interactions between the C-O asymmetric stretch fundamental ( $\nu_{23}$ ) and the C-C asymmetric stretch hot band ( $\nu_{18} + \nu_{24} - \nu_{18}$ ).....	88

6.4 Global analysis.....	90
6.5 Summary .....	94
References.....	95
Chapter 7: Summary and future work .....	96
References.....	101

## List of Figures

Figure 1.1: The potential functions along the ring puckering coordinates of azetidine, silacyclobutane and 3-oxetanone showing the energy ( $\text{cm}^{-1}$ ) as a function of the ring puckering coordinate. The quantum numbers of vibration are labeled on the right.....	4
Figure 1.2: The ring puckering coordinate defined for a four membered ring.....	5
Figure 1.3: Principal inertial axis system is defined by the planar geometry of oxetane...	6
Figure 1.4: The potential well for the ring puckering vibration of oxetane showing the energy ( $\text{cm}^{-1}$ ) as a function of the dimensionless coordinate $\chi$ . The quantum numbers of vibration are labeled on the right.....	7
Figure 1.5: Moment of inertia in a rigid two body rotor.....	11
Figure 1.6: Examples of symmetric and asymmetric tops.....	12
Figure 1.7: Schematic of P, Q and R branches for a diatomic molecule where rotational energies are $J$ dependent only. If the $\Delta J=0$ transitions (Q-branch) were allowed they appear as a single sharp peak .....	17
Figure 1.8: Schematic of a GSCD from a $b$ -type band. For example, for upper level ( $v=1$ ) rotational state $J_{K_a K_c}$ of $10_0 10$ , there are P-branch and R-branch transitions that originate in lower level ( $v=0$ ) rotational state $11_1 11$ and $9_1 9$ that end in this common state.....	18
Figure 1.9: Coriolis interactions between the two degenerate components of $\nu_2$ mode of $\text{H}_3^+$ molecule.....	20
Figure 2.1: A schematic diagram of a Michelson interferometer configured for FTIR spectroscopy.....	26

Figure 2.2: High resolution infrared spectrum of oxetane at 10 mTorr between 738 and 824 $\text{cm}^{-1}$ at room temperature.....	31
Figure 2.3: High resolution infrared spectrum of oxetane at 200 mTorr between 724 and 783 $\text{cm}^{-1}$ at room temperature, in which the contour of the <i>a</i> -type band $\nu_{17}+\nu_{18}$ at 754 $\text{cm}^{-1}$ is shown.....	33
Figure 2.4: A magnified portion of the spectrum in Fig (2.3). Strong transitions in the P-branch are labeled with the quantum numbers $J_{K_a K_c}$ of the lower and the higher levels.....	34
Figure 2.5: A magnified portion of the spectrum in Fig (2.2). A progression in the Q-branch is labeled with the quantum numbers $J_{K_a K_c}$ of the lower and the higher levels.....	35
Figure 3.1: High resolution infrared spectrum of oxetane at 200 mTorr. These bands represent combinations between the ring puckering ( $\nu_{18}$ ) at 53 $\text{cm}^{-1}$ , ( $2\nu_{18}$ ) at 142 $\text{cm}^{-1}$ , ( $3\nu_{18}$ ) at 247 $\text{cm}^{-1}$ and ( $4\nu_{18}$ ) at 365 $\text{cm}^{-1}$ , and the $\beta$ -CH <sub>2</sub> -rocking ( $\nu_{17}$ ) motion at 702 $\text{cm}^{-1}$ .....	44
Figure 3.2: High resolution spectrum of oxetane showing the ring puckering fundamental and hot bands.....	43
Figure 3.3: A simulation of the combination band ( $\nu_{17}+\nu_{18}$ ) at 754 $\text{cm}^{-1}$ , showing a part of a pattern with common $K_a$ values in the P-branch using PGOPHER.....	45
Figure 3.4: A Loomis-Wood Plot showing progressions in the P-branch of the combination band ( $\nu_{17}+\nu_{18}$ ) at 754 $\text{cm}^{-1}$ . The colours correspond to peaks labelled in Fig (3.3) that are part of a common $K_a$ progression.....	46

Figure 3.5: Spectral assignment in Igor Pro. The windows show part of a progression in the P-branch (left) and the corresponding R-branch (right) in the $\nu_{23}$ band. The transitions are doubly degenerate in $K_a$ which is reflected in the labels which are $J K_a K_c$ (upper vibrational state) $J K_a K_c$ (lower vibrational state).....	47
Figure 3.6: A schematic energy level diagram explaining the vibrational assignment of the bands in Fig (3.1).....	48
Figure 3.7: A comparison between the simulated and experimental transitions in a small region of the Q and P-branches of the $\nu_{17}+\nu_{18}$ band.....	51
Figure 3.8: High resolution infrared spectrum of oxetane at 10 mTorr showing the bands $\nu_7, \nu_7+\nu_{18} - \nu_{18}$ and $\nu_8$ . The features involving $\nu_7$ and $\nu_7+\nu_{18} - \nu_{18}$ will be discussed in Chapter6.....	56
Figure 4.1: High resolution infrared spectrum of oxetane at 5 mTorr. In this region, the bands $\nu_{23}, \nu_{18}+\nu_{23} - \nu_{18}$ and $2\nu_{18}+\nu_{23} - 2\nu_{18}$ were rovibrationally analyzed.....	62
Figure 4.2: A schematic energy diagram explaining the vibrational assignment of the bands: $\nu_{23}, \nu_{18}+\nu_{23} - \nu_{18}$ and $2 \nu_{18}+\nu_{23} - 2\nu_{18}$ .....	65
Figure 4.3: A comparison between the simulation and the spectrum of the $\nu_{23}, \nu_{18}+\nu_{23} - \nu_{18}$ and $2\nu_{18} +\nu_{23} - 2\nu_{18}$ bands.....	68
Figure 4.4: LW plot of the high resolution infrared spectrum of oxetane between 1021 and $1031\text{cm}^{-1}$ in which progressions of rovibrational transitions in the fundamental $\nu_{23}$ are highlighted.....	69
Figure 5.1: High resolution infrared spectrum of oxetane recorded at 180 mTorr which shows the $\nu_6$ band that overlaps with subset of bands in Fig (4.1).....	73

Figure 5.2: LW plot of the high resolution infrared spectrum of oxetane between 1047 and 1056cm <sup>-1</sup> showing progressions of rovibrational transitions in the $\nu_6$ fundamental.....	76
Figure 5.3: Coriolis forces acting on the two nondegenerate modes: symmetric C-C stretch ( $\nu_6$ ) and asymmetric C-O stretch ( $\nu_{23}$ ).....	76
Figure 5.4: Reduced energies (cm <sup>-1</sup> ) of levels with quantum number $J \leq 60$ and $K_a \leq 5$ of the states $\nu_{23}$ at 1008 cm <sup>-1</sup> and $\nu_6$ at 1033 cm <sup>-1</sup> .....	78
Figure 6.1: High resolution infrared spectrum of oxetane recorded at 5 mTorr which shows the $\nu_7$ band subset of bands of the $\nu_{23}$ mode. ....	84
Figure 6.2: Reduced energies (cm <sup>-1</sup> ) of levels with quantum number $J \leq 60$ and $K_a \leq 6$ of the states $\nu_7$ at 908 cm <sup>-1</sup> $\nu_{23}$ at 1008 cm <sup>-1</sup> .....	87
Figure 6.3: Reduced energies (cm <sup>-1</sup> ) of levels with quantum number $J \leq 60$ and $K_a \leq 6$ of the states $\nu_{18}+\nu_{24}$ at 997 cm <sup>-1</sup> $\nu_{23}$ at 1008 cm <sup>-1</sup> .....	90
Figure 6.4: A comparison between the simulated and the observed spectrum of the $\nu_{23}$ band without including the Coriolis interactions terms in the model Hamiltonian used.....	91
Figure 6.5: A comparison between the simulated and the observed spectrum of the $\nu_{23}$ band after including the Coriolis interactions terms in the model Hamiltonian used.....	93

## List of Tables

Table (2.1): Experimental parameters of the high resolution infrared spectra of oxetane measurements at the CLS.....	32
Table (2.2): Frequency calculations of oxetane fundamental bands ( $\text{cm}^{-1}$ ) compared with the experimental values.....	36
Table (2.3): Assigned combination and hot bands of oxetane, in the region of study.....	39
Table (3.1): Spectroscopic constants ( $\text{cm}^{-1}$ ) for the ground state and excited state ( $\nu_{17}+\nu_{18}$ ).....	50
Table (3.2): Spectroscopic constants ( $\text{cm}^{-1}$ ) of $\nu_{18}$ and $\nu_{17}+2\nu_{18}$ states.....	52
Table (3.3): Spectroscopic constants ( $\text{cm}^{-1}$ ) of the $\nu_{17}+3\nu_{18}$ and $2\nu_{18}$ states .....	54
Table (3.4): Spectroscopic constants ( $\text{cm}^{-1}$ ) of the $3\nu_{18}$ and $\nu_{17}+4\nu_{18}$ states.....	55
Table (3.5): Spectroscopic constants ( $\text{cm}^{-1}$ ) for the ground state and $\nu_8$ state.....	57
Table (4.1): Spectroscopic constants ( $\text{cm}^{-1}$ ) for the ground state and $\nu_{23}$ states.....	63
Table (4.2): Spectroscopic constants ( $\text{cm}^{-1}$ ) for the $\nu_{18} + \nu_{23}$ and $\nu_{18}$ states.....	66
Table (4.3): Spectroscopic constants ( $\text{cm}^{-1}$ ) for the $2\nu_{18} + \nu_{23}$ and $2\nu_{18}$ states.....	67
Table (5.1): Spectroscopic constants ( $\text{cm}^{-1}$ ) for the ground state and $\nu_6$ state.....	75
Table (5.2): Spectroscopic constants ( $\text{cm}^{-1}$ ) for the ground state, $\nu_6$ and $\nu_{23}$ states following treatment of the Coriolis interaction.....	80
Table (6.1): Spectroscopic constants ( $\text{cm}^{-1}$ ) for the ground and $\nu_7$ states.....	86
Table (6.2): Spectroscopic constants ( $\text{cm}^{-1}$ ) for the $\nu_7+\nu_{18}$ and $\nu_{18}$ states.....	88

Table (6.3): Spectroscopic constants ( $\text{cm}^{-1}$ ) for the G.S.,  $\nu_{18}$ ,  $\nu_{18+\nu_{24}}$ ,  $\nu_{23}$ , and  $\nu_6$  of oxetane.....92

## Chapter 1. Introduction

In spectroscopy, the interaction between electromagnetic radiation and matter is studied. Molecules could absorb energy from radiation by interacting with its oscillating electric or magnetic fields. Absorption of energy by molecules is governed by the rules of quantum mechanics by which absorption of energy is quantized and it corresponds to the gap between the initial and the final energy states that molecules could occupy. Therefore, species that obey these rules will provide unique fingerprints of their interaction with electromagnetic radiation.

Photons in the infrared region of the electromagnetic spectrum possess sufficient energy to stimulate vibrations in molecules. Rotational energy levels within a specific vibrational state are closely spaced which allows molecules of an ensemble to distribute over a wide range of these levels at room temperature. Therefore, when a molecule in a specific rotational level within a vibrational state is excited by an infrared photon, then it is elevated by the amount of energy absorbed to occupy a rotational level in a higher vibrational state. High resolution infrared spectroscopy is capable of resolving the large number of distinct transitions between rotational levels in different vibrational states of molecules beyond those from very light and diatomic molecules.

Rotational and vibrational spectroscopies can be used to describe energy levels of molecules near their equilibrium structures. Determination of rotational energy levels and rovibrational energy levels (i.e. rotational levels in excited vibrational states) can be used to determine molecule specific properties such as the molecular structure and provide understanding of internal dynamics<sup>1</sup> which both depend on the molecular potential

energy surface (PES). When the assigned transitions are fitted to an appropriate Hamiltonian, molecular parameters can be determined which involve analyzing the rotational and centrifugal distortion constants in addition to the vibrational frequencies and other parameters. Determination of rotational constants allows molecular structures to be derived through their moments of inertia. When a suitable Hamiltonian is determined, it can be applied to eigenfunctions to calculate the eigenvalues of a broad range of the rotational levels within the ground and the excited vibrational states of a molecule leading to the determination of the PES. In order to gain details about the nature of potential energy surfaces, experimental observations from spectroscopic techniques are compared to calculated values of these observables according to a model function; the experiments used in this manner are far-infrared, infrared and microwave spectroscopy. These techniques allow the measurement of observables related to rovibrational states of the molecules to be studied.<sup>2</sup>

Even small molecules have very interesting and complex rovibrational spectra. For example, the floppiness that arises from the ring puckering motion in four-membered rings makes them interesting. Internal dynamics of these molecules can be described through their PESs which are different even for molecules with similar skeletons. In four-membered rings with different moieties replacing a CH<sub>2</sub> group in cyclobutane, for example, different ring puckering potential forms are gained through the analysis of infrared and Raman spectra. For example, ring puckering in azetidine (C<sub>3</sub>H<sub>6</sub>NH) leaves the molecule in two conformations in which the Hydrogen attached to the Nitrogen atom lies either in the equatorial or axial orientation. This vibration has a single asymmetric potential well<sup>3,4</sup> with the minimum of this well corresponding to the equatorial

conformation and the axial conformer is not a minimum. In silacyclobutane ( $C_3H_8Si$ ), the ring puckering potential is a double well with a large barrier<sup>5-7</sup> to planarity ( $440\text{ cm}^{-1}$ ) compared to the vibrational spacing which results in inversion tunneling doubling in the lowest vibrational states.<sup>6-8</sup> In 3-oxetanone ( $C_3H_4O_2$ ), the ring skeleton is planar with a fairly harmonic potential along the ring puckering coordinate.<sup>9,10</sup> The potential functions along the ring puckering coordinates of azetidine, silacyclobutane and 3-oxetanone are shown in Fig (1.1).

Classically, two opposing factors compete in four-membered rings in determining the planarity of the ring skeleton: the ring strain favouring the planar form and the torsional strain from the eclipsed C-H bonds favouring the puckered form. The ring puckering mode in four-membered rings is described by a one dimensional potential function, which has the form  $V=ax^4+bx^2$ , first suggested by Chan *et al.* (1966),<sup>11</sup> where x is the ring puckering displacement coordinate as defined in Fig (1.2), a is a positive constant and b is positive constant for a single well potential function or negative for a double well potential. With enough spectroscopic information from studying the ring puckering vibration, a and b can be derived as was done for 3-oxetanone.<sup>10</sup>

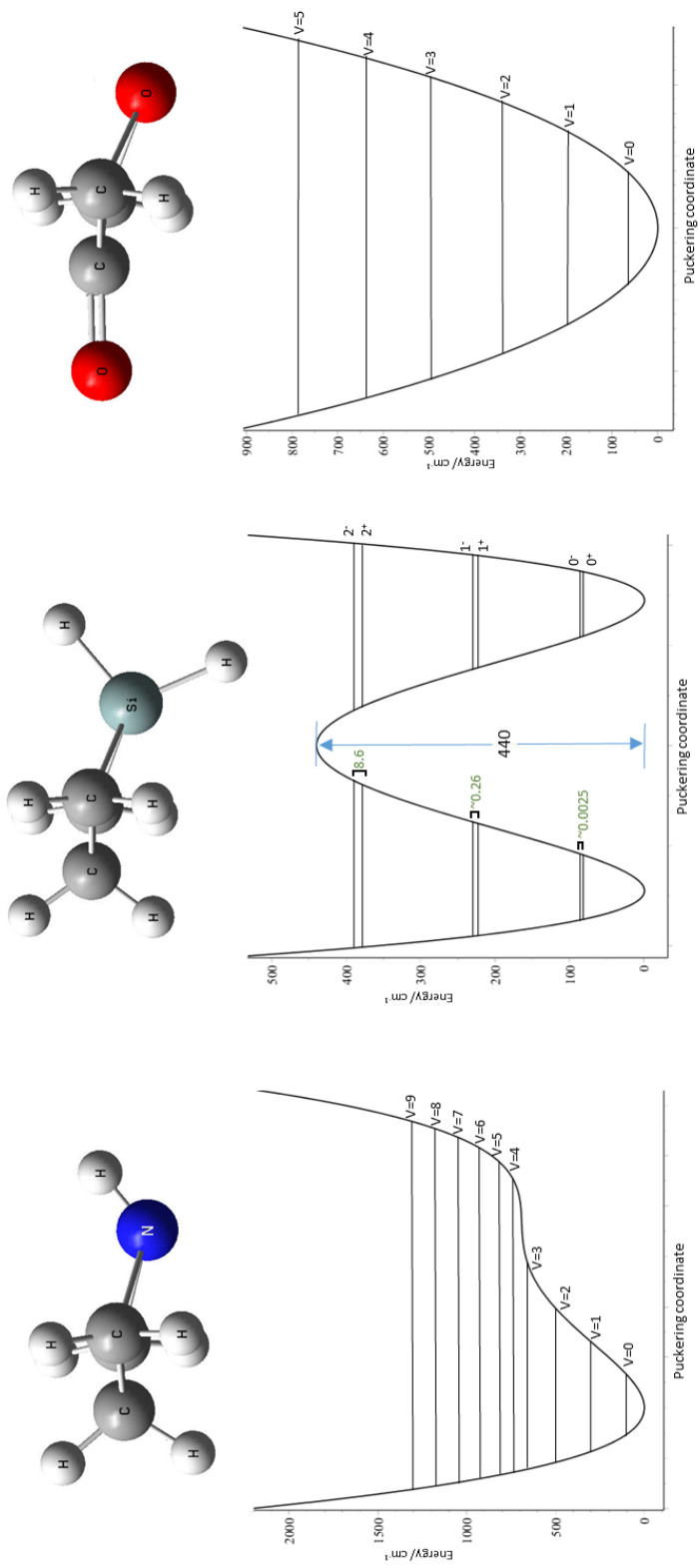


**Figure 1.1:** The potential functions along the ring puckering coordinates of azetidine,<sup>3, 4</sup> silacyclobutane<sup>5-7</sup> and 3-oxetanone<sup>9,10</sup> showing the energy (cm<sup>-1</sup>) as a function of the ring puckering coordinate. The quantum numbers of vibration are labeled on the right.

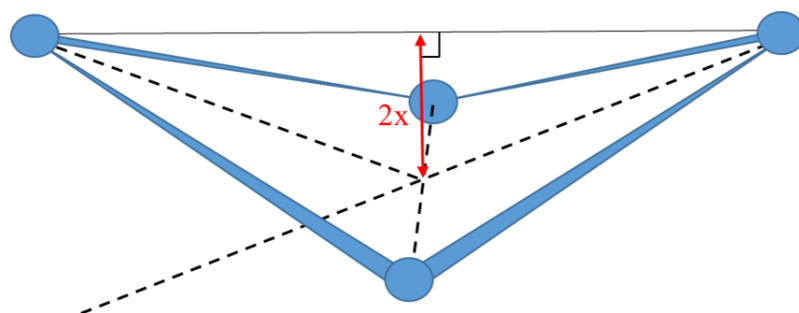


**Figure 1.2:** The ring puckering coordinate defined for a four membered ring.

### 1.1 Spectroscopy of oxetane

Oxetane ( $C_3H_6O$ ), is also known as trimethylene oxide, and its principal inertial axis system is defined by the planar geometry shown in Fig (1.2). The lowest frequency vibration in oxetane, (i.e. ring puckering mode at  $53\text{cm}^{-1}$ ), has been studied extensively for decades and a valuable effort has been put towards the determination of the oxetane potential energy curve along this coordinate. This is due to the fact that the low frequency vibrations in oxetane and structurally similar molecules are hard to model.<sup>12-17</sup> Oxetane has been studied by infrared,<sup>18-24</sup> far-infrared,<sup>11,25-29</sup> microwave<sup>30-34</sup> and Raman spectroscopy.<sup>22,35-37</sup> It was also studied by computational methods.<sup>24,38-43</sup>

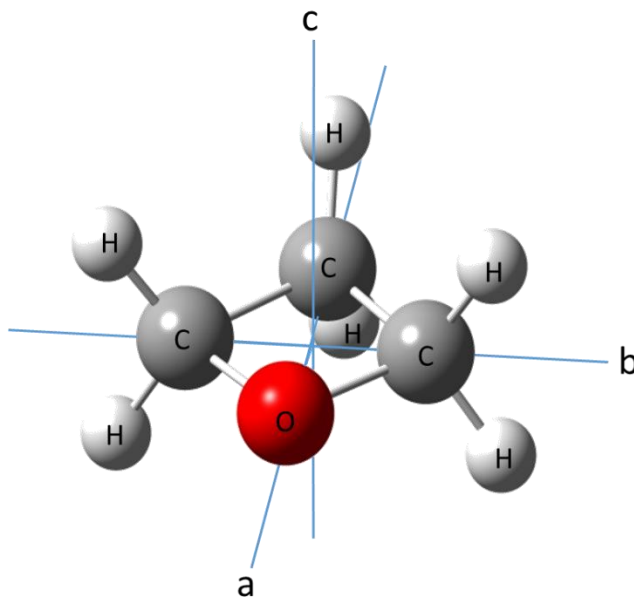


**Figure 1.3:** Principal inertial axis system is defined by the planar geometry of oxetane. .

In the case of oxetane, the potential function of ring puckering is in the shape of double minimum well<sup>11,27-29,47</sup> as shown in Fig (1.4) with a barrier to planarity of 15.52 (5)  $\text{cm}^{-1}$ <sup>27</sup> which lies below the ring puckering ground state by 11.732 (5)  $\text{cm}^{-1}$ .<sup>2</sup> Therefore, while the equilibrium structure of oxetane is puckered, the ground state conformation of the ring that can be measured is described as quasiplanar. Before this study, no high resolution infrared study has been attempted for the oxetane normal modes other than for the ring puckering mode at 53  $\text{cm}^{-1}$ . In this work, spectral analysis in the region 650-1080  $\text{cm}^{-1}$  was performed which includes several fundamental vibrations,<sup>23,41</sup> hot and combination bands that were first recognized in this work.

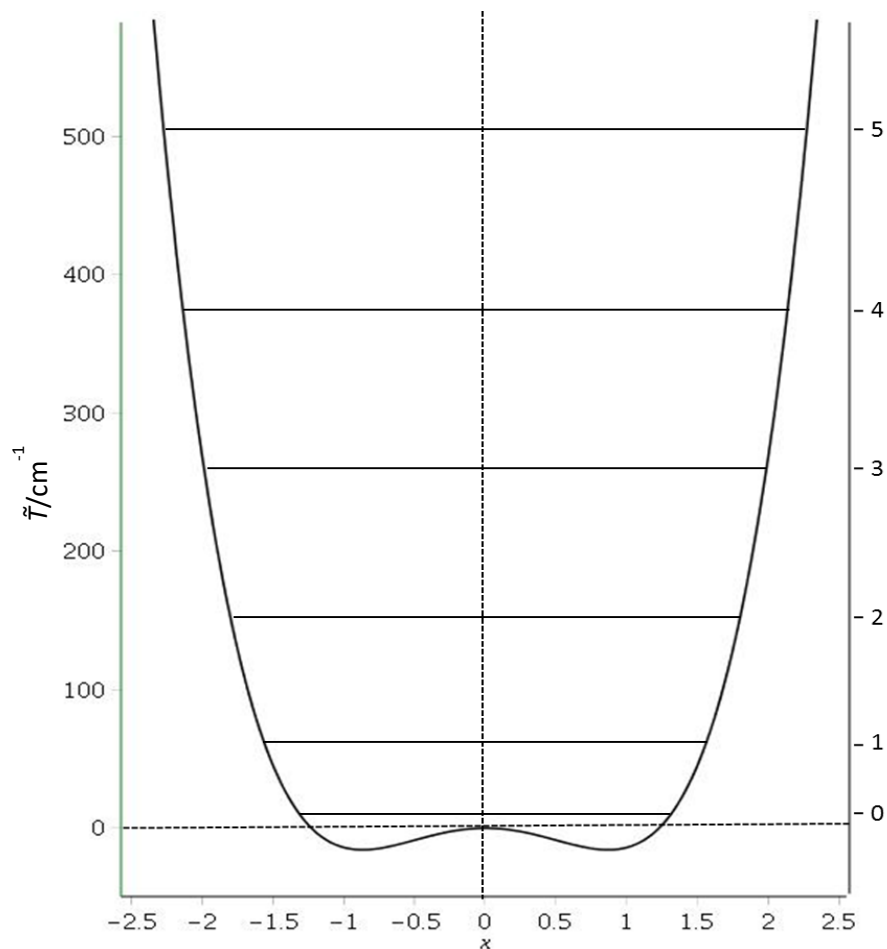


**Figure 1.4:** The potential well for the ring puckering vibration of oxetane showing the energy ( $\text{cm}^{-1}$ ) as a function of the dimensionless coordinate  $\chi$ . The quantum numbers of vibration are labeled on the right.

The conventions that are used for nomenclature and notation to describe vibrational transitions in this work are summarized here: a fundamental is the transition between the ground ( $v=0$ ) and first excited ( $v=1$ ) vibrational states; it is noted by the upper state only as  $\nu_x$  where  $x$  is a number to identify the unique vibrational motion. A hot band describes any transition that has the initial state as a vibrationally excited state ( $v>0$ ); the notation

$(v_{x1}(\text{upper state}) - v_{x2}(\text{lower state}))$  is used to describe a hot band. If  $x_1=x_2$ , one uses an integer before the band label to identify how many quanta of vibration are involved in the two states. For example,  $2v_x - v_x$  specifies that the vibrational transition is between the  $v=2$  and  $v=1$  levels of the  $v_x$  vibration. A combination band occurs when two vibrations are excited simultaneously so that quantum numbers for each vibration ( $v_x, v_y$ ) will both change. In this case, an addition sign ( $v_x + v_y$ ) is used for the notation of the combined state. The resulting frequency is ideally the sum of the contributing vibrations, however, in reality the combination of different vibrations is affected by anharmonicity and can result in the combination band appearing at a lower or higher frequency than the sum of the frequencies of the participating vibrations. An overtone is a transition where multiple quanta of a single mode are excited at once with  $\Delta v = \pm 2, \pm 3, \dots$  and starting in the ground vibrational state ( $v=0$ ) and would have a notation  $2v_x, 3v_x$ , etc.

High resolution infrared spectra reveal the rotational structure of the vibrational band and that provides important information that is not achievable using low resolution infrared techniques for the vibrational assignment. Overlapping rovibrational bands can be shown and analysed in high resolution spectra with precise determination of band centers. Rovibrational transitions initiate in rotational levels in a lower vibrational state and since the gaps between the rotational levels in the ground vibrational state can be described precisely using spectroscopic constants from microwave studies, the ground vibrational state is usually very well characterized. Thus, only the energy levels in the upper vibrational state need to be derived in such cases. In addition, rovibrational transitions are governed by selection rules which provide information about the symmetry of the energy levels involved which confirms the rovibrational assignment.

Rovibrational analysis in this study allowed the vibrational assignment of many more bands compared to literature<sup>23,41</sup> and includes hot and combination bands and re-assignment of some fundamental bands. The determination of spectroscopic constants including the rotational and the centrifugal distortion constants in multiple vibrational states in addition to the precisely determined band centers provides important benchmarks for theoretical calculations.

Also, Coriolis interactions arising due to the coupling of the rotational and the vibrational angular momenta take place in this region and can be resolved by high resolution infrared techniques. Such interactions introduce challenges for the analysis of the spectrum, however, they provide more details as suggested by Mills.<sup>45</sup> Firstly, they provide experimental values of the Coriolis zeta constants which describe the strength of the interaction that connect pairs of non-degenerate normal modes through the rotation of the molecule. This data is valuable for force constant calculations in order to calculate vibrational frequencies accurately. Secondly, treatment of Coriolis interactions allows a better vibrational assignment and can provide information about inactive or undetectable vibrations known as dark states. Thirdly, these interactions are responsible for specific perturbations in the intensity which are needed to determine the relative signs of the transition moments directly by experiment. Furthermore, since they complicate the analysis of high resolution spectra, identifying Coriolis interactions in test molecules such as oxetane will allow a better understanding of these interactions and improve their modeling in other molecules. When perturbations can be accurately modeled, the analysis of high resolution spectra becomes easier or possible for difficult cases.

## 1.2 Rovibrational spectroscopy

Energy gaps between rotational levels are small which allows sample molecules to occupy a wide range of these levels at room temperature. Therefore, excitation of molecules using infrared radiation will result in transitions between quantized rotational energy levels in different vibrational states giving rise to rovibrational spectra. This process is approximated by two ideal models: the harmonic oscillator which describes molecular vibrations and the rigid rotor which describes the molecular rotation. Rovibrational spectroscopy differs from pure rotational spectroscopy as the pure rotations occur in the molecular ground vibrational state, and the corresponding rotational spectrum appears mostly in the microwave region except for light molecules, such as CO, in which it appears in the far-infrared or millimeterwave regions of the spectrum.

### 1.2.1 Rotational energy levels of asymmetric tops

Moment of inertia is an important quantity to describe the rotational motion of a particle and corresponds to the mass of the particle moving linearly. The moment of inertia is defined as

$$I = \sum_i m_i r_i^2 \quad (1.1)$$

Where  $m_i$  is the mass and  $r_i$  is the shortest distance of the particle  $i$  from the axis of rotation as illustrated in Fig(1.5). The angular momentum ( $J$ ) of an object with moment of inertia ( $I$ ) and rotating with an angular frequency ( $\omega$ ) is given by ( $I \cdot \omega$ ).

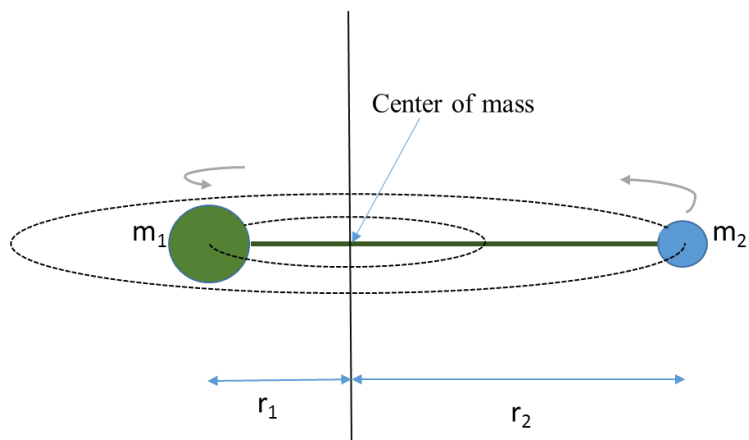


**Figure 1.5:** Moment of inertia in a rigid two-body rotor.

The kinetic energy of a rotating rigid molecule can be described classically in term of the moments of inertia which are defined as

$$E = \frac{1}{2} I \omega^2 = \frac{J^2}{2I} \quad (1.2)$$

Molecules can be categorized according to their moments of inertia that correspond to rotation of the molecule about each of its three inertial axes ( $a$ ,  $b$ ,  $c$ ) about its center of mass. The choice of these axes is set by convention according to the size of the moment of inertia for rotation about each such that  $I_a \leq I_b \leq I_c$ . By definition, symmetric tops (rotor) have two equal moments of inertia and are classified as prolate if they have  $I_a < I_b = I_c$  or oblate if they have  $I_a = I_b < I_c$ . Fig (1.6) shows an example of a prolate symmetric top. An asymmetric top (also shown in Fig (1.6)) has three different moments of inertia where by definition  $I_a < I_b < I_c$ .

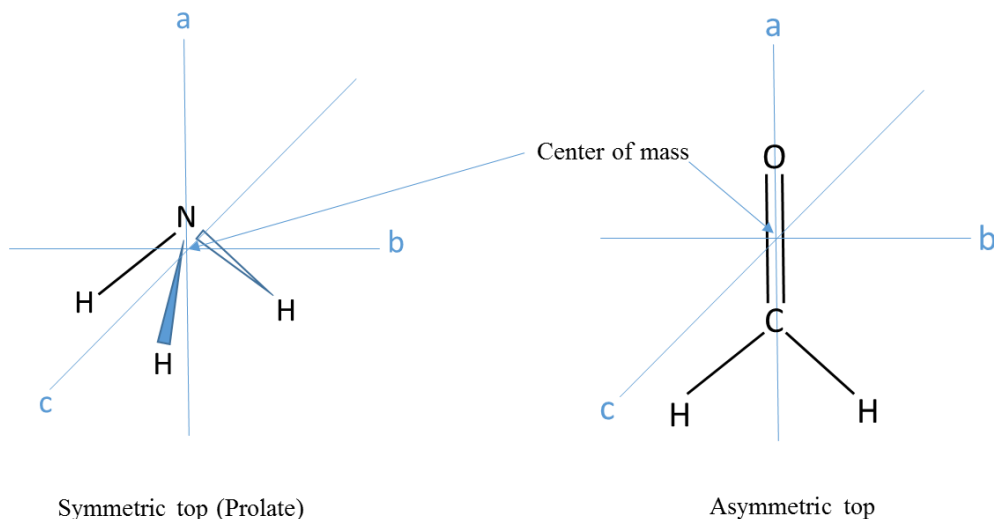


**Figure 1.6:** Examples of symmetric and asymmetric tops.

For a molecule with no electron orbital and spin angular momentum, rotational energy is expressed by

$$E = \frac{J_a^2}{2I_A} + \frac{J_b^2}{2I_B} + \frac{J_c^2}{2I_C} \quad (1.3)$$

Where  $J_a$  is the angular momentum about the a axis. The corresponding rigid rotor Hamiltonian for the asymmetric top is

$$\hat{H} = \frac{\hat{J}_a^2}{2I_A} + \frac{\hat{J}_b^2}{2I_B} + \frac{\hat{J}_c^2}{2I_C} \quad (1.4)$$

To simplify calculations, the Hamiltonian can be written in the form

$$\hbar^2 \hat{H} = \left(\frac{A+B}{2}\right) \hat{J}^2 + \left(C - \frac{A+B}{2}\right) \hat{J}_c^2 + \left(\frac{A-B}{4}\right) [(\hat{J}^+)^2 + (\hat{J}^-)^2] \quad (1.5)$$

Where the rotational constants:  $A = \frac{\hbar^2}{2I_A}$ ,  $B = \frac{\hbar^2}{2I_B}$  and  $C = \frac{\hbar^2}{2I_C}$ .  $\hat{J}^+$  and  $\hat{J}^-$  are the respective raising and lowering operators, such that  $\hat{J}^+$  increases the rotational angular

momentum along the principal axis by  $\hbar$ . Basis sets of wavefunctions of symmetric tops can be used for the purpose of approximately solving the asymmetric top quantum mechanical problem which has matrix elements with  $\Delta K=0$  and  $\Delta K=\pm 2$  where  $K$  is the component of the angular momentum  $J$  along the principal axis of rotation. To approximately solve the Schrödinger equation, the following matrix elements<sup>46,47</sup> are used.

$$\langle JK | \hat{J}^2 | JK \rangle = \hbar^2 J(J+1) \quad (1.6)$$

$$\langle JK | \hat{J}_c^2 | JK \rangle = \hbar^2 K^2 \quad (1.7)$$

$$\langle JK+2 | (\hat{J}^-)^2 | JK \rangle = \hbar^2 [(J-K)(J+K+1)(J-K-1)(J+K+2)]^{\frac{1}{2}} \quad (1.8)$$

$$\langle JK-2 | (\hat{J}^+)^2 | JK \rangle = \hbar^2 [(J+K)(J-K+1)(J+K-1)(J-K+2)]^{\frac{1}{2}} \quad (1.9)$$

Since there is no analytic solution for the Schrödinger equation of asymmetric molecules,<sup>47</sup> numerical solutions are achieved with the help of a computer. Watson's A-reduced Hamiltonian in the  $I^r$  representation,<sup>48</sup> in Pickett's SPFIT/SPCAT<sup>49</sup> and in PGOPHER<sup>50</sup> programs were used throughout this study for this purpose.

### 1.2.2 Centrifugal distortion

Rotation of molecules results in distortion of the internuclear distances and bond angles due to the fact that molecules are not rigid and that centrifugal forces act on atoms in the rotating axis system. This change in geometry results in different spectral line positions than of a molecule that is treated as rigid. Distortion of energy levels can be corrected by including terms containing centrifugal distortion constants in the Hamiltonian. Quartic centrifugal distortion constants are noted as  $\Delta_J$ ,  $\Delta_{JK}$ ,  $\Delta_K$ ,  $\delta_j$  and  $\delta_k$ ;

these correspond to terms in Watson's A-reduced Hamiltonian in the  $I^r$  representation used in this work.<sup>58</sup> Higher order distortion constants were also involved in this study since they are among the spectroscopic constants provided by Moruzzi *et al.*<sup>29</sup> that were needed to describe the ground vibrational state.

### 1.2.3 Vibrational spectroscopy of diatomic molecules

The simplest rovibrational spectrum can be seen for a diatomic molecule with two different atoms. The rovibrational selection rules for a diatomic molecule are obtained by combining the pure rotational rule with change in the rotational quantum number  $\Delta J = \pm 1$  and the vibrational rule where  $\Delta v = \pm 1$  for a harmonic oscillator. In this work, spectra are absorption spectra which are accompanied by increase in energy of molecules and this simplifies the vibrational rule to  $\Delta v = +1$ .

The intensity of a fundamental infrared vibrational transition is related to the transition dipole moment between the ground and the first vibrational excited states according to

$$I \propto |M(1,0)|^2 \quad (1.10)$$

and

$$M(1,0) = \int \psi_1^* \hat{\mu}(r) \psi_0 dr \quad (1.11)$$

Where  $\psi_0$  and  $\psi_1$  are the harmonic oscillator wavefunctions for the ground and first excited vibrational states,  $\hat{\mu}$  is the dipole moment operator which is a function of  $r$  (the distance between two nuclei in a diatomic molecule). If we take a Taylor series expansion of  $\mu$  about  $r = r_e$  (i.e.  $r_e$  the equilibrium distance corresponding to the minimum of the potential energy well)

$$\mu = \mu_e + \left(\frac{d\mu}{dr}\right)_{r_e} (r - r_e) + \left(\frac{d^2\mu}{2dr^2}\right)_{r_e} (r - r_e)^2 + \dots \quad (1.12)$$

and substitute in (1.11), we get

$$M(1,0) = \mu_e \int \psi_1^* \psi_0 dr + \left(\frac{d\mu}{dr}\right)_{r_e} \int \psi_1^* (r - r_e) \psi_0 dr + \dots \quad (1.13)$$

From equation (1.13), the first term vanishes since the wavefunctions of a harmonic oscillator are orthogonal; therefore, the vibrational transition moment is independent of the permanent dipole moment of the molecule and instead it depends on the dipole moment first derivative  $\left(\frac{d\mu}{dr}\right)_{r_e}$  at  $r_e$  if the contribution coming from higher order derivatives of the dipole moment are neglected. This means that the dipole moment must change during the vibration. The intensity of a vibrational transition is related to

$$I \propto \left| \left(\frac{d\mu}{dr}\right)_{r_e} \right|^2 \quad (1.14)$$

Also the intensity of a vibrational transition depends on the magnitude of the integral  $\int \psi_n^* (r - r_e) \psi_m dr$ . Under the harmonic oscillator approximation, a non-vanishing integral can only be achieved by a transition between two subsequent vibrational levels ( $\Delta v = \pm 1$  selection rule). In the anharmonic approximation, infrared transitions with  $\Delta v = \pm 2, \pm 3, \dots$  become allowed.

#### 1.2.4 Vibrational spectroscopy of polyatomic molecules

To detect vibrations via infrared spectroscopy, the vibration must be accompanied by a change in the dipole moment. In polyatomic molecules, symmetry-based selection rules determine which normal modes are allowed or forbidden. A vibrational transition will

occur when the transition moment, given in 1.15, is nonzero. This means that  $\psi_n^* \hat{\mu}(r) \psi_m$  must be totally symmetric in order for 1.15 to be non-vanishing.

$$M(n, m) = \int \psi_n^* \hat{\mu}(r) \psi_m d\tau \quad (1.15)$$

The vibrational ground state wavefunction of a molecule is totally symmetric which means that it is unchanged in sign when it undergoes any symmetry operation (reflection, rotation, inversion) about a symmetry element in the molecule (mirror plane, symmetry axis). In order for the fundamental ( $v=0$  to  $v=1$  transition) of a normal mode will be active in the infrared region the excited vibrational state must have the same symmetry as any of the unit vector components ( $x, y, z$ ) of the dipole moment in the inertial axis system ( $a, b$  or  $c$ ) which are listed in the character table of the point group of the molecule. This means that the excited state wavefunction follows the same behaviour as the dipole moment vector under all symmetry operations of the molecule. In this case, the direct product of the irreducible representations of the three components  $\Gamma(\psi_1^*) \otimes \Gamma(\mu) \otimes \Gamma(\psi_0)$  will be totally symmetric. Oxetane in its quasiplanar form belongs to the  $C_{2v}$  point group and therefore, the only infrared inactive modes under this point group are those with  $A_2$  symmetry since there is no dipole component with this symmetry.

### 1.2.5 Selection rules of rovibrational transitions in asymmetric tops

Rotational levels in asymmetric tops are labeled as  $J_{K_a K_c}$  where  $J$  is a good quantum number, (i.e. numbers with well-defined energy and angular momentum), while  $K_a$  and  $K_c$  are good quantum numbers only in the prolate and oblate symmetric tops limits. In addition to the selection rules discussed above, rovibrational transitions in

asymmetric tops obey rotational selection rules  $\Delta J = 0, \pm 1$ . If the change in dipole moment during vibration occurs along the  $a$ -inertial axis, the selection rules are those of  $a$ -type rotational transitions obey  $\Delta K_a = 0 (\pm 2, \pm 4, \dots)$  and  $K_c = \pm 1 (\pm 3, \pm 5, \dots)$ . Allowed  $b$ -type transitions obey the selection rules  $\Delta K_a = 1 (\pm 3, \dots)$  and  $K_c = \pm 1 (\pm 3, \dots)$  while  $c$ -type transitions obey  $\Delta K_a = 1 (\pm 3, \dots)$  and  $K_c = \pm 0 (\pm 2, \dots)$  selection rules. Groups of transitions (branches) are categorized based on the difference in the rotational quantum number ( $\Delta J$ ); the Q-branch corresponds to  $\Delta J = 0$ , the P-branch and R-branch correspond to  $\Delta J = -1$  and  $\Delta J = +1$ , respectively, as described in Fig (1.7).

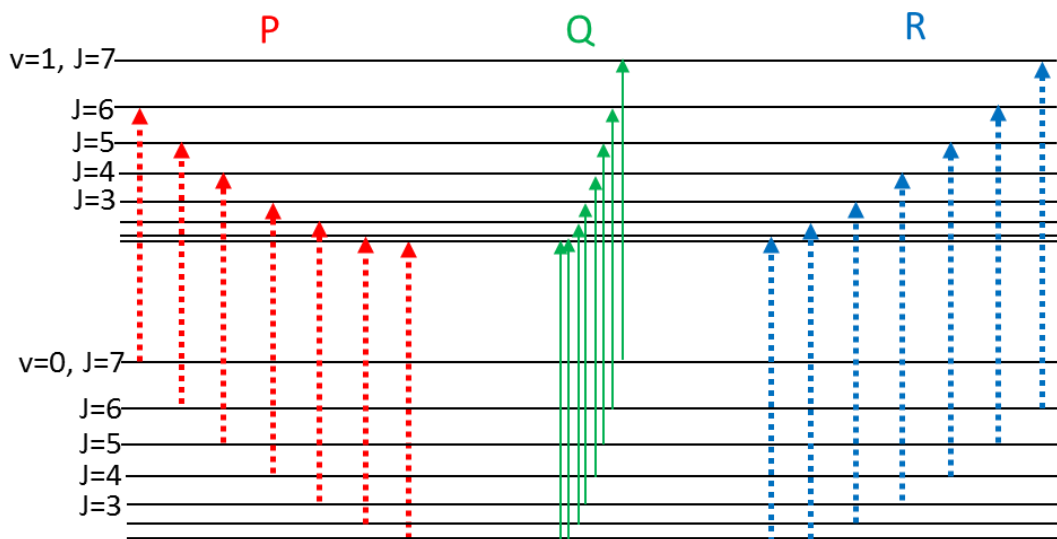


**Figure 1.7:** Schematic of P, Q and R branches for a diatomic molecule where rotational energies are  $J$  dependent only. If the  $\Delta J = 0$  transitions (Q-branch) were allowed they appear as a single sharp peak.

### 1.2.6 Combination differences

The energy of a transition equals the energy difference between the initial and final rovibrational levels. Depending on the molecule, a broad range of its rotational levels are populated within a vibrational state at room temperature which could result in a large number of rovibrational transitions in high resolution infrared spectroscopy. A combination difference is the difference in energy between two transitions that have a common energy level. Ground state combination differences GSCDs refer to energy gaps between rotational levels in the ground vibrational state as illustrated in Fig (1.8).

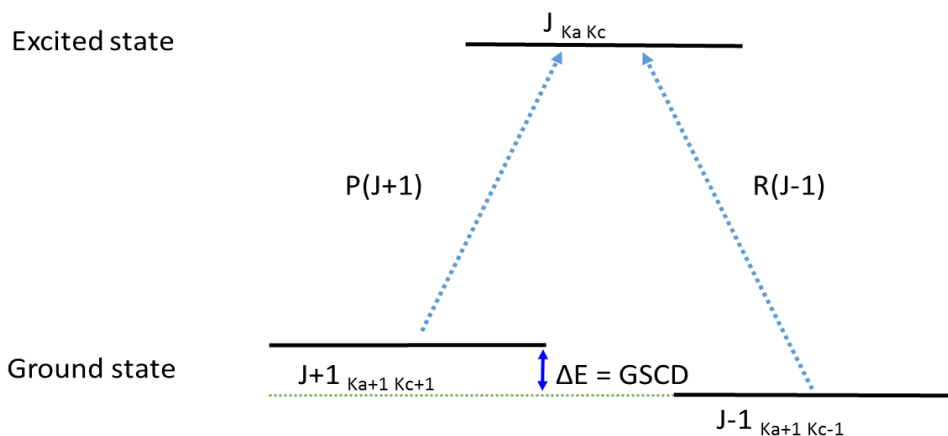


**Figure 1.8:** Schematic of a GSCD from a *b*-type band. For example, for upper level ( $v=1$ ) rotational state  $J_{K_a K_c}$  of  $10_{010}$ , there are P-branch and R-branch transitions that originate in lower level ( $v=0$ ) rotational state  $11_{111}$  and  $9_{19}$  that end in this common state.

GSCDs are used to confirm rovibrational assignments, especially when the spectrum is highly congested since the gaps between the rotational levels in the ground vibrational

state can be described precisely using spectroscopic constants available from previous microwave studies. This allows the initial vibrational state to be identified with confidence.

### 1.2.7 Coriolis interaction in rotating molecules

In order to understand rotation of molecules, one considers two coordinate systems, the laboratory coordinate system, (X,Y,Z) which is space fixed and the molecular system (x, y, z) or (a, b, c) which is rotating relative to (X,Y,Z) This means that the molecular inertial system is an accelerated system. When working with two axis systems, the description of centrifugal and Coriolis forces becomes important.

Coriolis interaction in molecules was first discussed by Teller<sup>51</sup> and later by others.<sup>45,52-54</sup> It can be explained classically using the following example. The  $H_3^+$  molecule has two degenerate modes of vibration  $\nu_{2a}$  and  $\nu_{2b}$  at  $2521\text{ cm}^{-1}$  that are coupled via a first-order Coriolis effect.<sup>47</sup> As illustrated in Fig (1.9), the molecule is pictured rotating counter clockwise and the vibrational mode  $\nu_{2a}$  is active in the laboratory frame using the solid arrows to show displacement of the atoms from their equilibrium position. If the vibration along one of these arrows is viewed in the rotating coordinate system, then the vibrational motion will appear not only radially but also diverted to the right. The Coriolis forces in this frame are responsible for the appearance of deflection of the motion to the right. The action of these forces on the  $\nu_{2a}$  mode, along the dashed arrows, leads to the excitation of the  $\nu_{2b}$  mode and vice versa. In such a case, the modes are said to be coupled via the Coriolis effect.

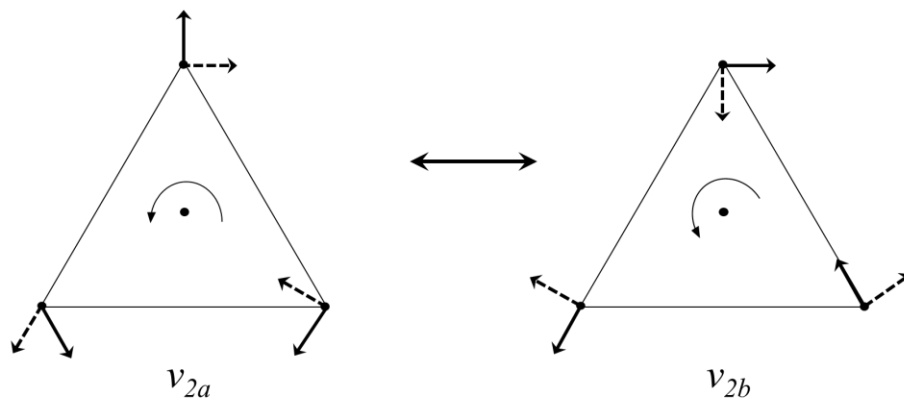


**Figure 1.9:** Coriolis interaction between the two degenerate components of the  $\nu_2$  mode of the  $\text{H}_3^+$  molecule.

When Coriolis interactions exist, the rovibrational Hamiltonian of a molecule can be expressed in the following form if the effects of anharmonicity and the dependence of the effective moments of inertia on the vibrational coordinates are neglected:

$$H = H_v + H_r + H' \quad (1.16)$$

Where  $H_v + H_r$ , consists of the vibrational Hamiltonian  $H_v$  and the rigid rotor Hamiltonian  $H_r$  and is the unperturbed part of the Hamiltonian and  $H'$  is the Coriolis perturbation. The model Hamiltonian including the Coriolis interaction terms are incorporated in Picket's SPFIT/SPCAT<sup>49</sup> and PGOPHER<sup>50</sup> programs used in this study.

Coriolis interactions in molecules are governed by selection rules. These interactions are permitted between two vibrational states if the direct product of their irreducible representations has the same symmetry as the rotation about any of the principal axes  $R_a$ ,  $R_b$ ,  $R_c$  of the molecule. For example, *c-type* Coriolis interactions are permitted between the  $A_1$ -symmetric C-C stretch ( $\nu_6$ ) and the  $B_2$ -asymmetric C-O stretch ( $\nu_{23}$ ) vibrational

states since the direct product of their symmetries  $A_1 \otimes B_2 = B_2$  corresponds to a rotation about the principal  $c$ -axis ( $R_c$ ) in the  $C_{2v}$  point group. When Coriolis perturbations exist in the spectrum, they complicate the analysis process. Perturbed transitions need to be identified first as their positions are not predictable without the inclusion of the right Coriolis terms in the model Hamiltonian and the energies of the possibly perturbing levels are also required.

This thesis consists of seven chapters. In Chapter 2, an overview of Fourier transform infrared spectroscopy using synchrotron radiation and frequency calculations is discussed. Chapter 3 discusses the preliminary analysis of the ring deformation fundamental band ( $\nu_8$ ) at  $839\text{ cm}^{-1}$  and the combination bands of the ring puckering ( $\nu_{18}$ ) mode at  $53\text{ cm}^{-1}$  and the  $\beta$ -CH<sub>2</sub>-rocking ( $\nu_{17}$ ) mode at  $702\text{ cm}^{-1}$ . Both were first recognized in this work. In Chapter 4, the preliminary rovibrational analysis of the C-O asymmetric stretch ( $\nu_{23}$ ) at  $1008\text{ cm}^{-1}$  and its hot bands ( $\nu_{18}+\nu_{23} - \nu_{18}$ ) at  $1002\text{ cm}^{-1}$ , ( $2\nu_{18}+\nu_{23} - 2\nu_{18}$ )  $999\text{ cm}^{-1}$ ) in addition to perturbations in  $\nu_{23}$  are discussed. Chapter 5 discusses the rovibrational analysis of the C-C symmetric stretch ( $\nu_6$ ) at  $1033\text{ cm}^{-1}$  and the analysis of the Coriolis interactions of this band with the  $\nu_{23}$  state. In chapter 6, the analysis of the Coriolis interactions between the  $\nu_{23}$  band and the C-C asymmetric stretch hot band ( $\nu_{24}+\nu_{18} - \nu_{18}$ ) at  $944\text{ cm}^{-1}$  and a global fit of these two bands along with the  $\nu_6$  band are described. Chapter 7 concludes this thesis and suggests future work based on the current findings.

## References

- (1) Laane, J. *Annu. Rev. Phys. Chem.* **1994**, *45*, 179.
- (2) Legon, A.C. *Chem. Rev.* **1980**, *80*, 231.
- (3) Robiette, A.G.; Borgers, T.R.; Strauss, H.L. *Mol. Phys.* **1981**, *42*, 1519.
- (4) Zaporozan, T.; Chen, Z.; van Wijngaarden, J. *J. Mol. Spectrosc.* **2010**, *264*, 105.
- (5) Laane, J.; Lord, R.C. *J. Phys. Chem.* **1968**, *48*, 1508.
- (6) Pringle, W.C.P. *J. Chem. Phys.* **1971**, *54*, 4979.
- (7) Chen, Z.; van Wijngaarden, J. *J. Chem. Phys.* **2013**, *139*, 244305.
- (8) Chen, Z.; van Wijngaarden, J. *J. Mol. Spectrosc.* **2015**, *307*, 10.
- (9) Durig, J.R.; Morrissey, A.C.; Harris, W.C. *J. Mol. Struct.* **1970**, *6*, 375.
- (10) Chen, Z.; van Wijngaarden, J. *J. Mol. Spectrosc.* **2012**, *279*, 31.
- (11) Chan, S.I.; Borgers, T.R.; Russell, J.W.; Strauss, H.L.; Gwinn, W.D. *J. Chem. Phys.* **1966**, *44*, 1103.
- (12) Malloy, T.B. *J. Mol. Spectrosc.* **1972**, *44*, 504.
- (13) Laane, J. *Pure Appl. Chem.* **1987**, *59*, 1307.
- (14) Laane, J. *Annu. Rev. Phys. Chem.* **1994**, *45*, 179.
- (15) Laane, J. *Int. Rev. Phys. Chem.* **1990**, *18*, 301.
- (16) Laane, J. *J. Phys. Chem. A.* **2000**, *104*, 7715.
- (17) Chen, Z.; van Wijngaarden, J. *J. Mol. Spectrosc.* **2012**, *279*, 31.
- (18) Zürcher, R.F.; Günthard, H.H. *Helv. Chim. Acta.* **1955**, *38*, 849.
- (19) Ueda, T.; Shimanouchi, T. *J. Chem. Phys.* **1967**, *47*, 5018.
- (20) Green, W.H. *J. Chem. Phys.* **1970**, *52*, 2156.
- (21) Wieser, H.; Danyluk, M. *Can. J. Chem.* **1972**, *50*, 2761.

- (22) Wieser, H.; Danyluk, M.; Kydd, R.A.; Kiefer, W.; Bernstein, H.J. *J. Chem. Phys.* **1974**, *61*, 4380.
- (23) Kydd, R.A.; Wieser, H.; Kiefer, W. *Spectrochim. Acta.* **1983**, *39A*, 173.
- (24) Turnbull, D.M.; Sowa, M.G.; Henry, B.R. *J. Phys. Chem.* **1996**, *100*, 13433.
- (25) Danti, A.; Lafferty, W. J.; Lord, R.C. *J. Chem. Phys.* **1960**, *33*, 294.
- (26) Wieser, H.; Danyluk, M.; Kydd, R.A. *J. Mol. Spectrosc.* **1972**, *43*, 382.
- (27) Jokisaari, J.; Kauppinen, J. *J. Chem. Phys.* **1973**, *59*, 2260.
- (28) Winnewisser, M.; Kunzmann, M.; Winnewisser, B. *J. Mol. Spectrosc.* **2001**, *561*, 152.
- (29) Moruzzi, G.; Kunzmann, M.; Winnewisser, B. ; Winnewisser, M. *J. Mol. Spectrosc.* **2003**, *219*, 152.
- (30) Chan, S.I.; Zinn, J.; Fernandez, J.; Gwinn, W.D. *J. Chem. Phys.* **1960**, *33*, 1643.
- (31) Creswell, R.A.; Mills, I.M. *J. Mol. Spectrosc.* **1974**, *52*, 392.
- (32) Allison, P.D.; Roberta, A.G. *J. Mol. Spectrosc.* **1974**, *52*, 413.
- (33) Creswell, R.A. *J. Mol. Phys.* **1975**, *30*, 217.
- (34) Lesarri, A.; Blanco, S.; Lopez, J.C. *J. Mol. Struct.* **1995**, *354*, 237.
- (35) Wieser, H.; Danyluk, M.; Kiefer, W.; Bernstein, H.J. *Can. J. Chem.* **1972**, *50*, 2771.
- (36) Kiefer, W.; Bernstein, H.J.; Danyluk, M.; Wieser, H. *Chem. Phys. Lett.* **1972**, *12*, 605.
- (37) Kiefer, W.; Bernstein, H.J.; Wieser, H.; Danyluk, M. *J. Mol. Spectrosc.* **1972**, *43*, 393.
- (38) Sellers, H.; Almelo, J.; Saeb, S.; Play, P. *J. Phys. Chem.* **1987**, *91*, 4216.
- (39) Bocian, D.F.; Schick, G.A.; Barge, R.R. *J. Chem. Phys.* **1981**, *74*, 3660.

- (40) Foltynowicz, I. *J. Mol. Spectrosc.* **1982**, 96, 239.
- (41) Banhegyi, G.; Play, P.; Fogarasi, G. *Spectrochim. Acta.* **1983**, 39A, 761.
- (42) Mastryukov, V.S.; Boggs, J.E. *J. Mol. Struct. (Theochem).* **1995**, 338, 235.
- (43) Chong, D.P.; Hu, C.H. *J. Chem. Phys.* **1998**, 108, 8950.
- (44) Kydd, R.A.; Wieser, H.; Danyluk, M. *J. Mol. Spectrosc.* **1972**, 44, 14.
- (45) Mills, I.M. *Pure Appl. Chem.* **1965**, 11, 325.
- (46) Kroto, H.W. *Molecular Rotation Spectra*; Dover: New York, 1992.
- (47) Bernath, P.F. *Spectra of Atoms and Molecules*; Oxford University Press: New York, 1995.
- (48) Watson, J.K.G. In *Vibrational Spectra and Structure*; Durig, J. Ed; Vol. VI; Elsevier: Amsterdam, 1977.
- (49) Pickett, H.M. *J. Mol. Spectrosc.* **1991**, 148, 371.
- (50) Western, C.M. *J. Quant. Spectrosc. Ra*, **2016**, 186, 221.
- (51) Teller E., *Hand- und Jahrbuch der Chem. Physik*; Akademische Verlagsgesellschaft: Leipzig, 1934; 9.
- (52) Hohnston, M.; Dennison, D.M. *Phys. Rev.* **1935**, 48, 868.
- (53) Jahn, H.A. *Proc. R. Soc. Lon. Ser-A.* **1939**, 168, 469.
- (54) Boyd, D.R.J.; Longuet-Higgins, H.C. *Proc. R. Soc. Lon. Ser-A.* **1952**, 213, 55.

## Chapter 2. High resolution Fourier transform infrared (FTIR) spectroscopy of oxetane

### 2.1 High resolution spectroscopy

In this work, high resolution refers to the spectral resolution ( $\Delta\bar{\nu}$ ) needed to account for the rotational structure of a vibrational band for molecules that show more complicated rotational patterns than diatomic and very light molecules. In general, resolution in gas phase infrared can be limited by either pressure or Doppler broadening of the absorption line. Higher pressure increases the possibility of collisions between molecules which distorts energy levels of them. At lower pressure, the Doppler broadening depends on many factors which are given by

$$\text{FWHH} = 2\Delta\bar{\nu} = \frac{\bar{\nu}}{c} \left( \frac{8NkT\ln 2}{M} \right)^{\frac{1}{2}} \quad (2.1)$$

Where FWHH is the full width at half-height of the spectral line,  $N$  is Avogadro's number,  $k$  is the Boltzmann constant,  $T$  is the temperature,  $\bar{\nu}$  is the reciprocal wavelength ( $\text{cm}^{-1}$ ), and  $M$  is the molecular mass (amu). In gas phase infrared spectroscopy, FWHH is minimal in the far-infrared region for heavy molecules due to the Doppler effect.

#### 2.1.1 Michelson interferometer

A Michelson interferometer is the heart of the spectrometer in Fourier transform infrared (FTIR) spectroscopy. An interferogram is created from the interference between two beams which have an optical path difference or retardation. In the simple design of the Michelson interferometer, it consists of two mirrors that lie perpendicularly to each

other; one is a stationary mirror and the second is movable along its axis at constant velocity as shown Fig (2.1). The source light is partially reflected to the fixed mirror by the beamsplitter, and it transmits the remainder of the light to the moving mirror. The beamsplitter recombines the beams reflected back from each mirror.<sup>1</sup> The combined beam is directed so that it interacts with the sample and the transmitted light then leaves toward the detector where the light intensity versus optical path difference (OPD) is measured resulting in an interferogram. The interferogram is then Fourier transformed to produce a plot of light intensity versus wavenumber (reciprocal centimeters), the spectrum.<sup>2</sup>

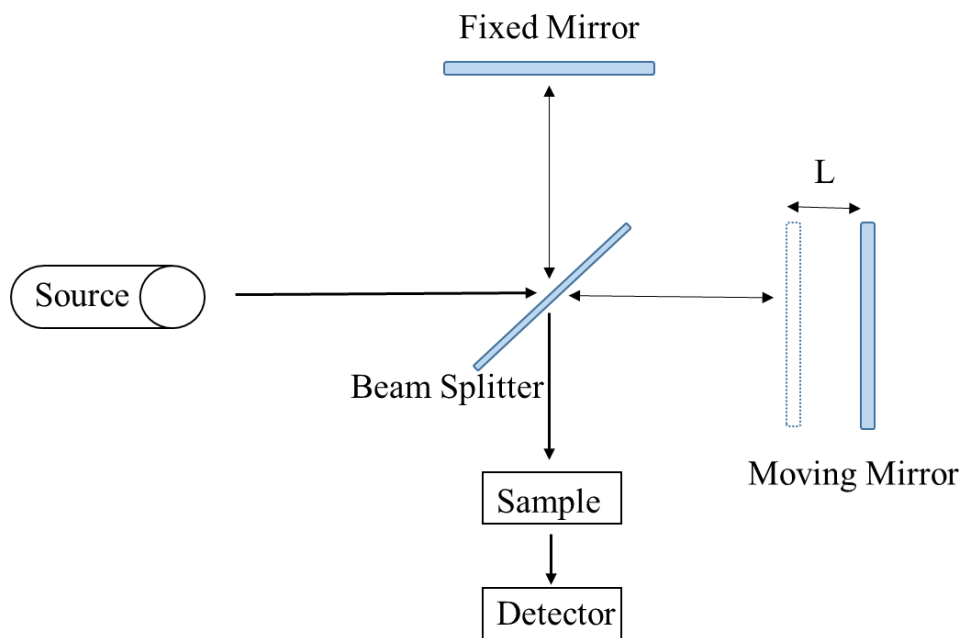


**Figure 2.1:** A schematic diagram of a Michelson interferometer configured for FTIR spectroscopy.

The spectral resolution of a Fourier transform instrument is the optical path difference reciprocal such that:

$$\Delta\bar{\nu} = \frac{1}{\text{OPD}} = \frac{1}{2L} \quad (2.2)$$

Where L is the travel length of the moving mirror from the equidistant position with the fixed mirror. Equation 2.2 shows that longer optical path difference is preferred in order to achieve higher spectral resolution. Circular interference fringes are generated at the detector due to divergence of rays from typical infrared sources.<sup>3,4,5</sup> The spacing between successive fringes decreases with the increase in the path difference and results in loss of resolution.<sup>5</sup> In order to maintain the resolution, an aperture at the detector is often used to allow the measurement of the central fringe only.<sup>5,6</sup> The diameter d of the aperture required to achieve a desired resolution ( $\Delta\bar{\nu}$ ) at a given wavenumber is given by:

$$d = 2F\sqrt{\Delta\bar{\nu} / \bar{\nu}} \quad (2.3)$$

Where F is the focal length of the parabolic collimating mirror in the interferometer.

### **2.1.2 Light Source (Synchrotron Radiation)**

Synchrotron radiation is a brilliant light, an expensive replacement to the conventional light sources such as a tungsten filament, globar or mercury discharge lamp. However, the nature of synchrotron radiation makes it the ideal light source for FTIR spectroscopy using a Michelson interferometer as described below.

### **2.1.2.1 How does a synchrotron work?<sup>7</sup>**

A synchrotron consists of several key components, mainly: electron gun, linear accelerator (LINAC), booster ring, storage ring. Generating light starts at the electron gun and happens by applying high voltage (approximately 200,000 volts) to a heated cathode, usually a tungsten-oxide disk. Heating the disk (at about 1000 °C) gives some electrons enough energy to leave the surface. The electrons get repelled toward the LINAC by the high voltage. In the LINAC, a microwave radio frequency field is applied to the electrons so that they gain energy and get accelerated to 99.9998% of the speed of light at this stage. Pulses of electrons are injected into the booster ring. The electron transfer must happen in high vacuum which ultimately reaches lower than  $10^{-11}$  Torr at the Canadian Light Source (CLS). Then the electrons are transferred from the booster ring to the storage ring. The synchrotron light is emitted when the electron path is bent at the bending magnet in the storage ring. When the light is emitted, it is introduced to the beamlines which have component mirrors and optics that focus the light and selects the desired wavelength to transfer the light to the experimental hutch. It is the experimentation hutch and work station where the experimental part takes place.

### **2.1.2.2 Synchrotron Advantage**

Using synchrotron radiation for gas phase infrared spectroscopy is only beneficial when used with a high resolution instrument ( $\leq 0.004\text{cm}^{-1}$ ). For lower resolution studies, conventional sources can offer good results when coupled to a qualifying spectrometer. The synchrotron radiation advantage is related to the brightness of the infrared light

passing through a small aperture rather than the total radiation flux. Since synchrotron radiation is highly collimated, intense light can pass through a small aperture. In turn, it is valuable in condensed matter applications such as spectromicroscopy for the investigation of samples with high spatial resolution. For high spectral resolution in gas phase experiments,<sup>8-16</sup> the use of synchrotron radiation is most advantageous in the far-infrared region. Doppler broadening is a limiting factor and therefore, very high resolution is not achievable in the mid-infrared region  $>1500\text{ cm}^{-1}$ . Equation 2.3 shows that the highest resolution can be achieved at a certain wavelength when a smaller aperture is used since it minimizes the oblique rays that affect the quality of the interferogram.<sup>1</sup> At the same time, the high brightness ensures a sufficient level of light intensity to reach the infrared detector through the small aperture. The theoretical synchrotron advantage is more than three orders of magnitudes, which is achievable for small apertures in the far-infrared. In practice, the actual synchrotron advantage is about order of magnitude and is limited by the synchrotron source noise which results from fluctuations in the electron beam or because of mechanical noise due to vibrations in the mirrors responsible for transportation of the radiation from the storage ring through the spectrometer.<sup>16</sup>

## **2.2 Experimental details**

The rovibrational spectrum of oxetane between  $400$  and  $1150\text{ cm}^{-1}$  was recorded at the Canadian Light Source (CLS) using the synchrotron radiation as the light source and a Bruker IFS125HR FTIR spectrometer. This instrument has an optical path difference of

nearly 10 m which allows for spectral resolution of  $\sim 0.00096 \text{ cm}^{-1}$ . The liquid oxetane sample used was purchased commercially and the vapour above a small sample volume (1-2 mL) was sufficient to record all spectra needed. The vapour was added to a large cylindrical stainless steel gas cell which is 2 m long and 0.3 m in diameter. Mirrors at each end of the cell are arranged to pass the light back and forth to create a total absorption path length of about 80 m.

This region was chosen for analysis based on the prediction of the frequency calculations in this work and interpretations<sup>17,18</sup> of a previous low resolution far-infrared work<sup>17</sup> which suggests that several infrared active normal modes appear in this region. Also, in this region, a useful high resolution spectrum for the rovibrational analysis can be achieved. When the spectrum was recorded at low pressure, more bands appeared than were suggested by the frequency calculations and previous low resolution work<sup>17</sup> and these new bands have low infrared intensity as can be seen in the continuous overlap between bands that vary in intensity in Fig (2.2). Therefore, optimization of the spectrum was needed. This was mainly done by recording the spectrum at different sample vapor pressures.

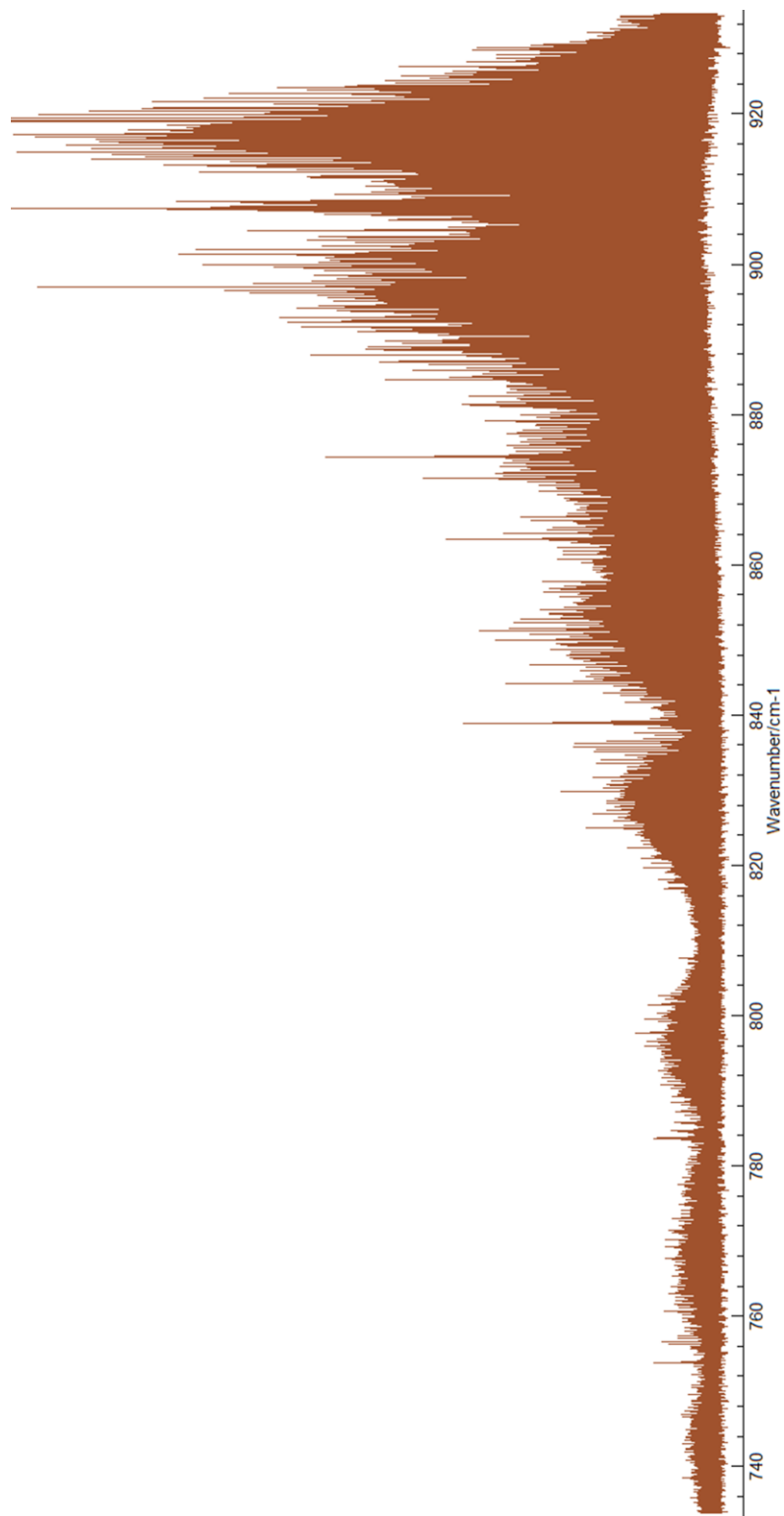


**Figure 2.2** : High resolution infrared spectrum of oxetane at 10 mTorr between 738 and 824  $\text{cm}^{-1}$  at room temperature.

Optimization of other experimental aspects was also made. The spectra were collected according to the optimized parameters listed in Table 2.1. The time needed to record a total of 706 interferogram was over one week of beamtime.

**Table (2.1):** Experimental parameters of the high resolution infrared spectra of oxetane measurements at the CLS.

Parameter	Set up
Spectrometer	Bruker IFS125HR
Spectral Region	400-1150 $\text{cm}^{-1}$
Source	Synchrotron radiation
Aperture size	1.15 mm
Scanner velocity	40 kHz
Detector	GeCu detector
Beam splitter	KBr
Cell windows	KBr
Calibration	H <sub>2</sub> O
Absorption cell path length	72 m
Resolution	0.00096 $\text{cm}^{-1}$
Cell temperature	298
Pressure	5, 10, 180, 200 and 500 mTorr
*Number of averaged scans	44, 146, 330, 54 and 132.

\*Arranged respectively to the different pressure measurements

### 2.3 Structure of the rotationally resolved infrared spectrum

The symmetry based selection rules are reflected in the contour of the rovibrational band. The part of the spectrum shown in Fig (2.3) shows the contour of an *a-type* band which corresponds to the change in the dipole moment along the inertial a-axis during vibration. The asymmetry in the intensity of this band's wings depends largely on the overlap of the R-branch with a series of bands located at about  $785\text{ cm}^{-1}$ .

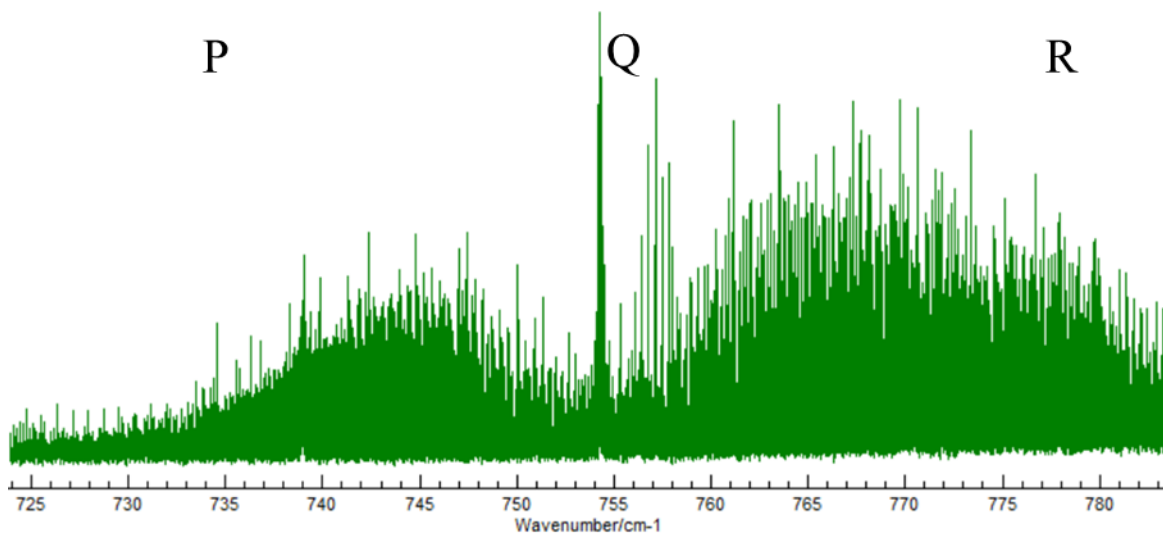


**Figure 2.3:** High resolution infrared spectrum of oxetane at 200 mTorr between 724 and  $783\text{ cm}^{-1}$  at room temperature in which the contour of the *a-type* band  $\nu_{17}+\nu_{18}$  at  $754\text{ cm}^{-1}$  is shown.

The spectrum in Fig (2.3) involves thousands of individual rovibrational transitions. A magnified portion of less than a wavenumber width from this band is shown in Fig (2.4) to show the rotational structure in the P-branch.

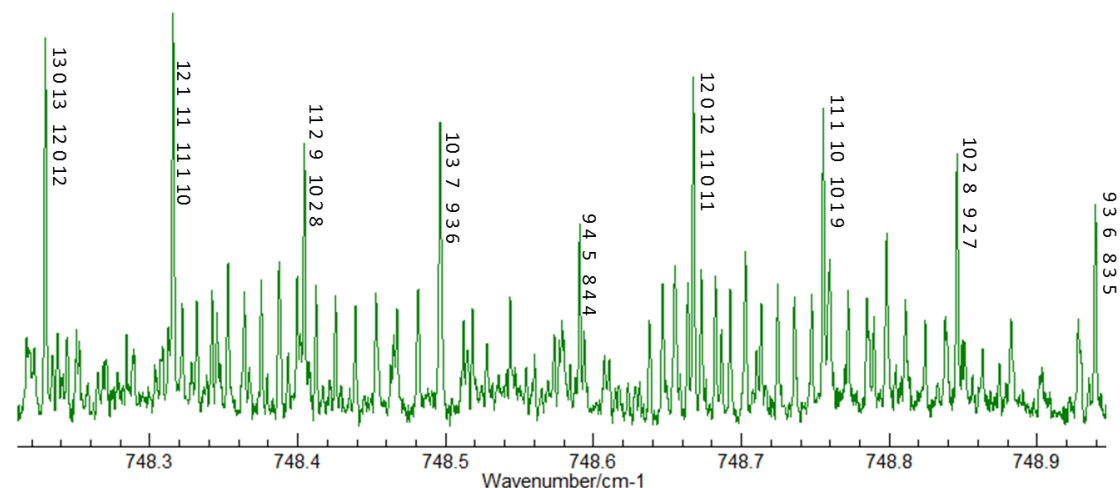


**Figure 2.4:** A magnified portion of the spectrum in Fig (2.3). Strong transitions in the P-branch are labeled with the rotational quantum numbers  $J_{K_aK_c}$  of the lower and the higher vibrational levels.

A smaller window of the spectrum ( $\sim 0.1 \text{ cm}^{-1}$ ) shows the rotational structure in the Q-branch Fig (2.5). Fig (2.4) and Fig (2.5) indicate that a large number of rovibrational transitions exist in the rotationally resolved spectrum of oxetane. It was the objective of this work to assign as much of this structure as possible for all observed bands of oxetane between  $400$  and  $1150 \text{ cm}^{-1}$ .

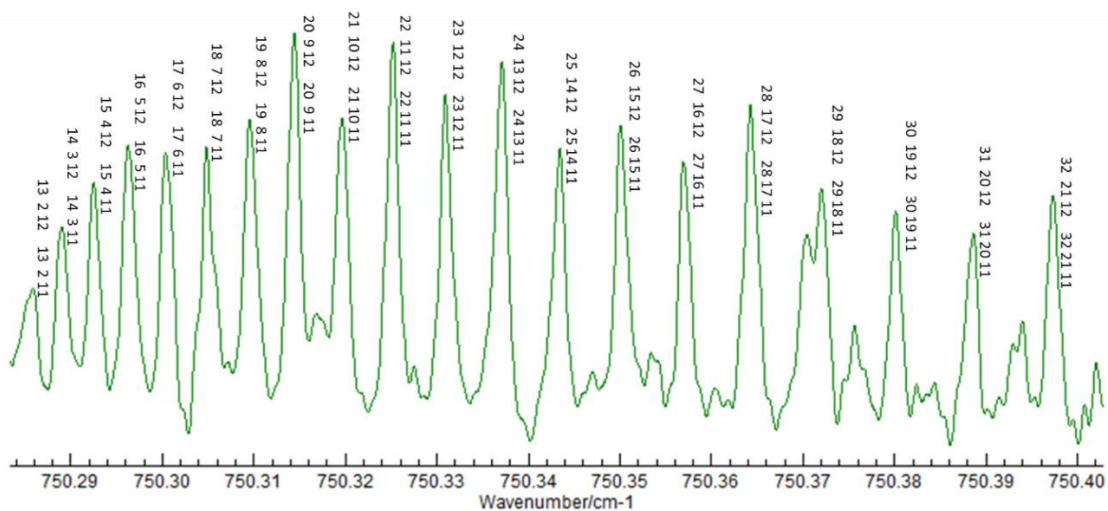


**Figure 2.5:** A magnified portion of the spectrum in Fig (2.2). A progression in the Q-branch is labeled with the rotational quantum numbers  $J_{K_a K_c}$  of the lower and the higher vibrational levels.

## 2.4 Previous studies on the low resolution infrared spectrum of oxetane

The band center assignment of oxetane fundamental vibrations has been attempted in earlier studies.<sup>17-21</sup> The vibrational assignment done by Kydd *et al.* (1983)<sup>17</sup> should be highlighted followed by an *ab initio* prediction of the oxetane vibrational spectra by Banhegyi *et al.* (1983).<sup>18</sup> Kydd's assignments are based on the infrared spectra of oxetane in the gas phase, in matrix-isolated solids at 15 K and the Raman spectra of oxetane in the gas and liquid phases. The *ab initio*, Self-Consistent Field (SCF) calculations using the 4-21G basis set by Banhegyi *et al.* were used to optimize the geometry of oxetane and were followed by force field frequency calculations at the planar reference geometry. These first attempts at assignments are summarized in Table 2.2.

**Table (2.2):** Frequency calculations of oxetane fundamental bands ( $\text{cm}^{-1}$ ) compared with the experimental values.

$\nu$	Symmetry	Normal mode	Calc. MP2 <sup>1</sup>		Calc. B3LYP <sup>1</sup>		[Calc.] <sup>2</sup>	Kydd <i>et al.</i> <sup>3</sup>	Experiment
			harm	anharm	harm	anharm			This study
1	A <sub>1</sub>	$\beta$ -H-C-symm. stretch	3131	3038	3065	2908	2959	2979	
2	A <sub>1</sub>	$\alpha$ -H-C-symm. stretch	3080	2944	3029	2851	2941	2984	
3	A <sub>1</sub>	$\alpha$ -CH <sub>2</sub> -scissoring	1561	1497	1540	1478	1511	1505	
4	A <sub>1</sub>	$\beta$ -CH <sub>2</sub> -scissoring	1507	1483	1492	1468	1458	1452	
5	A <sub>1</sub>	$\alpha$ -CH <sub>2</sub> -wagging	1376	1343	1369	1336	1338	1343	
6	A <sub>1</sub>	C-C-symm. stretch	1046	1024	1039	1019	1032	1033	1033
7	A <sub>1</sub>	C-O-symm. stretch	910	883	914	894	903	909	908
8	A <sub>1</sub>	Deformation	856	831	815	779	801	785	839
9	A <sub>2</sub>	$\alpha$ -H-C-asyymm. stretch	3156	3006	3081	2999	2987		
10	A <sub>2</sub>	$\beta$ -CH <sub>2</sub> -twisting	1231	1202	1230	1195	1235	<b>1230</b>	
11	A <sub>2</sub>	$\alpha$ -CH <sub>2</sub> -twisting	1159	1134	1159	1128	1112	<b>1096</b>	
12	A <sub>2</sub>	$\alpha$ -CH <sub>2</sub> -rocking	839	829	836	825	833	842	
13	B <sub>1</sub>	$\beta$ -H-C-asyymm. stretch	3205	3057	3135	2986	3010	3006	
14	B <sub>1</sub>	$\alpha$ -H-C-symm. stretch	3155	3007	3067	2910	2981	2938	
15	B <sub>1</sub>	$\alpha$ -CH <sub>2</sub> -twisting	1214	1182	1193	1166	1197	<b>1183</b>	
16	B <sub>1</sub>	$\alpha$ -CH <sub>2</sub> -rocking	1155	1130	1144	1125	1097	<b>1137</b>	
17	B <sub>1</sub>	$\beta$ -CH <sub>2</sub> -rocking	707	706	766	748	740	703	702
18	B <sub>1</sub>	Ring puckering <sup>4</sup>	134	87	61	118	120		
19	B <sub>2</sub>	$\alpha$ -H-C-asyymm. stretch	3075	2924	3021	2855	2935	2887	
20	B <sub>2</sub>	$\alpha$ -CH <sub>2</sub> -scissoring	1532	1525	1513	1467	1483	1480	
21	B <sub>2</sub>	$\alpha$ -CH <sub>2</sub> -wagging	1319	1289	1308	1275	1274	1289	
22	B <sub>2</sub>	$\beta$ -CH <sub>2</sub> -wagging	1279	1246	1257	1224	1261	1230	
23	B <sub>2</sub>	C-O-asyymm. stretch	999	969	1019	982	1022	1008	1008
24	B <sub>2</sub>	C-C-asyymm. stretch	956	940	939	905	940	937	

<sup>1</sup> Using 6-31++G(2d,2p) basis set in this work

<sup>2</sup> From Banhegyi *et al.* in ref. 18. Geometry optimized using SCF/4-21G, frequencies calculated using force field at planar geometry

<sup>3</sup> From ref 17; Underlined bands assigned experimentally by Banhegyi *et al.*; bold denotes liquid phase Raman bands

<sup>4</sup> Experimentally determined in ref 27 at 53  $\text{cm}^{-1}$

The calculations performed by Banhegyi *et al.* do not reproduce the observed experimental band centers for low frequency vibrations. For instance, they calculated the  $\beta$ -CH<sub>2</sub>-rocking fundamental at 740 cm<sup>-1</sup> while it was assigned at 702 cm<sup>-1</sup> in this work. This may be attributed to the fact that they chose the planar geometry as a reference for the frequency calculations, however, oxetane is quasiplanar and very floppy.<sup>22-26</sup> In addition, the high resolution spectrum in this work shows more bands than expected based on these early works. In fact although only seven fundamental bands are predicted between 400 and 1150 cm<sup>-1</sup> according to the frequency calculations by Banhegyi *et al.*, the spectra collected in this work identified at least 20 different band centers. Therefore, it was necessary to perform frequency calculations at a higher level of theory in this work in order to help with the assignment of the bands to their corresponding vibrations.

## 2.5 Frequency calculations

Quantum mechanical frequency calculations can be used as a guide in the analysis of the high resolution infrared spectra. When no experimental rotational and centrifugal distortion constants are available for excited vibrational levels, calculated constants can be used to predict patterns of transitions in the rovibrational spectra. Furthermore, calculated frequencies and infrared intensities help in the assignment of infrared bands to the corresponding vibrations. Therefore, geometry optimization followed by harmonic and anharmonic frequency calculations using Density Functional Theory (DFT) with the B3LYP functional in Gaussian 09<sup>27</sup> using the 6-31++G (2d, 2p) basis set were performed.

Tight convergence criteria were applied during geometry optimization in order to achieve a more reliable prediction of the low frequency vibrations.

Møller–Plesset second order perturbation theory (MP2) in Gaussian 09<sup>27</sup> was then used to optimize the geometry and to calculate harmonic and anharmonic vibrational frequencies for comparison with the DFT results. Calculations using the basis set 6-31++G (2d, 2p) generally showed the least variance from the experimental results in this study. Using the MP2 method, the geometry was optimized to the puckered form which is the equilibrium geometry of oxetane.<sup>22-26</sup> Fundamental vibrations assigned in this study are compared to the assignments by Kydd *et al.* and Banhegyi *et al.* and to the frequency calculations using both MP2 and DFT methods in Table 2.2.

The frequency calculations using the MP2 method outperform calculations using the DFT and SCF methods for the low frequency vibrations. The geometry was optimized to the planar form using the DFT method which resulted in poor prediction of the low frequency vibrations:  $\beta$ -CH<sub>2</sub>-rocking and the ring deformation fundamental bands with 7.6% and 2.9% respective variation from the experimental values obtained in this study. The respective variation in the calculated frequencies of these two modes using the SCF method is 5.4% and 9.5%.

In general, frequency calculations using the MP2 method with anharmonic corrections were predicted to be closer to the experiment than the harmonic calculations. MP2 predictions of the low frequency modes  $\beta$ -CH<sub>2</sub>-rocking, ring deformation and C-O-symmetric stretch showed 2.0%, 0.6% and 0.2%, respective variations from the experimental values obtained in this study, however, the ring puckering mode is predicted

to be 64% from the experimental value ( $53 \text{ cm}^{-1}$ ).<sup>26</sup> The previous discussion shows that there is no single method that systematically reproduces the experimental results. This is why analyzing the rotational structure of each band is necessary to ensure that the vibrational assignment is correct.

The rovibrational analysis of individual bands is described in detail in the remainder of this thesis. Once the rotational patterns are understood, the identity of the extra bands can be deduced. For example, a number of bands due to coupling of the ring puckering vibration ( $53 \text{ cm}^{-1}$ ) with other modes were assigned based on the rotational analysis in this study. They are described in Table 2.3; however, their assignments are explained in chapters 3 and 4.

**Table (2.3):** Assigned combination and hot bands of oxetane, in the region of study.

Band	Vibration assignment ( $\text{cm}^{-1}$ )
$\nu_{17} + \nu_{18}$	754
$\nu_{17} + 2\nu_{18} - \nu_{18}$	784
$\nu_{17} + 3\nu_{18} - 2\nu_{18}$	785
$\nu_{17} + 4\nu_{18} - 3\nu_{18}$	786
$\nu_7 + \nu_{18} - \nu_{18}$	864
$\nu_{18} + 2\nu_{23} - 2\nu_{18}$	999
$\nu_{18} + \nu_{23} - \nu_{18}$	1002

## References

- (1) Burns, D.A.; Ciurczak, E.W. *Handbook of Near Infrared Analysis*, 3<sup>rd</sup> ed.; Taylor and Francis Group: New York, 2008.
- (2) Smith, B.C. *Fundamentals of Fourier Transform Infrared Spectroscopy*, 2<sup>nd</sup> ed.; CRC Press: Boca Raton, FL, 2011.
- (3) Lowenstein, E.V. *Fourier spectroscopy: an introduction*, *Aspen International Conference on Fourier Spectroscopy*; 1970.
- (4) Vanasse, G.A.; Stair Jr, A.T.; Baker, D.J. *Aspen International Conference on Fourier Spectroscopy*; 1970. (No. AFCRL-71-0019). Air Force Cambridge Research Labs Hanscom AFB MA 1971.
- (5) Griffiths, P.R.; De Haseth J.A. *Fourier transform infrared spectrometry*, 2<sup>nd</sup> ed. Vol. 171; John Wiley & Sons: Hoboken, New Jersey, 2007.
- (6) Chalmers, J.M.; Griffiths, P.R. *Handbook of vibrational spectroscopy*, Vol. I; Wiley: Chichester, UK, 2002.
- (7) <http://www.lightsource.ca/education/whatis.php> (Accessed on 18-07-15 at 1:00 pm)
- (8) Duncan, W.D.; Williams, G.P. *Appl. Opt.* **1983**, 22, 2914.
- (9) Schweizer, E.; Nagel, J.; Braun, W.; Lippert, E.; Bradshaw, A.M. *Nucl. Instrum. Meth Phys. A* **1985**, 239, 630.
- (10) Williams, G.P. *Rev. Sci. Instrum.* **1992**, 63, 1535.
- (11) Ugawa, A.; Ishii, H.; Yakushi, K.; Okamoto, H.; Mitani, T.; Watanabe, K.; Sakai, K.; Suzui, K.; Kato, S. *Rev. Sci. Instrum.* **1992**, 63, 1551.
- (12) Reffner, J.A.; Martoglio, P.A.; Williams, G.P. *Rev. Sci. Instrum.* **1955**, 66, 1298.
- (13) Carr, G.L.; Reffner, J.A.; Williams, G.P. *Rev. Sci. Instrum.* **1995**, 66, 1490.

- (14) Carr, G.L. *Rev. Sci. Instrum.* **2001**, 72, 1613.
- (15) Miller, L.M.; Dumas, P. *Biochim. Biophys. Acta.* **2006**, 1758, 846.
- (16) McKellar, A.R.W. *J. Mol. Spectrosc.* **2010**, 262, 1.
- (17) Kydd, R.A.; Wieser, H.; Kiefer, W. *Spectrochim. Acta.* **1983**, 39 A, 173.
- (18) Banhegyi, G.; Play, P.; Fogarasi, G. *Spectrochim. Acta.* **1983**, 39 A, 761.
- (19) Zürcher, R.F.; Günthard, H.H. *Helv. Chem. Acta.* **1955**, 38, 849.
- (20) Lafferty, W.J. *Ph.D. thesis*, Massachusetts Institute of Technology, 1960.
- (21) Lebrumant, J.; *Cr. Acad.. Sci*, Paris, **1968**, 267, 946.
- (22) Chan, S.I.; Borgers, T.R.; Russell, J.W.; Strauss, H.L; Gwinn. W.D. *J. Chem. Phys.* **1966**, 44, 1103.
- (23) Kydd, R.A.; Wieser, H.; Danyluk, M. *J. Mol. Spectrosc.* **1972**, 44, 14.
- (24) Jokisaari, J.; Kauppinen, J. *J. Chem. Phys.* **1973**, 59, 2260.
- (25) Winnewisser, M.; Kunzmann, M.; Winnewisser, B. *J. Mol. Spectrosc.* **2001**, 561, 152.
- (26) Moruzzi, G.; Kunzmann, M.; Winnewisser, B.; Winnewisser, M. *J. Mol. Spectrosc.* **2003**, 219, 152.
- (27) Gaussian 09, Revision, B01; Gaussian, Inc.: Wallingford CT 2010.

## Chapter 3: Analysis of bands located between 700 and 900 $\text{cm}^{-1}$

### 3.1 Introduction

When the spectrum of oxetane was recorded, many new bands that were not previously described in the low resolution infrared studies<sup>1,2</sup> nor predicted by the quantum mechanical calculations, performed in this work and by Banhegyi *et al.*,<sup>2</sup> appeared in the spectrum. Examples of these bands are shown in Fig (3.1).

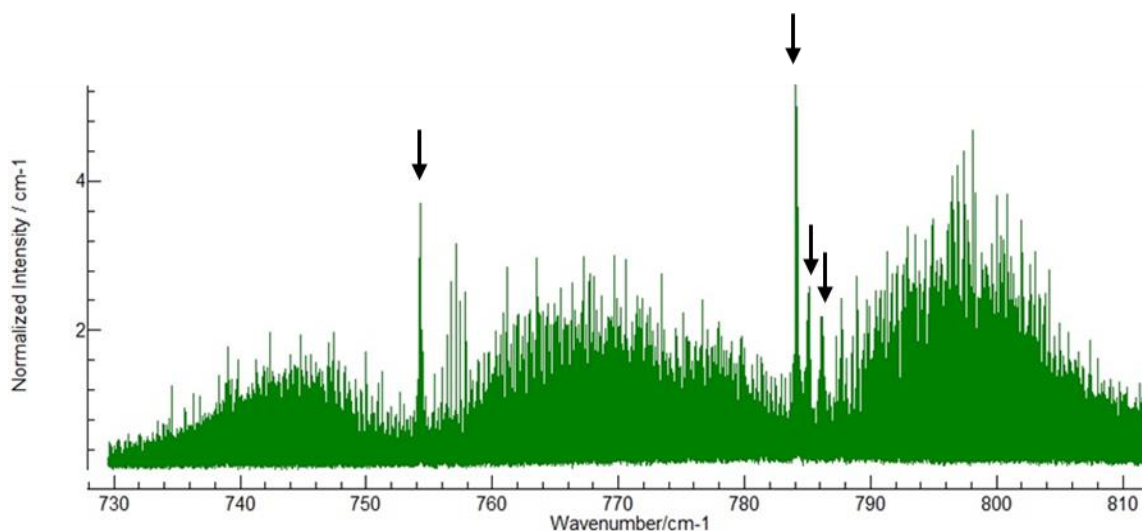


**Figure 3.1:** High resolution infrared spectrum of oxetane at 200 mTorr. These bands represent combinations between the ring puckering ( $\nu_{18}$ ) at  $53 \text{ cm}^{-1}$ , ( $2\nu_{18}$ ) at  $142 \text{ cm}^{-1}$ , ( $3\nu_{18}$ ) at  $247 \text{ cm}^{-1}$  and ( $4\nu_{18}$ ) at  $365 \text{ cm}^{-1}$ , and the  $\beta$ - $\text{CH}_2$ -rocking ( $\nu_{17}$ ) motion at  $702 \text{ cm}^{-1}$ .

It is shown in Fig (3.1) that at least three bands originate at about  $785 \text{ cm}^{-1}$ , marked by black arrows, and they are almost superimposed. The P-branches from this subset of bands overlap with the R-branch of a relatively isolated band appearing at  $754 \text{ cm}^{-1}$ . When these bands are compared to the spectrum of the ring puckering vibration in the Winnewisser *et*

*al.* work<sup>3</sup> in Fig (3.2), a similar pattern of the spacing between the Q-branches is observed. This raised the question: do these bands belong to a vibration that behaves as the ring puckering vibration? It was first necessary to identify the underlying vibrations of these bands. The rovibrational analysis of the bands that originate between 754 cm<sup>-1</sup> and 864 cm<sup>-1</sup> was performed which allowed an unambiguous vibrational assignment of these bands in Fig (3.1) and also the re-assignment of the ring deformation fundamental band which was mis-assigned in the literature.<sup>1,2</sup>

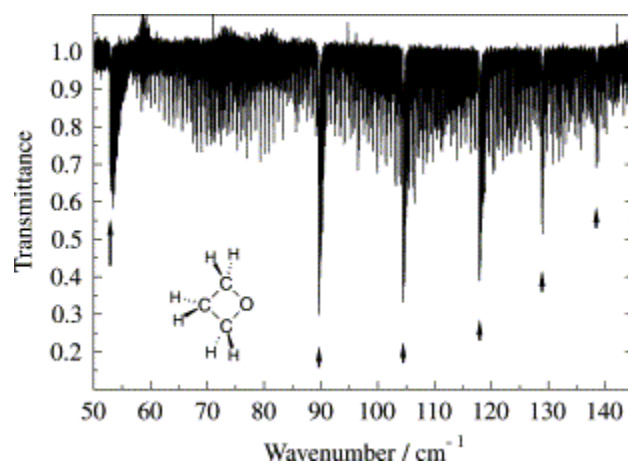


**Figure 3.2:**\* High resolution spectrum of oxetane showing the ring puckering fundamental and hot bands.  
\* Reprinted from ref. (1) with permission from Elsevier.

### 3.2 General procedure for the rovibrational analysis

A systematic procedure is needed in order to analyze rovibrational spectra which involve large numbers of transitions. The most convenient case arises when patterns of transitions are visually identified in the spectrum; otherwise, helpful tools such as

Loomis-Wood (LW) plots<sup>4</sup> are required. Analysis starts by comparing patterns of transitions in the experimental spectrum to the corresponding predicted spectrum. A predicted spectrum can be achieved by applying a model molecular Hamiltonian to eigenfunctions to calculate the eigenvalues of the rovibrational levels. This can be performed using programs such as PGOPHER<sup>5</sup> by including estimates of the most important Hamiltonian parameters: rotational and centrifugal distortion constants. These can often be found for the ground state from previous microwave studies and these can be used as a first guess for the excited state rotational parameters also. The approximate band origin for the vibration can be estimated from low resolution infrared studies or frequency calculations as a guide.

Analysis of the combination band ( $\nu_{17}+\nu_{18}$ ) at  $754\text{ cm}^{-1}$  is taken as an example to explain the general procedure that is followed to assign rovibrational transitions in this study. Since the spectrum is highly congested due to the presence of hot and combination bands which made the visual recognition of patterns difficult, patterns in the rotational structure of the simulated spectrum were inspected in order to determine the spacing between transitions that share a common quantum number. For example, part of a pattern with common  $K_a$  values (with different  $J$  values), is highlighted in the simulation in Fig (3.3).

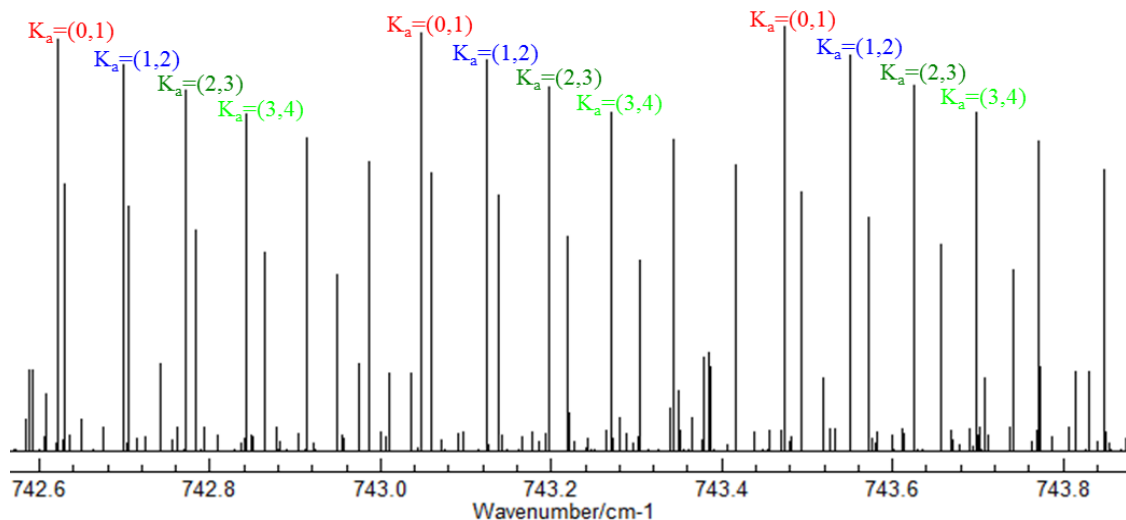


**Figure 3.3:** A simulation of the combination band ( $\nu_{17}+\nu_{18}$ ) at  $754\text{ cm}^{-1}$ , showing a part of a pattern with common  $K_a$  values in the P-branch using PGOPHER.<sup>5</sup>

The spacing in Fig. (3.3) between transitions for a particular  $K_a$  is ideally equal to  $2B$  where  $B$  is a rotational constant. This value is used to build a Loomis-Wood (LW) plot.<sup>4</sup> This plot stacks segments of the spectrum, each is  $2B$  long, on top of each other in order to show transitions within the same progression (common  $K_a$ ) as easily recognized series that run vertically in the plot as can be seen in Fig (3.4) which shows transitions in the P-branch. Consecutive triangles in a series in Fig (3.4), the red ones labeled as  $K_a=(0,1)$  as an example, correspond to consecutive lines with the same coloured label in Fig (3.3). Once progressions are identified, the individual transitions within each colour-coded series need to be assigned to the appropriate  $J$  quantum number. The y-axis in the LW plot is used to identify the approximate  $J$  ( $m=J$  for P branch,  $m=J+1$  for R branch) although this may be shifted by one or two levels in the early stages of the assignment as the excited state rotational parameters are not known. In this work, the experimental

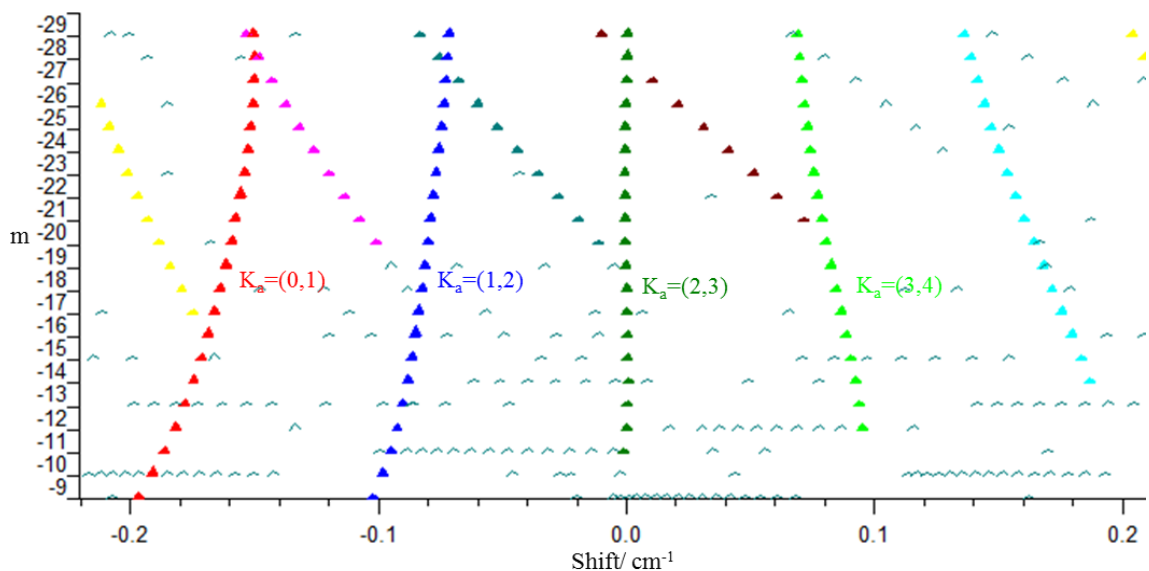


**Figure 3.4:** A Loomis-Wood Plot showing progressions in the P-branch of the combination band ( $\nu_{17}+\nu_{18}$ ) at  $754\text{ cm}^{-1}$ . The colours correspond to peaks labelled in Fig (3.3) that are part of a common  $K_a$  progression.

ground state combination differences (GSCDs) were compared to GSCDs from well-determined spectroscopic constants by Moruzzi *et al.*<sup>6</sup> in order to confirm the assignments of pairs of transitions in the P-branch and R-branch to the corresponding quantum numbers ( $J_{K_a K_c}$ ). Once sufficient numbers of transitions were assigned, they were least-squares fitted to Watson's A-reduced Hamiltonian in the  $I'$  representation<sup>7</sup> which is incorporated in PGOHER<sup>5</sup> and in Pickett's SPFIT/SPCAT programs<sup>8</sup> in order to determine preliminary spectroscopic constants of the excited state. In turn, this allowed prediction of more transitions using the preliminary parameters and this process was repeated to refine these parameters. Once line position of obvious simulated patterns are in agreement with the experiment using PGOPHER,<sup>5</sup> then the refined spectroscopic constants were used to produce a simulation using Pickett's SPCAT program.<sup>8</sup> This

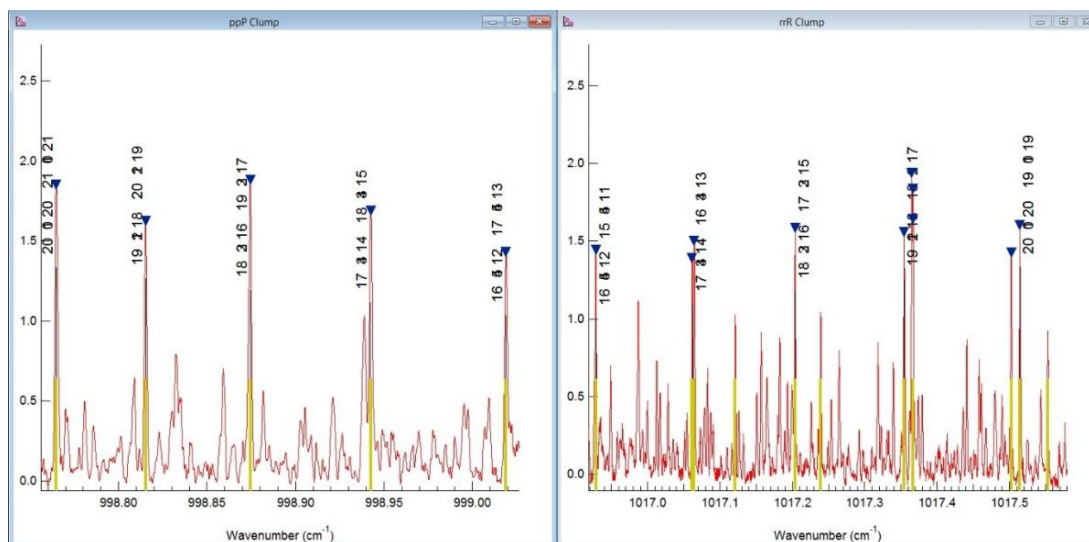


**Figure 3.5:** Spectral assignment in Igor Pro. The windows show part of a progression in the P-branch (left) and the corresponding R-branch (right) in the  $\nu_{23}$  band. The transitions are doubly degenerate in  $K_a$  which is reflected in the labels which are  $J K_a K_c$  (upper vibrational state)  $J K_a K_c$  (lower vibrational state).

simulation was then loaded to Igor Pro<sup>9</sup> which facilitated the assignment of patterns as shown in Fig (3.5). In this program, the simulated and experimental spectra are overlaid and the user can choose which transitions fit the current model Hamiltonian to include in the updated fit using Pickett's SPFIT program.<sup>10</sup> The process of spectral assignment and refinement of the spectroscopic constants is continued until all of the strong transitions of a band can be described by the model Hamiltonian used. By doing so, well-determined parameters in the excited state can be achieved. Also, rovibrational spectral analysis may provide refinement of the ground state parameters if more energy states are involved in the infrared work than in previous microwave studies.

### 3.3 Analysis of the combination bands between the ring puckering ( $\nu_{18}$ ) and the $\beta$ -CH<sub>2</sub>-rocking ( $\nu_{17}$ ) modes

The rovibrational analysis of the spectrum shown in Fig (3.1) allowed the bands in this portion of the spectrum to be identified. The following schematic diagram in Fig (3.6) describes the energies and symmetries of the vibrational states that are involved in this subset of vibrational transitions which represent combination bands between the ring puckering ( $\nu_{18}$ ) and the  $\beta$ -CH<sub>2</sub>-rocking ( $\nu_{17}$ ) vibrational modes. The assignment of a band to a particular vibrational mode is based on the rovibrational analysis and symmetry.

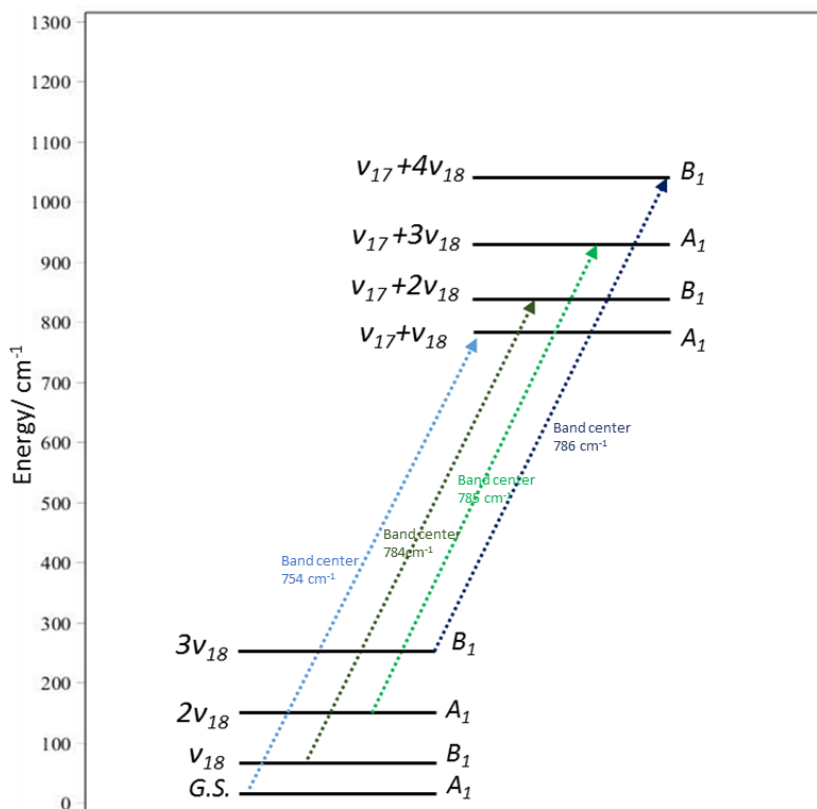


**Figure 3.6:** A schematic energy level diagram explaining the vibrational assignment of the bands in Fig (3.1).

### 3.3.1 The combination band $\nu_{17}+\nu_{18}$

The rovibrational analysis showed the band at  $754\text{cm}^{-1}$  follows *a-type* selection rules (i.e. the change in dipole moment accompanying this vibration occur along the a-inertial axis) and initiates in the ground vibrational state based on the GSCDs from the work of Moruzzi *et al.* Therefore, this band was assigned in this study to the combination band ( $\nu_{17}+\nu_{18}$ ) between the ring puckering ( $\nu_{18}$ ) mode at  $53\text{ cm}^{-1}$  and the  $\beta$ -CH<sub>2</sub>-rocking ( $\nu_{17}$ ) motion at  $702\text{ cm}^{-1}$ . By looking at the symmetry of each component, the  $\nu_{17}+\nu_{18}$  state is totally symmetric ( $B_1 \otimes B_1 = A_1$ ) as is the ground state. The direct product of the irreducible representations of the initial and final vibrational state wavefunctions and of the dipole component ( $\mu_a$ ) is  $A_1 \otimes A_1 \otimes A_1 = A_1$  totally symmetric (infrared active transition) as required which is consistent with this assignment.

Up to this point, 1180 transitions with the quantum number J values spanned over 3 to 37 and with  $K_a$  values up to 24 have been assigned to this combination band. The assigned transitions were fit using the Hamiltonian described earlier and the rms error value of this fit was  $0.000207\text{ cm}^{-1}$  which is a fraction of the FWHH of the transitions recorded. To describe the  $\nu_{17}+\nu_{18}$  state, eight parameters including the band origin, the rotational constants and the quartic centrifugal distortion constants except  $\delta_j$  were determined in this fit while the ground vibrational state parameters were held fixed to the values obtained by Moruzzi *et al.* The parameters of the fit are reported in Table 3.1. Transitions that are believed to be perturbed were excluded from the fit.

**Table (3.1):** Spectroscopic constants ( $\text{cm}^{-1}$ ) for the ground state <sup>6</sup> and excited state ( $\nu_{17}+\nu_{18}$ ).

	Ground State <sup>6</sup>	$\nu_{17}+\nu_{18}$
$G_v$	0	754.172015(32)
Rotational Constants		
$A$	0.40179332	0.4018971(75)
$B$	0.391405984	0.3913358(66)
$C$	0.224510678	0.22495814(26)
Quartic Centrifugal Distortion Constants ( $\times 10^8$ )		
$\Delta_J$	16.5254	15.809(40)
$\Delta_{JK}$	-4.68	-71.2(26)
$\Delta_K$	15.23	90.3(47)
$\delta_j$	5.4815	5.4815
$\delta_k$	-2.779	28.8(13)
Sextic Centrifugal Distortion Constants ( $\times 10^{12}$ )		
$\Phi_J$	0.627	0.627
$\Phi_{JK}$	0.8	0.8
$\Phi_{KJ}$	1.236	1.236
$\Phi_K$	-2.2	-2.2
$\varphi_j$	0.1	0.1
$\varphi_{jk}$	-0.897	-0.897
$\varphi_k$	-0.19	-0.19
rms error	0.000207	
No. transitions	1180	

Values in grey are fixed to values from reference <sup>6</sup>

A simulation of the spectrum was made based on the spectroscopic constants in Table 3.1. The agreement between the simulation and the experimental spectrum in Fig (3.7) shows that the preliminary sets of spectroscopic parameters obtained in this work for the  $\nu_{17}+\nu_{18}$  band at  $754 \text{ cm}^{-1}$  is descriptive of the strong unperturbed transitions.

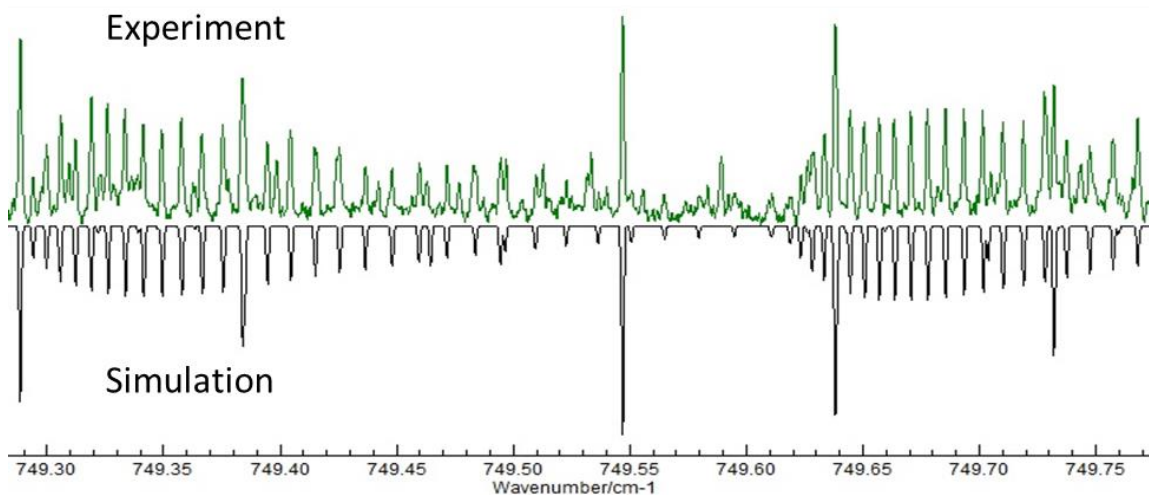


**Figure 3.7:** A comparison between the simulated and experimental transitions in a small region of the Q and P-branches of the  $\nu_{17}+\nu_{18}$  band.

### 3.3.2 The hot combination band $\nu_{17}+2\nu_{18} - \nu_{18}$

The rovibrational analysis of the band that originates at  $784\text{ cm}^{-1}$  shows that this vibrational transition initiates in the first ring puckering excited state at  $53\text{ cm}^{-1}$  which has  $B_1$  symmetry. The observed band contour follows *a-type* selection rules and hence, the final state must be of  $B_1$  symmetry so that the direct product of the wavefunctions corresponding to the initial and the final states and of the dipole moment component ( $\mu_a$ ) is  $B_1 \otimes A_1 \otimes B_1 = A_1$  to result in an infrared active transition. The combination state  $\nu_{17}+2\nu_{18}$  has the same symmetry of  $B_1$  from  $(B_1 \otimes A_1)$ , the symmetry of the final state, which confirms the vibrational assignment of this hot combination band to  $\nu_{17}+2\nu_{18} - \nu_{18}$  at  $784\text{ cm}^{-1}$ .

Preliminary work on this hot combination band allowed the assignment of 416 rovibrational transitions with quantum number  $J$  ranging between 5 and 26 and a

maximum  $K_a$  value of 14. Table 3.2 summarizes the spectroscopic parameters obtained by fitting these data. Seven parameters including the band origin, the rotational constants and the diagonal quartic centrifugal distortion constants for the  $\nu_{17}+2\nu_{18}$  state were allowed to float in this fit while the rest of the parameters were fixed to the values of Moruzzi *et al.* which correspond to the first excited vibrational state of ring puckering ( $\nu_{18}$ ). The rms error value for the fit was  $0.000378 \text{ cm}^{-1}$ . This value is higher than expected, based on other bands and suddenly rose when transitions that had a  $J$  value of more than 26 were included in the fit. This sudden rise in the rms error value is a sign of perturbations in this band which have not been treated in this work.

**Table (3.2):** Spectroscopic constants ( $\text{cm}^{-1}$ ) of  $\nu_{18}$  and  $\nu_{17}+2\nu_{18}$  states.

	$\nu_{18}$ <sup>6</sup>	$\nu_{17}+2\nu_{18}$
$G_v$	52.920348	837.278182(99)
Rotational Constants		
$A$	0.402209858	0.401865(23)
$B$	0.391155554	0.390961(20)
$C$	0.22589666	0.22583195(92)
Quartic Centrifugal Distortion Constants ( $\times 10^8$ )		
$\Delta J$	16.6282	29.19(16)
$\Delta_{JK}$	-21.5803	-48.5(12)
$\Delta_K$	32.248	28.5(17)
$\delta_j$	5.3811	5.3811
$\delta_k$	5.9528	5.9528
Sextic Centrifugal Distortion Constants ( $\times 10^{12}$ )		
$\Phi_J$	0.537	0.537
$\Phi_{JK}$	-1.79	-1.79
$\Phi_{KJ}$	1.93	1.93
$\Phi_K$	-0.397	-0.397
$\varphi_j$	0.097	0.097
$\varphi_{jk}$	0.54	0.54
$\varphi_k$	0.871	0.871
rms error	0.000378	
No. transitions		416

Values in grey are fixed to values from reference <sup>6</sup>

### 3.3.3. The hot combination band $\nu_{17}+3\nu_{18} - 2\nu_{18}$

In a similar fashion to the analysis of the  $(\nu_{17}+2\nu_{18} - \nu_{18})$  and  $(\nu_{17}+\nu_{18})$  bands, it was found based on a preliminary rovibrational analysis of the band centered at  $785 \text{ cm}^{-1}$  that this band obeys *a-type* selection rules and initiates in the second ring puckering excited state at  $154 \text{ cm}^{-1}$  which has  $A_1$  symmetry. The infrared activity of this band means that the final state is also of  $A_1$  symmetry as discussed above. The combination state  $\nu_{17}+3\nu_{18}$  at  $928 \text{ cm}^{-1}$  meets this requirement ( $B_1 \otimes B_1 = A_1$ ). Therefore, the band that appear at  $785 \text{ cm}^{-1}$  is assigned to  $(\nu_{17}+3\nu_{18} - 2\nu_{18})$ .

Initially, 84 transitions were assigned to this hot combination band in order to confirm the vibrational assignment of this subset of bands. A preliminary fit of the assigned transitions is summarized in Table 3.3. The rms error value of this preliminary fit is  $0.00200 \text{ cm}^{-1}$  which is very high since only the band origin and the rotational constants  $A$  and  $C$  in the  $\nu_{17}+3\nu_{18}$  state were allowed to vary. Assignment of more transitions is needed in order to have more spectroscopic parameters determined.

**Table (3.3):** Spectroscopic constants ( $\text{cm}^{-1}$ ) of the  $\nu_{17}+3\nu_{18}$  and  $2\nu_{18}$ <sup>6</sup> states.

	$2\nu_{18}$ <sup>6</sup>	$\nu_{17}+3\nu_{18}$
$G_v$	142.579784	927.8155(10)
Rotational Constants		
$A$	0.402243871	0.401628(27)
$B$	0.390900214	0.390900214
$C$	0.22645821	0.2247944(57)
Quartic Centrifugal Distortion Constants ( $\times 10^8$ )		
$\Delta_J$	16.127	16.127
$\Delta_{JK}$	-15.11	-15.11
$\Delta_K$	26.168	26.168
$\delta_j$	5.5755	5.5755
$\delta_k$	3.223	3.223
Sextic Centrifugal Distortion Constants ( $\times 10^{13}$ )		
$\Phi_J$	4.87	4.87
$\Phi_{JK}$	-0.2	-0.2
$\Phi_{KJ}$	-3.3	-3.3
$\Phi_K$	2.1	2.1
$\varphi_j$	0.83	0.83
$\varphi_{jk}$	-0.47	-0.47
$\varphi_k$	9.94	9.94
rms error	0.00200	
No. transitions		84

Values in grey are fixed to values from reference <sup>6</sup>

### 3.3.4. The hot combination band $\nu_{17}+4\nu_{18} - 3\nu_{18}$

The band at  $786 \text{ cm}^{-1}$  also follows *a-type* selection rules and originates in the third ring puckering excited state at  $259 \text{ cm}^{-1}$  which has  $B_1$  symmetry. Due to similar symmetry considerations for  $(\nu_{17}+2\nu_{18} - \nu_{18})$ , the combination state  $\nu_{17}+4\nu_{18}$  at  $1033 \text{ cm}^{-1}$  is the final state as it has the right symmetry  $B_1$  from  $(B_1 \otimes A_1)$ .

Preliminary work on this hot combination band allowed the assignment of 360 transitions with the quantum number  $J$  values spanning from 9 to 30 and with  $K_a$  values up to 16. The assigned transitions were fitted as described above and the rms error value

of the fit was  $0.000231 \text{ cm}^{-1}$ . Six spectroscopic parameters were allowed to be determined in this fit while the rest of parameters were held fixed to the values from the Moruzzi *et al.* work<sup>6</sup> which correspond to the third excited vibrational state of the ring puckering ( $3\nu_{18}$ ). Spectroscopic constants obtained in this fit are reported in Table 3.4.

**Table (3.4):** Spectroscopic constants ( $\text{cm}^{-1}$ ) of the  $3\nu_{18}$ <sup>6</sup> and  $\nu_{17}+4\nu_{18}$  states.

	$3\nu_{18}$ <sup>6</sup>	$\nu_{17}+4\nu_{18}$
$G_v$	247.044598	1033.366315(64)
Rotational Constants		
$A$	0.402289516	0.4020474(57)
$B$	0.390602805	0.3902271(50)
$C$	0.22714785	0.22637358(37)
Quartic Centrifugal Distortion Constants ( $\times 10^8$ )		
$\Delta_J$	16.171	16.283(35)
$\Delta_{JK}$	-15.208	-15.208
$\Delta_K$	26.281	25.28(20)
$\delta_j$	5.4991	5.4991
$\delta_k$	3.563	3.563
Sextic Centrifugal Distortion Constants ( $\times 10^{13}$ )		
$\Phi_J$	4.07	4.07
$\Phi_{JK}$	-5.7	-5.7
$\Phi_{KJ}$	8.02	8.02
$\Phi_K$	-2.3	-2.3
$\varphi_j$	0.9	0.9
$\varphi_{jk}$	2.03	2.03
$\varphi_k$	5.94	5.94
rms error	0.000231	
No. transitions		360

Values in grey are fixed to values from reference <sup>6</sup>

This set of hot combination bands was mistakenly assigned by Kydd *et al.*<sup>1</sup> to the ring deformation band ( $\nu_8$ ). This is incorrect because with the benefit of rotational resolution, the spectra in this work confirm that the lower state is not the ground state which

excludes this from being a fundamental band. The correct assignment of the  $\nu_8$  mode is described next.

### 3.4 Analysis of the ring deformation fundamental band ( $\nu_8$ )

The next higher frequency band at  $839\text{ cm}^{-1}$  as shown in Fig (3.8) follows *a-type* selection rules and its GSCDs correspond to the ground vibrational state from the Moruzzi *et al.* work.<sup>6</sup> As a result, this band is assigned to the ring deformation fundamental ( $\nu_8$ ) mode.

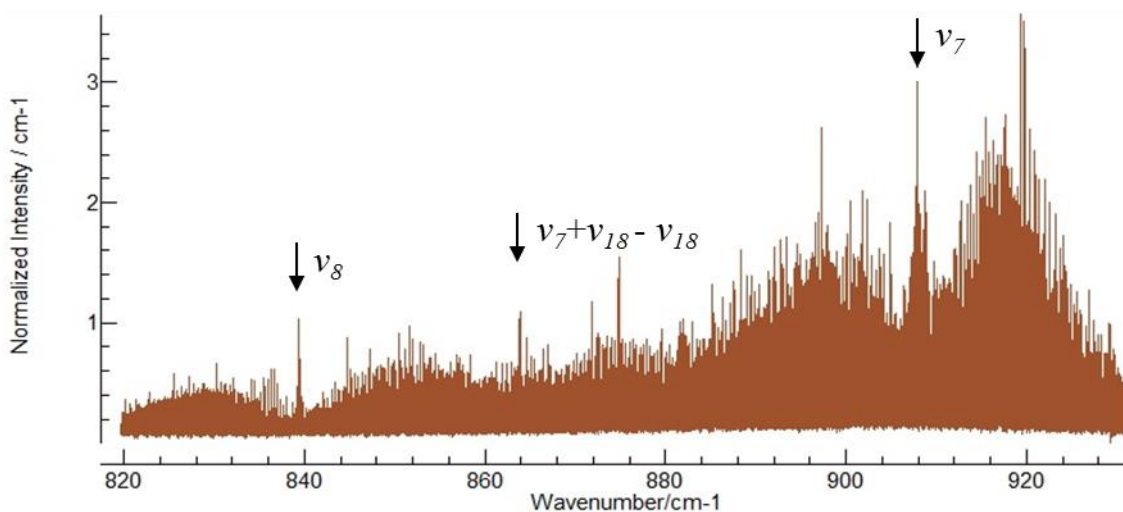


**Figure 3.8:** High resolution infrared spectrum of oxetane at 10 mTorr showing the bands  $\nu_7$ ,  $\nu_7 + \nu_{18} - \nu_{18}$  and  $\nu_8$ . The features involving  $\nu_7$  and  $\nu_7 + \nu_{18} - \nu_{18}$  will be discussed in Chapter 6.

A total of 842 rovibrational transitions with the quantum number  $J$  values ranging between 5 and 43 and with  $K_a$  values up to 24 were assigned to this fundamental and they were fitted using the Hamiltonian used earlier in this work. Table 3.5 reports the spectroscopic parameters of the fitted rovibrational transitions. Seven parameters in the  $\nu_8$  state were allowed to float. Only transitions that are believed to be unperturbed were included in the fit which has an rms error value of  $0.000235 \text{ cm}^{-1}$ .

**Table (3.5):** Spectroscopic constants ( $\text{cm}^{-1}$ ) for the ground state <sup>6</sup> and  $\nu_8$  state.

	Ground State <sup>6</sup>	$\nu_8$
$G_v$	0	839.296672(39)
Rotational Constants		
$A$	0.40179332	0.4021448(54)
$B$	0.391405984	0.3910361(47)
$C$	0.224510678	0.22344567(35)
Quartic Centrifugal Distortion Constants ( $\times 10^8$ )		
$\Delta_J$	16.5254	10.678(62)
$\Delta_{JK}$	-4.68	-19.68(35)
$\Delta_K$	15.23	57.91(39)
$\delta_j$	5.4815	5.4815
$\delta_k$	-2.779	-2.779
Sextic Centrifugal Distortion Constants ( $\times 10^{12}$ )		
$\Phi_J$	0.627	0.627
$\Phi_{JK}$	0.8	0.8
$\Phi_{KJ}$	1.236	1.236
$\Phi_K$	-2.2	-2.2
$\varphi_j$	0.1	0.1
$\varphi_{jk}$	-0.897	-0.897
$\varphi_k$	-0.19	-0.19
rms error		0.000235
No. transitions		842

Values in grey are fixed to values from reference <sup>6</sup>

The assignment of this band to the ring deformation fundamental ( $\nu_8$ ) at  $839 \text{ cm}^{-1}$  in this work is supported by the fact that this band obeys *a-type* selection rules and has

GSCDs that correspond to the ground vibrational state. Kydd *et al.*<sup>1</sup> in their low resolution infrared work assigned this band at  $\sim 840\text{ cm}^{-1}$  to the out-of-plane  $\alpha\text{-CH}_2$ -rocking mode which occurs along the molecular *c*-axis and would result in a *c-type* band. This assignment is based on one feature in their spectra which is the presence of a sharp Q-branch around  $840\text{ cm}^{-1}$ , however, both *a* and *c-type* band contours have this feature. Patterns of transitions of this band which depend on the rotational constants in the ground state, which is well determined from the work of Moruzzi *et al.*,<sup>6</sup> and the excited vibrational state from this work are connected by transitions of *a-type* symmetry. The ring deformation mode ( $\nu_8$ ) is totally symmetric as is the ground vibrational state. The direct product of the wavefunctions corresponding to these states and of the dipole moment component ( $\mu_a$ ) is  $A_1 \otimes A_1 \otimes A_1 = A_1$  confirms that this is an infrared active transition. Moreover, quantum mechanical calculations using MP2/6-31++ (2d, 2p) predict that the  $\alpha\text{-CH}_2$ -rocking fundamental band is much higher at  $1097\text{ cm}^{-1}$  which is inconsistent with the assignment of Kydd *et al.*<sup>1</sup>

In the *ab initio* study using SCF theory by Banhegyi *et al.*,<sup>2</sup> they suggested that the band at  $839\text{ cm}^{-1}$  is a combination band between the ring deformation mode ( $\nu_8$ ) which is of  $A_1$  symmetry and the ring puckering mode at  $53\text{ cm}^{-1}$  which has  $B_1$  symmetry. Such a combination has the symmetry of  $B_1$  from ( $A_1 \otimes B_1$ ) which should result in a band with *c-type* selection rules which is inconsistent with the rovibrational spectra analyzed in this thesis. Furthermore, their assignment relied on the mis-assignment by Kydd *et al.* for the bands discussed in Section 3.3.

### 3.5 Summary

The rovibrational analysis of the high resolution infrared spectrum of oxetane in the region of study reveals the existence of many many more vibrational transitions in addition to what was suggested in previous low resolution infrared studies. The vibrational energy levels of the ring puckering mode in oxetane are closely spaced<sup>1-5</sup> which allows a noteworthy distribution of oxetane molecules among the first few vibrational states of this normal mode at room temperature. This distribution results in many hot bands that initiate in excited vibrational states of ring puckering. When these states couple with states from other normal modes, these bands are also expected to appear in this region of the spectrum. In particular for oxetane, the ring puckering energy levels are not evenly spaced leading to unusually large gaps between the band originating in  $v=0$  and the first hot band of a given vibration as seen in Fig (3.1) and Fig (3.2). This caused mis-assignments in the past as the spectra appear as two separate bands.

Rotationally resolved spectra provide more information than low resolution ones do and therefore, the band centers of fundamentals are correctly identified during the rovibrational analysis of the spectrum. In this study, the ring deformation fundamental is assigned at  $839\text{ cm}^{-1}$  rather than  $785\text{ cm}^{-1}$ <sup>2</sup> and many hot and combination bands were assigned in this part of the spectrum that were never reported before now:  $\nu_{17}+\nu_{18}$  at  $754\text{ cm}^{-1}$ ,  $\nu_{17}+2\nu_{18}-\nu_{18}$  at  $784\text{ cm}^{-1}$ ,  $\nu_{17}+3\nu_{18}-2\nu_{18}$  at  $785\text{ cm}^{-1}$ ,  $\nu_{17}+4\nu_{18}-3\nu_{18}$  at  $786\text{ cm}^{-1}$ .

## References

- (1) Kydd, R.A.; Wieser, H.; Kiefer, W. *Spectrochim. Acta.* **1983**, 39A, 173.
- (2) Banhegyi, G.; Play, P.; Fogarasi, G. *Spectrochim. Acta.* **1983**, 39A, 761.
- (3) Winnewisser, M.; Kunzmann, M.; Winnewisser, B. *J. Mol. Spectrosc.* **2001**, 561, 152.
- (4) Loomis, F.W.; Wood, R.W. *Phys. Rev.* **1928**, 32, 223.
- (5) Western, C.M. *J. Quant. Spectrosc. Ra*, **2016**, 186, 221.
- (6) Moruzzi, G.; Kunzmann, M.; Winnewisser, B.; Winnewisser, M. *J. Mol. Spectrosc.* **2003**, 219, 152.
- (7) Watson, J.K.G. In *Vibrational Spectra and Structure*; Durig, J. Ed; Vol. VI; Elsevier: Amsterdam, 1977.
- (8) Pickett, H.M. *J. Mol. Spectrosc.* **1991**, 148, 371.
- (9) IGOR Pro; WaveMetric Inc. Lake Oswego OR 2008.

## **Chapter 4: Preliminary analysis of C-O asymmetric stretch fundamental ( $\nu_{23}$ ) at 1008 cm<sup>-1</sup> and its hot bands $\nu_{23}$ , $\nu_{18}+\nu_{23} - \nu_{18}$ and $2\nu_{18}+\nu_{23} - 2\nu_{18}$**

### **4.1 Introduction**

It was shown in the previous chapter that there is extensive overlap among many bands in the region between 700-950 cm<sup>-1</sup> which makes it necessary to analyse these bands simultaneously as there are believed to be interactions due to the closeness of the energy of these vibrations. Therefore, the focus in this chapter is given to the portion of the spectrum that looked isolated from these overlapping bands at lower frequency. At the same time, this part has the highest infrared intensity in the region of study. The rovibrational analysis of this portion revealed that it is due to the excitation of the asymmetric stretch of C-O: the fundamental and two hot bands starting at different vibrational levels of ring puckering and ending in coupled states between these two vibrations. Preliminary analysis of the  $\nu_{23}$  fundamental band at 1008 cm<sup>-1</sup> as outlined in this chapter showed that many of the rovibrational energy levels in  $\nu_{23}$  are perturbed by Coriolis interactions; their treatment will be covered in later chapters.

### **4.2 Assignment of the C-O asymmetric stretch fundamental ( $\nu_{23}$ )**

The part of the spectrum of oxetane in Fig (4.1) is the most intense in the region of study and looks isolated from the low frequency bands seen in Fig (2.2). What can be seen here is a contour of a *b-type* band which was vibrationally assigned by Kydd *et al.*<sup>1</sup> to a B<sub>2</sub> symmetry species at 1008 cm<sup>-1</sup> in their low resolution infrared work. It corresponds to the in- plane asymmetric stretch of C-O. In fact, more *b-type* bands that

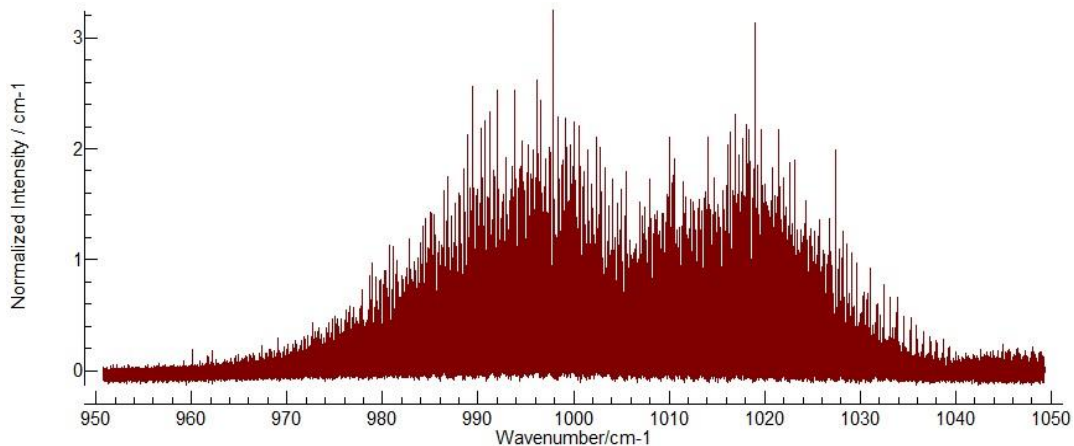


**Figure 4.1:** High resolution infrared spectrum of oxetane at 5 mTorr. In this region, the bands  $\nu_{23}$ ,  $\nu_{18} + \nu_{23} - \nu_{18}$  and  $2\nu_{18} + \nu_{23} - 2\nu_{18}$  were rovibrationally analyzed.

are almost superimposed with each other were identified in this region of the spectrum and are discussed in section 4.3. The rovibrational analysis of this band confirms the vibrational assignment of Kydd *et al.* of this fundamental mode, however, a more precise band center was achieved in this work as it can be difficult to assign band centers from low resolution data when there is no sharp Q branch as in this case.

According to the procedure of analysis described earlier, the assignment of the rovibrational transitions and the refinement of the preliminarily-used Hamiltonian parameters were continued up to a point where the rms value of the fit became large suddenly. That suggested perturbations were present in the spectrum where rovibrational transition positions cannot be predicted by the model Hamiltonian used. Up to this point, 1016 transitions were fit using Watson's A-reduced Hamiltonian in the  $I'$  representation.<sup>2</sup> in Pickett's SPFIT program.<sup>3</sup> Preliminary rotational constants  $A$ ,  $B$  and  $C$  and the centrifugal distortion constants  $\Delta_J$ ,  $\Delta_{JK}$  and  $\Delta_K$  in the excited state were allowed to vary in

the fit of the unperturbed transitions. The rest of the centrifugal distortion constants in the  $\nu_{23}$  state in addition to the ground state spectroscopic constants were fixed to the corresponding values in the ground vibrational state obtained by Moruzzi *et al.*<sup>4</sup> The rms error value of this fit was 0.000213  $\text{cm}^{-1}$ . These parameters are summarized in Table 4.1. More refined spectroscopic constants for the  $\nu_{23}$  state will be presented at the end of this thesis following a global analysis of this and its interacting states.

**Table (4.1):** Spectroscopic constants ( $\text{cm}^{-1}$ ) for the ground <sup>4</sup> and  $\nu_{23}$  states.

	Ground State <sup>4</sup>	$\nu_{23}$
$G_v$	0	1008.364321(34)
Rotational Constants		
$A$	0.40179332	0.4003218(51)
$B$	0.391405984	0.3901291(46)
$C$	0.224510678	0.22458181(11)
Quartic Centrifugal Distortion Constants ( $\times 10^8$ )		
$\Delta_J$	16.5254	17.1532(61)
$\Delta_{JK}$	-4.68	-3.007(88)
$\Delta_K$	15.23	15.74(16)
$\delta_j$	5.4815	5.4815
$\delta_k$	-2.779	-2.779
Sextic Centrifugal Distortion Constants ( $\times 10^{12}$ )		
$\Phi_J$	0.627	0.627
$\Phi_{JK}$	0.8	0.8
$\Phi_{KJ}$	1.236	1.236
$\Phi_K$	-2.2	-2.2
$\varphi_j$	0.1	0.1
$\varphi_{jk}$	-0.897	-0.897
$\varphi_k$	-0.19	-0.19
rms error	0.000213	
No. transitions	1016	

Values in grey are fixed to values from reference <sup>4</sup>

Inspection of the spectrum for this band Fig (4.1) showed progressions that belong to other bands than this fundamental. Neither the quantum mechanical calculations nor the low resolution infrared study<sup>1</sup> suggests the existence of these bands as fundamental vibrations. Their assignment is discussed in section 4.3.

#### 4.3 Analysis of the C-O asymmetric stretch hot bands $\nu_{18} + \nu_{23} - \nu_{18}$ and $2\nu_{18} + \nu_{23} - 2\nu_{18}$

In a similar fashion to the assignment of rovibrational transitions discussed earlier, a total of 516 transitions were found to belong to another band other than the  $\nu_{23}$  fundamental. The rovibrational analysis of this band revealed that it follows *b-type* selection rules (i.e. the change in dipole moment accompanying this vibration should occur along the inertial b-axis). That dipole component corresponds to B<sub>2</sub> symmetry in the C<sub>2v</sub> character table. In addition, this vibrational transition initiates in the first ring puckering vibrational state ( $\nu_{18}$ ) at 53 cm<sup>-1</sup> that was confirmed using well-determined GSCDs from the Moruzzi *et al.* work.<sup>4</sup> Based on C<sub>2v</sub> symmetry, the  $\nu_{18}$  vibration has B<sub>1</sub> symmetry while the coupled state between the first ring puckering vibrational level and the first vibrational level of in- plane asymmetric stretch of C-O,  $\nu_{18} + \nu_{23}$  has the symmetry of B<sub>1</sub>  $\otimes$  B<sub>2</sub> = A<sub>2</sub>. Since the direct product of the irreducible representations of the initial and the final vibrational state wavefunctions and of the dipole moment component along the b axis A<sub>2</sub>  $\otimes$  B<sub>2</sub>  $\otimes$  B<sub>1</sub> = A<sub>1</sub> is totally symmetric (infrared active transition), this hot band was assigned to ( $\nu_{18} + \nu_{23} - \nu_{18}$ ). A schematic illustration that describes the vibrational levels including their energies and symmetries involved in this

spectral region:  $\nu_{23}$ ,  $\nu_{18} + \nu_{23} - \nu_{18}$  and  $2\nu_{18} + \nu_{23} - 2\nu_{18}$ , is shown in the following energy diagram Fig. (4.2).

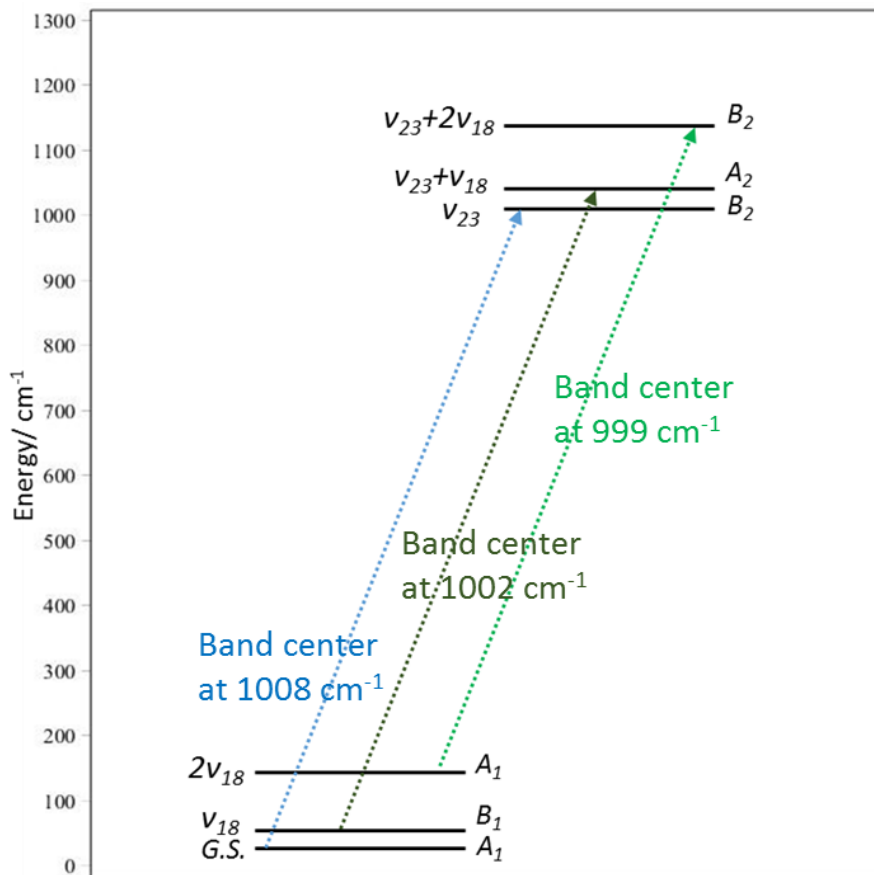


**Figure 4.2:** A schematic energy diagram explaining the vibrational assignment of the bands:  $\nu_{23}$ ,  $\nu_{18} + \nu_{23} - \nu_{18}$  and  $2\nu_{18} + \nu_{23} - 2\nu_{18}$ .

Progressions of rovibrational transitions that have quantum number J values ranging from 5 to 31 and values of  $K_a$  up to 14 in the P-branch and R-branch were assigned. The data were fitted to the Hamiltonian described earlier. The rms error value of this fit was  $0.000323 \text{ cm}^{-1}$ . The fitted and fixed parameters are summarized in Table 4.2.

**Table (4.2):** Spectroscopic constants ( $\text{cm}^{-1}$ ) for the  $\nu_{18}+\nu_{23}$  and  $\nu_{18}^4$  states.

	$\nu_{18}^4$	$\nu_{18}+\nu_{23}$
$G_v$	52.920348	1054.448596(85)
Rotational Constants		
$A$	0.402209858	0.402256(16)
$B$	0.391155554	0.389721(14)
$C$	0.225896666	0.22620929(46)
Quartic Centrifugal Distortion Constants ( $\times 10^8$ )		
$\Delta_J$	16.6282	18.261(52)
$\Delta_{JK}$	-21.5803	-32.39(34)
$\Delta_K$	32.248	91.42(53)
$\delta_j$	5.3811	5.3811
$\delta_k$	5.9528	5.9528
Sextic Centrifugal Distortion Constants ( $\times 10^{12}$ )		
$\Phi_J$	0.537	0.537
$\Phi_{JK}$	-1.79	-1.79
$\Phi_{KJ}$	1.93	1.93
$\Phi_K$	-0.397	-0.397
$\varphi_j$	0.097	0.097
$\varphi_{jk}$	0.54	0.54
$\varphi_k$	0.871	0.871
rms error	0.000323	
No. transitions		516
Values in grey are fixed to values from reference <sup>4</sup>		

Additional progressions to those identified for the  $\nu_{23}$  band at  $1008 \text{ cm}^{-1}$  and  $\nu_{18}+\nu_{23}$  -  $\nu_{18}$  band at  $1002 \text{ cm}^{-1}$  were identified which suggested that these progressions belong to another hot band. The second hot band, illustrated in Fig (4.2), in this region of the spectrum was found to originate at  $999 \text{ cm}^{-1}$ . The band follows *b-type* selection rules; hence, it belongs to the same symmetry species as the previous hot band. Supported by GSCDs values from the Moruzzi *et al.* work,<sup>4</sup> it was found that the initial state for this hot band is the second excited vibrational state of the ring puckering ( $2\nu_{18}$ ) at  $143 \text{ cm}^{-1}$ . As a result, the final state is a coupled state between the second ring puckering vibrational state and the first vibrational state of in-plane asymmetric stretch of C-O,

( $2\nu_{18}+\nu_{23}$ ) which is of  $B_2$  symmetry ( $A_1 \otimes B_2$ ). The direct product of the initial, the final and the dipole component symmetries  $B_2 \otimes B_2 \otimes A_1 = A_1$  confirms the vibrational assignment of this hot band to  $2\nu_{18}+\nu_{23} - 2\nu_{18}$  at  $999 \text{ cm}^{-1}$ .

Progressions of rovibrational transitions with the quantum number  $J$  values ranging between  $J=6$  and  $J=28$  and of  $K_a$  values up to 15 in the P-branch and R-branch were identified. Before now, 400 transitions were assigned to this hot band and were fitted using the model Hamiltonian used earlier in this work. The rms error value of this fit was  $0.000215 \text{ cm}^{-1}$ . Spectroscopic parameters along with the literature values are reported in Table (4.3).

**Table (4.3):** Spectroscopic constants ( $\text{cm}^{-1}$ ) for the  $2\nu_{18}+\nu_{23}$  and  $2\nu_{18}^4$  states.

	$2\nu_{18}^4$	$2\nu_{18}+\nu_{23}$
$G_v$	142.579784	1141.344073(60)
Rotational Constants		
$A$	0.402243871	0.4008564(94)
$B$	0.390900214	0.3895381(83)
$C$	0.22645821	0.22635724(42)
Quartic Centrifugal Distortion Constants ( $\times 10^8$ )		
$\Delta_J$	16.127	13.506(58)
$\Delta_{JK}$	-15.11	-52.15(40)
$\Delta_K$	26.168	83.89(65)
$\delta_j$	5.5755	5.5755
$\delta_k$	3.223	3.223
Sextic Centrifugal Distortion Constants ( $\times 10^{13}$ )		
$\Phi_J$	4.87	4.87
$\Phi_{JK}$	-0.2	-0.2
$\Phi_{KJ}$	-3.3	-3.3
$\Phi_K$	2.1	2.1
$\varphi_j$	0.83	0.83
$\varphi_{jk}$	-0.47	-0.47
$\varphi_k$	9.94	9.94
rms error	0.000215	
No. transitions	400	

Values in grey are fixed to values from reference <sup>4</sup>

Rovibrational transitions that have low values of the quantum number  $J$  in these hot bands were fitted nicely using the previously described Hamiltonian until perturbations due to Coriolis interactions appeared during the assignment of the spectrum. In Fig (4.3), a comparison is shown between a portion of the high resolution infrared spectrum of oxetane and the corresponding simulation which was produced using the spectroscopic parameters obtained in this study. In this comparison, the simulations of the three bands ( $\nu_{23}$  at  $1008\text{ cm}^{-1}$ ,  $\nu_{18}+\nu_{23}-\nu_{18}$  at  $1002\text{ cm}^{-1}$  and  $2\nu_{18}+\nu_{23}-2\nu_{18}$  at  $999\text{ cm}^{-1}$ ) are labeled in different colors. This region shows the congestion of the oxetane spectrum in this study. The good agreement between the simulation and the experiment shows that the preliminary sets of spectroscopic parameters obtained in this work are descriptive of the strong unperturbed transitions in these three bands and shows that some transitions in the  $\nu_{23}$  band, marked by black arrows, are shifted from their predicted position. That is a sign of perturbations.

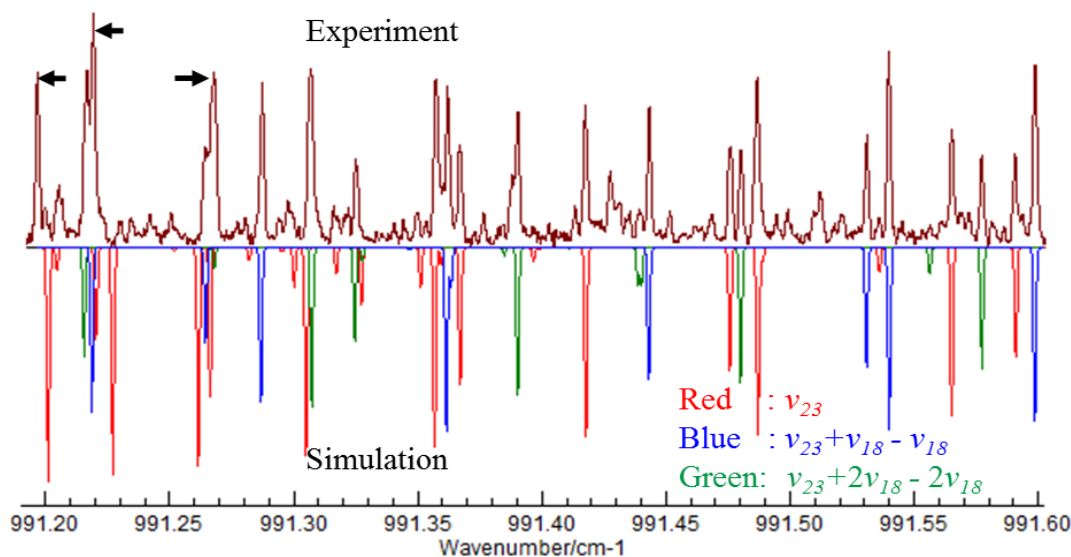


**Figure 4.3:** A comparison between the simulation and the spectrum of the  $\nu_{23}$ ,  $\nu_{18}+\nu_{23}-\nu_{18}$  and  $2\nu_{18}+\nu_{23}-2\nu_{18}$  bands.

#### 4.4. Perturbations in the C-O asymmetric stretch fundamental

Inspection of the C-O asymmetric stretch fundamental spectrum with the aid of a Loomis-Wood (LW) plot<sup>5</sup> allowed trends in the perturbed transitions in this band to be identified. These perturbations can be easily seen in the LW plot shown in Fig (4.4) in which the sudden shift in progressions of rovibrational transitions are identified.

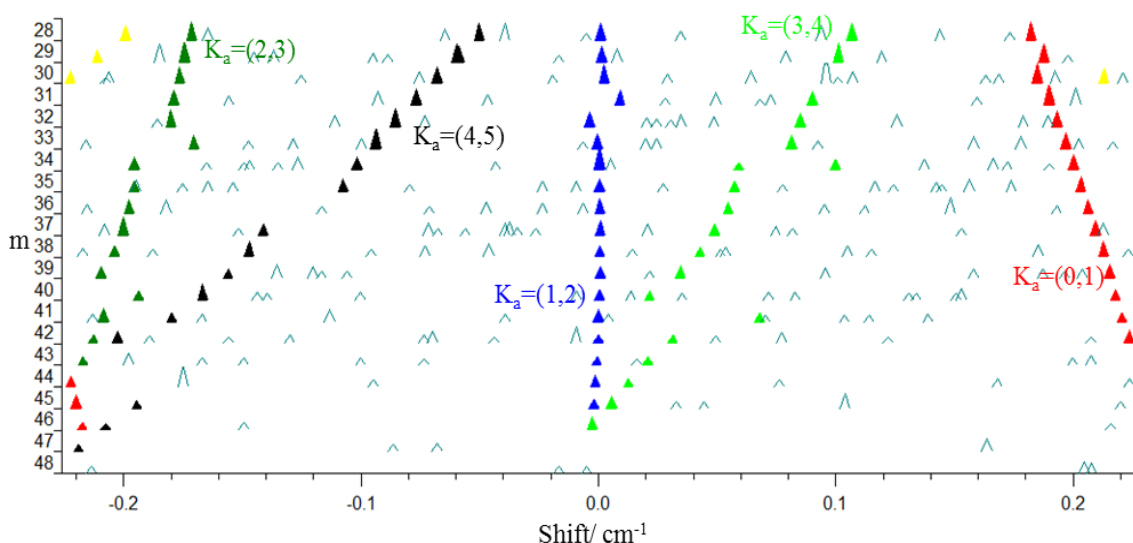


**Figure 4.4:** LW plot of the high resolution infrared spectrum of oxetane between 1021 and 1031  $\text{cm}^{-1}$  in which progressions of rovibrational transitions in the fundamental  $\nu_{23}$  are highlighted.

Coriolis forces are thought to be responsible for the perturbations seen in this figure. In fact, they could occur if the rotational levels are close in energy and have the correct symmetry for Coriolis interactions and result in energy shifts from the unperturbed energy levels. For rovibrational transitions that have  $K_a$  values of (0,1) and (1,2) which are labeled with red and blue, respectively, local perturbations can be seen in Fig (4.4)

where only a few transitions are shifted off the straight trend of the progression at about the quantum number  $J$  values of 28 and 29. In this case, unperturbed transitions beyond the perturbation sites could be assigned using the same preliminary Hamiltonian as the lower  $J$  values before the onset of this shift, however, including new terms that describe energy shifts due Coriolis forces are needed in order to assign the perturbed transitions. For rovibrational transitions that have higher  $K_a$  values, the case is more complicated. It can be seen in the LW plot for the  $K_a$  values of (2, 3), (3, 4) and (4, 5) which are labeled with green, lime and black, respectively, that perturbations extend over a wider range of transitions. It is also seen that many more transitions deviate from the straight trend of each of these three progressions. Since large numbers of the rovibrational transitions in progressions with  $K_a$  values  $\geq (2, 3)$  are perturbed, it is necessary to include perturbation terms to improve the model Hamiltonian.

#### **4.5. Summary**

The analysis of the highest infrared intensity portion of the rovibrational spectrum of oxetane, shown in Fig (4.1), was performed. That revealed the presence of a subset of overlapping bands that are nearly superimposed. This subset of bands are due to the excitation of the in-plane asymmetric stretch of C-O starting at different vibrational levels of ring puckering and ending in coupled states between these two vibrations. These bands were found to have perturbations due Coriolis interactions. Due to the challenges introduced by the ring puckering motion, only perturbations in the  $\nu_{23}$  fundamental at  $1008\text{ cm}^{-1}$  were analysed in this work. It was found that many of the rovibrational energy levels in the  $\nu_{23}$  state interact with rovibrational energy levels from two other vibrational

states; one that originates at higher energy than  $\nu_{23}$  and the other that originates at lower energy than  $\nu_{23}$ . These perturbing states are discussed in Chapters 5 and 6, respectively.

## References

- (1) Kydd, R.A.; Wieser, H.; Kiefer, W. *Spectrochim. Acta.* **1983**, 39A, 173.
- (2) Pickett, H.M. *J. Mol. Spectrosc.* **1991**, 148, 371.
- (3) Watson, J.K.G. In *Vibrational Spectra and Structure*; Durig, J. Ed; Vol. VI; Elsevier: Amsterdam, 1977.
- (4) Moruzzi, G.; Kunzmann, M.; Winnewisser, B.; Winnewisser, M. *J. Mol. Spectrosc.* **2003**, 219, 152.
- (5) Loomis, F.W.; Wood, R.W. *Phys. Rev.* **1928**, 32, 223.

## Chapter 5 Coriolis interaction between the fundamental vibrations: C-O asymmetric stretch ( $\nu_{23}$ ) at $1008\text{ cm}^{-1}$ and the C-C symmetric stretch ( $\nu_6$ ) at $1033\text{ cm}^{-1}$

### 5.1 Introduction

Significant perturbations due to Coriolis interactions were encountered during the analysis of the C-O asymmetric stretch fundamental ( $\nu_{23}$ ) band at  $1008\text{ cm}^{-1}$ ; therefore, the rovibrational analysis of the next higher frequency vibration was necessary in order to account for these perturbations. Located at a higher frequency,  $1030\text{ cm}^{-1}$ , another band can be seen in the spectrum recorded at higher pressure (180 mTorr) shown in Fig (5.1). This band corresponds to the excitation of the symmetric stretch of C-C ( $\nu_6$ ). This normal mode was assigned by Kydd *et al.* at  $1033\text{ cm}^{-1}$ .<sup>1</sup> It can be seen also that the P-branch part of this spectrum is saturated and this is due to the overlap with very intense rovibrational transitions from the asymmetric stretch of C-O bands explained in the previous chapter.

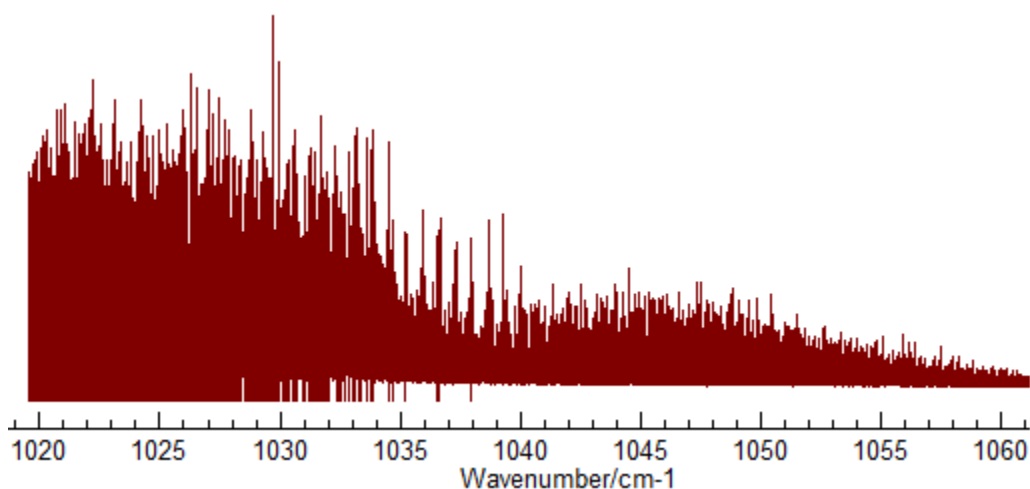


**Figure 5.1:** High resolution infrared spectrum of oxetane recorded at 180 mTorr which shows the  $\nu_6$  band that overlaps with the very intense bands in Fig (4.1), that cause the saturation in the P-branch region of  $\nu_6$ .

## 5.2 Preliminary analysis of the C-C symmetric stretch fundamental ( $\nu_6$ )

The saturation seen in Fig (5.1) along with the overall congestion of the spectrum make the rovibrational assignment in this region difficult. Despite these difficulties, this fundamental was rovibrationally analysed and found to obey *a-type* selection rules as this vibration involves a change in the dipole moment along the molecular a-axis which corresponds to  $A_1$  symmetry. Quantum mechanical calculations and symmetry based selection rules confirm the assignment of Kydd *et al.*, however, the rovibrational analysis in this study provides a more accurate band center.

Regardless of the complications in the spectrum of this band, the initial assignment of 236 transitions was performed and these were fit using Watson's A-reduced Hamiltonian in the  $I'$  representation<sup>2</sup> in Pickett's SPFIT program.<sup>3</sup> Preliminary rotational constants  $A$ ,  $B$  and  $C$  and the centrifugal distortion constants  $\Delta_J$  in the excited state were determined in the fit. The rest of the constants were fixed to the corresponding values in the ground vibrational state obtained by Moruzzi *et al.*<sup>4</sup> The preliminary spectroscopic parameters obtained in this fit are summarized in Table 5.1. More accurate spectroscopic constants for the  $\nu_6$  state will be presented at the end of this thesis following discussion of the perturbations involved.

**Table (5.1):** Spectroscopic constants (cm<sup>-1</sup>) for the ground state<sup>4</sup> and  $\nu_6$  state.

	Ground State <sup>4</sup>	$\nu_6$
$G_v$	0	1033.405167(51)
Rotational Constants		
$A$	0.40179332	0.400608(44)
$B$	0.391405984	0.390317(41)
$C$	0.224510678	0.22406440(26)
Quartic Centrifugal Distortion Constants ( $\times 10^8$ )		
$\Delta_J$	16.5254	16.095(22)
$\Delta_{JK}$	-4.68	-4.68
$\Delta_K$	15.23	15.23
$\delta_j$	5.4815	5.4815
$\delta_k$	-2.779	-2.779
Sextic Centrifugal Distortion Constants ( $\times 10^{12}$ )		
$\Phi_J$	0.627	0.627
$\Phi_{JK}$	0.8	0.8
$\Phi_{KJ}$	1.236	1.236
$\Phi_K$	-2.2	-2.2
$\varphi_j$	0.1	0.1
$\varphi_{jk}$	-0.897	-0.897
$\varphi_k$	-0.19	-0.19
rms error	0.000156	
No. transitions		236

Values in grey are fixed to values from reference<sup>4</sup>

### 5.2.1 Perturbations in the C-C symmetric stretch fundamental ( $\nu_6$ ) band

Inspection of progressions of rovibrational transitions in the  $\nu_6$  band using a Loomis-Wood (LW)<sup>5</sup> plot in Fig (5.2) shows that the  $\nu_6$  band has perturbations also. These perturbations start at a J value of 37 for the  $K_a=(0, 1)$  progression and at higher J for the higher  $K_a$  values. Moreover, the direct product of the vibrational state symmetries for the C-O asymmetric stretch and C-C symmetric stretch  $B_2 \otimes A_1 = B_2$  corresponds to a rotation about the molecular c-axis. Therefore, a *c-type* Coriolis interaction is possible between these two vibrational states. If the  $\nu_6$  mode is chosen as active, then the Coriolis

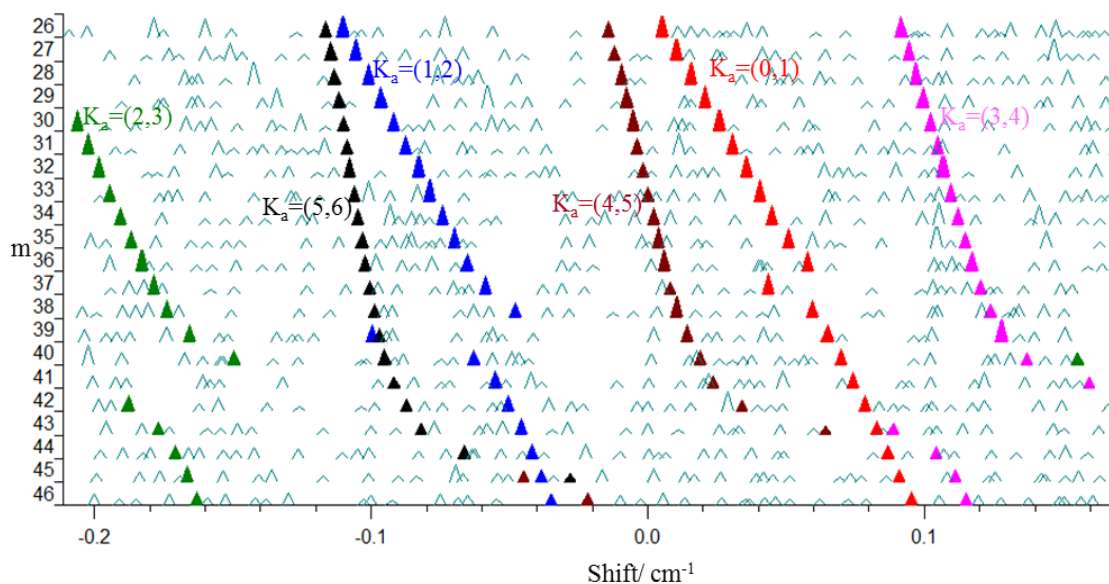


**Figure 5.2:** LW plot of the high resolution infrared spectrum of oxetane between 1047 and 1056 $\text{cm}^{-1}$  showing progressions of rovibrational transitions in the  $\nu_6$  fundamental.

forces action on the molecule can be described by dashed arrows in Fig (5.3). These forces can lead to the excitation of the  $\nu_{23}$  mode. All of these considerations makes the  $\nu_6$  state a potential candidate as a perturbing state for  $\nu_{23}$ .

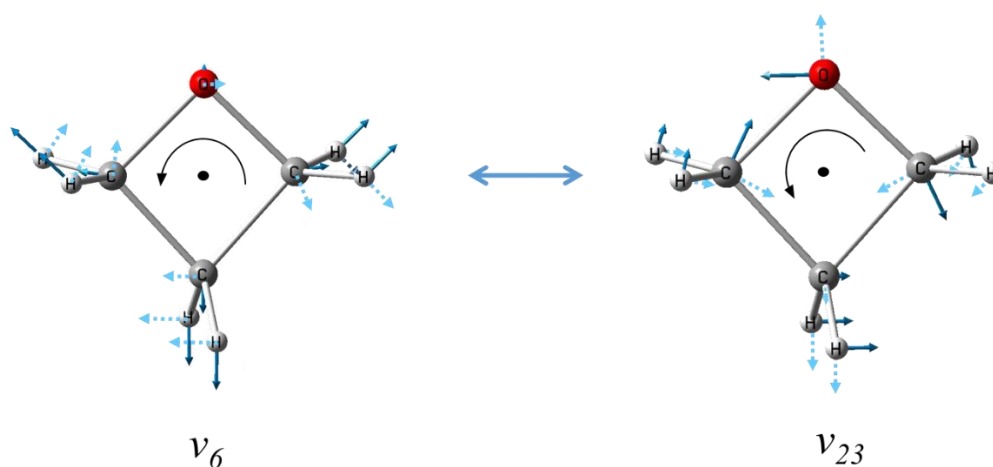


**Figure 5.3:** Coriolis forces acting on the two nondegenerate modes: symmetric C-C stretch ( $\nu_6$ ) and asymmetric C-O stretch ( $\nu_{23}$ ).

### **5.3 Analysis of the Coriolis interactions between the C-O asymmetric stretch fundamental ( $\nu_{23}$ ) and the C-C symmetric stretch ( $\nu_6$ )**

To simplify the treatment of the perturbations shown in Fig (4.4) and Fig (5.2), one must visualize the energies of the rovibrational levels of possible interacting vibrational states. The preliminary sets of spectroscopic parameters achieved earlier from the analysis of unperturbed rovibrational transitions in this work for the two states ( $\nu_{23}$  and  $\nu_6$ ) were used to plot the energies of the rovibrational levels. The following energy diagram in Fig (5.4) shows the reduced energies of the first few progressions of rovibrational levels that share a common  $K_a$  in a series belonging to each of the  $\nu_{23}$  and  $\nu_6$  vibrational states. For simplicity, only sets of  $K_a \leq 5$  and J quantum number values up to 60 are shown.

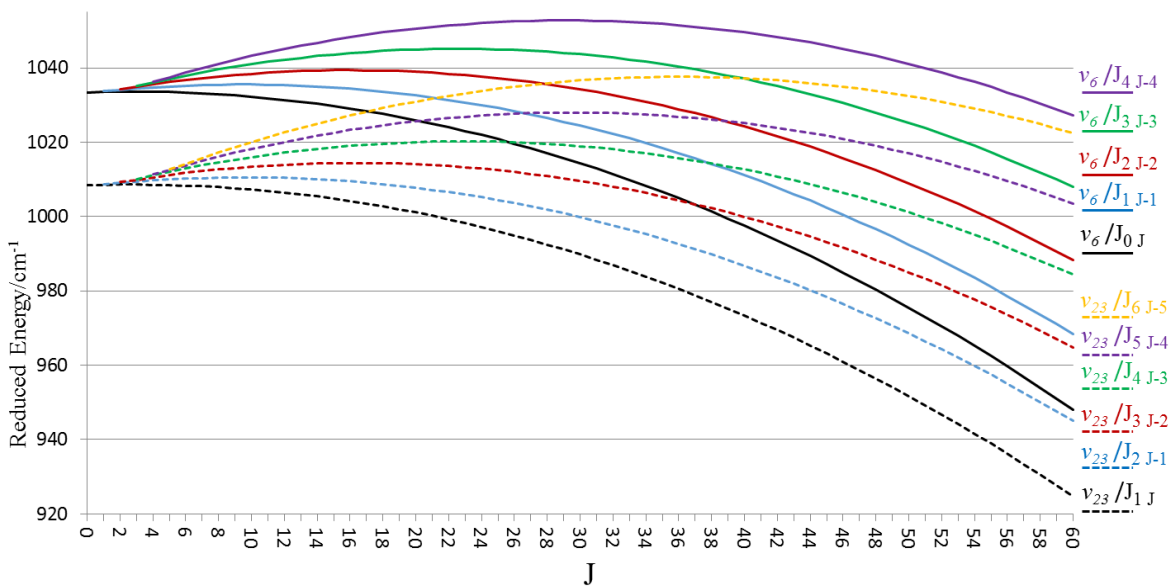


**Figure 5.4:** Reduced energies ( $\text{cm}^{-1}$ ) of levels with quantum number  $J \leq 60$  and  $K_a \leq 5$  of the states  $\nu_{23}$  at  $1008 \text{ cm}^{-1}$  and  $\nu_6$  at  $1033 \text{ cm}^{-1}$ .

Fig (5.4) shows that crossings between progressions of rovibrational energy levels in the  $\nu_{23}$  and  $\nu_6$  vibrational states are apparent. For instance, the lowest energy crossing can be seen between the progression labeled as  $\nu_{23}/J_3 J_{-2}$  in the  $\nu_{23}$  state in dashed red and the solid black curve labeled as  $\nu_6/J_0 J$  in the  $\nu_6$  state. They intersect at about quantum number  $J=37$ . The closest energy levels from these two progressions are  $37_3 35$  ( $J K_a K_c$ ) in the  $\nu_{23}$  state and  $37_0 37$  in the  $\nu_6$  state. These levels differ by  $\Delta K_a=3$  and have the correct symmetry for a second order *c-type* Coriolis interaction (parameter  $F_{ab}$ ).

Looking closely at the shifted transitions in the LW plots of Fig (5.2) and Fig (4.4) in comparison with the energy level diagram seen in Fig (5.4), shows that the quantum numbers of these transitions in the excited state correspond to the same quantum numbers of the energy levels at the crossing sites in the energy diagram. For example in the  $\nu_6$

band in Fig (5.2), the strongest shift from the linear trend with  $K_a = (0, 1)$  is at  $J=37$  which corresponds to the level  $37_0\ 37$ , which can interact with the  $37_3\ 35$  level seen in the progression  $K_a = (2, 3)$  of the  $\nu_{23}$  band in Fig (4.4). The visual evidence of the perturbed transitions with higher  $K_a$  values in the LW plots also agree with crossings in the energy level diagram shown in Fig (5.4). It should be noted that the energy levels correspond to crossings at lower  $J$  values in Fig (5.4) do not have the right symmetry to interact via Coriolis interactions which is confirmed by the fact that transitions involving these energy levels are not perturbed.

When the Coriolis coupling constant  $F_{ab}$  was included in the model Hamiltonian in a simultaneous fit of these two bands, it allowed the assignment of the perturbed rovibrational transitions in the  $\nu_6$  band and the corresponding perturbed transitions in the  $\nu_{23}$  band which were originally excluded. A total of 1162 transitions in the  $\nu_6$  band with values of the quantum number  $J$  between 8 and 55 and a maximum of  $K_a$  values of 25 were then fit. The  $\nu_6$  band is of low infrared intensity compared to the neighbouring subset of bands of the C-O asymmetric stretch ( $\nu_{23}$ ) and the P-branch of the  $\nu_6$  band overlaps with R-branches of this intense subset of bands. These factors make the assignment of rovibrational transitions in the P-branch of  $\nu_6$  impossible except for 36 rovibrational transitions because of the saturation of this part of spectrum. The inclusion of the Coriolis term in the model Hamiltonian allowed the assignment of 926 additional transitions in the  $\nu_6$  band and 296 additional transitions in the  $\nu_{23}$  band. The simultaneous fit of 2474 transitions allowed the determination of the Coriolis coupling constant  $F_{ab}(\nu_{23}, \nu_6)$  and provided refined spectroscopic parameters for each of these fundamentals. These parameters are summarized in Table 5.2.

**Table (5.2):** Spectroscopic constants ( $\text{cm}^{-1}$ ) for the ground state,  $^4 v_6$  and  $v_{23}$  states following treatment of the Coriolis interaction.

	Ground State <sup>4</sup>	$v_6$	$v_{23}$
$G_v$	0	1033.405418(61)	1008.364346(60)
Rotational Constants			
$A$	0.40179332	0.4006276(24)	0.4004090(47)
$B$	0.391405984	0.3902948(20)	0.3900466(42)
$C$	0.224510678	0.22406364(10)	0.22458181(16)
Quartic Centrifugal Distortion Constants ( $\times 10^8$ )			
$\Delta_J$	16.5254	16.0956(32)	17.1534(75)
$\Delta_{JK}$	-4.68	-2.590(27)	-2.179(63)
$\Delta_K$	15.23	13.024(60)	6.24(13)
$\delta_j$	5.4815	5.4815	5.4815
$\delta_k$	-2.779	-2.779	-2.779
Sextic Centrifugal Distortion Constants ( $\times 10^{12}$ )			
$\Phi_J$	0.627	0.627	0.627
$\Phi_{JK}$	0.8	0.8	0.8
$\Phi_{KJ}$	1.236	1.236	1.236
$\Phi_K$	-2.2	-2.2	-2.2
$\varphi_j$	0.1	0.1	0.1
$\varphi_{jk}$	-0.897	-0.897	-0.897
$\varphi_k$	-0.19	-0.19	-0.19
$F_{ab}(v_{23}, v_6)/\text{cm}^{-1}$			$-9.6281(64) \times 10^{-4}$
rms error		0.000440	
No. transitions		1162	1312

Values in grey are fixed to values from reference<sup>4</sup>

Up to this point, one set perturbations in the  $v_{23}$  band that start at  $J=37$  in the  $K_a=(2, 3)$  series and extends to higher  $J$  and  $K_a$  values as shown clearly in the LW plot Fig (4.4) has been successfully described in this fit. However, a second set of perturbations can also be seen in this LW plot. This set starts at the  $J=28$  in  $K_a=(0,1)$  series and extends to higher  $J$  and  $K_a$  values. Therefore, another state must be involved and according to the reduced energy diagram in Fig (5.4), progressions from this state have to cross the dashed black line labeled  $v_{23} / J_1 J$  in order for the lower  $J$  levels to be perturbed. This state

therefore must originate at lower energy than the  $\nu_{23}$  fundamental at  $1008\text{ cm}^{-1}$ . The origin of the second set of perturbations will be discussed in Chapter 6.

#### 5.4. Summary

Analysis of the C-O asymmetric stretch fundamental  $\nu_{23}$  at  $1008\text{ cm}^{-1}$  showed that many of its rovibrational energy levels interact with rovibrational energy levels from two other vibrational states; one that originates at an energy above the  $\nu_{23}$  state and the other that originates at a lower energy. The rovibrational analysis of the C-C symmetric stretch fundamental ( $\nu_6$ ) suggested that it is the potential perturbing band that is higher in energy than the C-O asymmetric stretch. Investigation of the rovibrational levels energies along with the symmetry selection rules for Coriolis interactions showed that the  $\nu_{23}$  and  $\nu_6$  states interact via a second order *c-type* Coriolis interaction and its treatment allowed the assignment of 1312 transitions for the  $\nu_{23}$  band and 1162 transitions for the  $\nu_6$  band. The latter has a very low infrared intensity compared to the overlapping intense, very congested subset of bands at lower frequency. These difficulties made most of the P-branch of the  $\nu_6$  band impossible to assign. Some candidates for lower vibrational states that perturb the C-O asymmetric stretch fundamental ( $\nu_{23}$ ) at  $1008\text{ cm}^{-1}$  are discussed in the next chapter. This requires analysis of bands below  $1000\text{ cm}^{-1}$  in order to account for perturbations in the  $\nu_{23}$  fundamental.

## References

- (1) Kydd, R.A.; Wieser, H.; Kiefer, W. *Spectrochim. Acta.* **1983**, 39A, 173.
- (2) Watson, J.K.G. In *Vibrational Spectra and Structure*; Durig, J. Ed; Vol. VI; Elsevier: Amsterdam, 1977.
- (3) Pickett, H.M. *J. Mol. Spectrosc.* **1991**, 148, 371.
- (4) Moruzzi, G.; Kunzmann, M.; Winnewisser, B.; Winnewisser, M. *J. Mol. Spectrosc.* **2003**, 219, 152.
- (5) Loomis, F.W.; Wood, R.W. *Phys. Rev.* **1928**, 32, 223.

## **Chapter 6: Global analysis of perturbations in the C-O asymmetric stretch ( $\nu_{23}$ ), C-C symmetric stretch ( $\nu_6$ ) and the C-C asymmetric stretch hot band ( $\nu_{18}+\nu_{24} - \nu_{18}$ )**

### **6.1 Introduction**

As mentioned earlier, perturbations in the C-O asymmetric stretch fundamental ( $\nu_{23}$ ) at  $1008\text{ cm}^{-1}$  are caused by Coriolis interactions of the  $\nu_{23}$  state by two other states. Interaction with the higher energy  $\nu_6$  state was discussed in the previous chapter. In order to analyze Coriolis interactions caused by a lower energy state, it is necessary to identify the states that are close in energy and have the right symmetry to cause such interactions. Given that ring puckering couples to other vibrations as discussed earlier in Chapter 3 and 4 of this work, this introduces more candidates to be involved in the Coriolis interactions with the  $\nu_{23}$  state. Therefore, rovibrational analysis of bands with band centers that lie between  $900\text{ cm}^{-1}$  and  $1000\text{ cm}^{-1}$  were performed.

### **6.2 Candidates for the lower perturbing state**

#### **6.2.1 The C-C asymmetric stretch fundamental ( $\nu_{24}$ ) and the hot band ( $\nu_{18}+\nu_{24} - \nu_{18}$ )**

According to the quantum mechanical calculations, the next lower frequency fundamental belongs to the C-C asymmetric stretch ( $\nu_{24}$ ). The harmonic frequency calculations following geometry optimization using the MP2 method/ 6-31++G (2d, 2p) basis set predicts this fundamental vibration to be at  $956\text{ cm}^{-1}$  while it is predicted by applying anharmonic corrections to appear at  $940\text{ cm}^{-1}$ . This band has very low infrared intensity and overlaps with the intense C-O symmetric stretch ( $\nu_7$ ) at  $908\text{ cm}^{-1}$  and the subset of C-O asymmetric stretch bands ( $\nu_{23}$ ) at  $1008\text{ cm}^{-1}$  as shown in Fig (6.1).

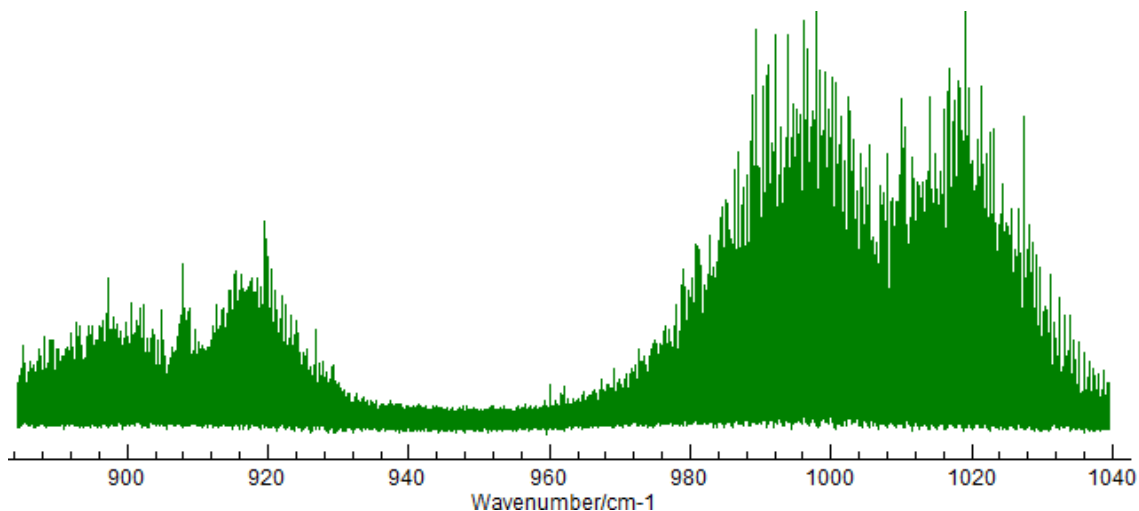


**Figure 6.1:** High resolution infrared spectrum of oxetane recorded at 5 mTorr which shows the  $\nu_7$  band and the subset of bands related to the  $\nu_{23}$  mode.

As a result of the spectral congestion and low infrared intensity, no clue from the spectrum indicates the band center of  $\nu_{24}$ . This vibration has  $B_2$  symmetry and thus, the direct product of the  $\nu_{23}$  and  $\nu_{24}$  vibrational symmetries  $B_2 \otimes B_2 = A_1$  does not correspond to the symmetry of rotation about any of the molecular axes under  $C_{2v}$ . Therefore, no direct Coriolis interaction is allowed between these two states.

When the C-C asymmetric stretch mode couples to the ring puckering mode, the hot combination band  $\nu_{18+\nu_{24}} - \nu_{18}$  becomes a potential candidate as a perturbing band. The direct product of the  $\nu_{18+\nu_{24}}$  and  $\nu_{23}$  vibrational state symmetries  $A_2 \otimes B_2 = B_1$  permits *b-type* Coriolis interactions between these two states. Due to the lack of a visible band center in Fig (6.1), this hot band also is not eligible for rovibrational assignment. Therefore, other possible candidates were investigated.

### 6.2.2 The C-O symmetric stretch fundamental ( $\nu_7$ ) and the hot band ( $\nu_7+\nu_{18} - \nu_{18}$ )

Lower than the bands discussed in 6.2.1, the fundamental of the symmetric stretch of C-O ( $\nu_7$ ) is centered at  $908\text{ cm}^{-1}$  in Fig (6.1). Rovibrational analysis of this fundamental band was performed in this study and it was found that the origin of this band is located at  $908\text{ cm}^{-1}$ , slightly lower than the vibrational assignment by Kydd *et al.* at  $909\text{ cm}^{-1}$ .<sup>1</sup> The rovibrational transitions of this fundamental band follow *a-type* selection rules as a consequence of the symmetry of this normal mode which is totally symmetric. A total of 1584 rovibrational transitions in progressions of J from 5 through 43 and  $K_a$  values up to 28 were assigned and fitted using Watson's A-reduced Hamiltonian in the  $I'$  representation<sup>2</sup> in Pickett's SPFIT program.<sup>3</sup> The rms error of the fit was  $0.000200\text{ cm}^{-1}$ . These parameters are summarized in Table 6.1.

As *c-type* Coriolis interactions are allowed by symmetry between the  $\nu_7$  and  $\nu_{23}$  states, the preliminary spectroscopic constants of the  $\nu_7$  state were used to build a reduced energy diagram shown in Fig(6.2) including rovibrational levels in the  $\nu_7$  and the  $\nu_{23}$  states. Upon inspection, crossing in rovibrational level of these states were not found at the local perturbation sites of the C-O asymmetric stretch fundamental ( $\nu_{23}$ ) identified in Fig (4.4) as the  $\nu_7$  band is too low in energy.

Inspection of the spectrum in Fig (3.8) showed another band with closely spaced Q-branch transitions at  $864\text{ cm}^{-1}$  which does not correspond to a fundamental vibration. When patterns of transitions in this band were inspected with the aid of a LW plot, they were found to obey *a-type* selection rules. Furthermore, the GSCDs of progressions in the P-branch and R-branch of this band were investigated and found to correspond to the first

**Table (6.1):** Spectroscopic constants ( $\text{cm}^{-1}$ ) for the ground <sup>4</sup> and  $\nu_7$  states.

	Ground State <sup>4</sup>	$\nu_7$
$G_v$	0	908.427247(33)
Rotational Constants		
$A$	0.40179332	0.4008022(83)
$B$	0.391405984	0.3906555(74)
$C$	0.224510678	0.22041061(28)
Quartic Centrifugal Distortion Constants ( $\times 10^7$ )		
$\Delta_J$	1.65254	2.202(71)
$\Delta_{JK}$	-0.468	-20.5(10)
$\Delta_K$	1.523	29.3(15)
$\delta_j$	0.54815	3.156(37)
$\delta_k$	-0.2779	-13.31(44)
Sextic Centrifugal Distortion Constants ( $\times 10^{11}$ )		
$\Phi_J$	0.627	3.107(81)
$\Phi_{JK}$	0.8	0.8
$\Phi_{KJ}$	1.236	-5.36(68)
$\Phi_K$	-2.2	-19.29(39)
$\varphi_j$	0.1	3.835(55)
$\varphi_{jk}$	-0.897	-0.897
$\varphi_k$	-0.19	-0.19
rms error	0.000200	
No. transitions		1584

Values in grey are fixed to values from reference <sup>4</sup>

ring puckering vibrational state ( $\nu_{18}$ ) which has  $B_1$  symmetry. The dipole moment component along the molecular a-axis is totally symmetric and therefore, the higher vibrational state must be of  $B_1$  symmetry. This is consistent with a combination between the C-O symmetric stretch ( $\nu_7$ ) and ring puckering ( $\nu_{18}$ ).

Up to this point, 420 transitions were assigned to this hot band. The assigned transitions with  $K_a = (0,1)$  have quantum number J values spanning from 5 to 43. On the other hand, progressions that have higher  $K_a$  values do not have quantum number J values that exceed 29 due to perturbations in the higher states. Seven parameters for the state

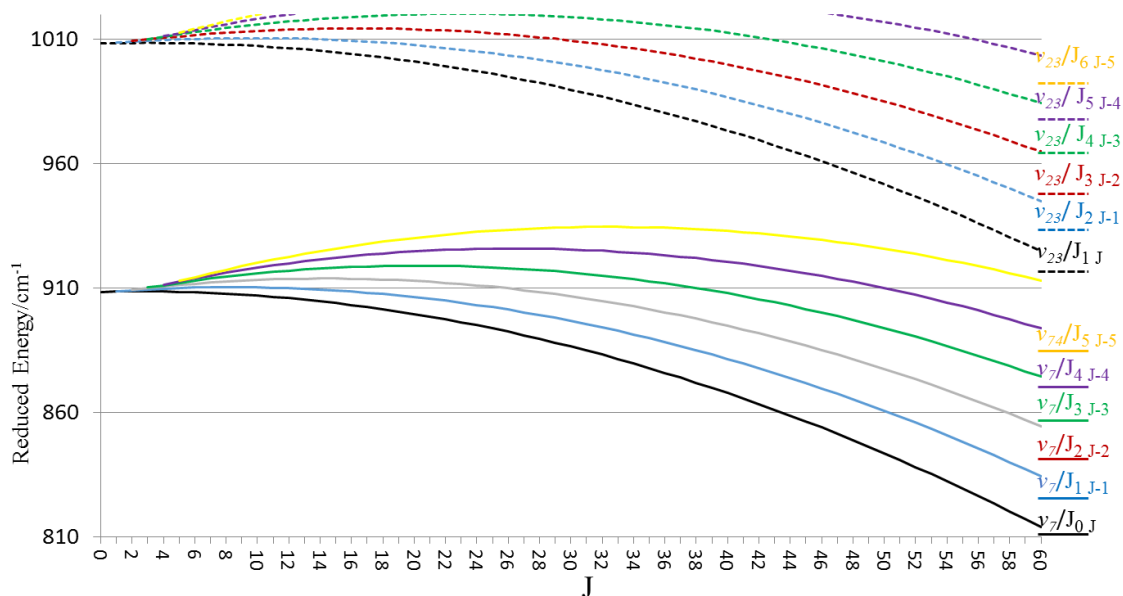


**Figure 6.2:** Reduced energies ( $\text{cm}^{-1}$ ) of levels with quantum number  $J \leq 60$  and  $K_a \leq 60$  of the states  $\nu_7$  at  $908 \text{ cm}^{-1}$   $\nu_{23}$  at  $1008 \text{ cm}^{-1}$ .

$\nu_7 + \nu_{18}$  were determined by fitting the assigned transitions while the rest of the parameters were fixed to values obtained by Moruzzi *et al.*<sup>4</sup> The lower state of this band corresponds to the first excited vibrational state of ring puckering and the rms error value of this fit was  $0.000134 \text{ cm}^{-1}$ . Table (6.2) reports the spectroscopic parameters obtained for this band. By symmetry, *a-type* Coriolis interactions are permitted between the  $\nu_7 + \nu_{18}$  and  $\nu_{23}$  states, however, the hot band  $\nu_7 + \nu_{18} - \nu_{18}$  was excluded for the same reason as the  $\nu_7$  fundamental.

**Table (6.2):** Spectroscopic constants ( $\text{cm}^{-1}$ ) for the  $\nu_7+\nu_{18}$  and  $\nu_{18}^4$  states.

	$\nu_{18}^4$	$\nu_7+\nu_{18}$
$G_v$	52.920348	916.859741(30)
Rotational Constants		
$A$	0.402209858	0.402156(20)
$B$	0.391155554	0.390725(18)
$C$	0.22589666	0.224940589(99)
Quartic Centrifugal Distortion Constants ( $\times 10^8$ )		
$\Delta_J$	16.6282	14.1601(49)
$\Delta_{JK}$	-21.5803	-28.86(41)
$\Delta_K$	32.248	52.39(91)
$\delta_j$	5.3811	5.3811
$\delta_k$	5.9528	5.9528
Sextic Centrifugal Distortion Constants ( $\times 10^{12}$ )		
$\Phi_J$	0.537	0.537
$\Phi_{JK}$	-1.79	-1.79
$\Phi_{KJ}$	1.93	1.93
$\Phi_K$	-0.397	-0.397
$\varphi_j$	0.097	0.097
$\varphi_{jk}$	0.54	0.54
$\varphi_k$	0.871	0.871
rms error		0.000134
No. transitions		480

Values in grey are fixed to values from reference <sup>4</sup>

### 6.3 Analysis of the Coriolis interactions between the C-O asymmetric stretch fundamental ( $\nu_{23}$ ) and the C-C asymmetric stretch hot band ( $\nu_{18}+\nu_{24} - \nu_{18}$ )

In order to account for perturbations seen in the progressions of rovibrational transitions in the  $\nu_{23}$  band that have  $K_a$  values of (0,1) and (1,2) in Fig (4.4), diagrams of vibrational states that have lower energy than  $\nu_{23}$  were inspected as described above. The most probable candidate following this was determined to be  $\nu_{18}+\nu_{24}$ . This vibrational state has  $A_2$  symmetry; the direct product  $A_2 \otimes B_2 = B_1$  corresponds to a rotation about

*b*-inertial axis of oxetane. Therefore,  $\nu_{23}$  and  $\nu_{18+\nu_{24}}$  could interact via *b*-type Coriolis forces.

Unfortunately, as discussed above, no experimental spectroscopic parameters could be determined for the  $\nu_{18+\nu_{24}} - \nu_{18}$  band nor for the  $\nu_{24}$  band due to the very low infrared intensity compared to its neighbouring bands ( $\nu_7$  at  $908\text{ cm}^{-1}$  and the subset of bands  $\nu_{23}$ ,  $\nu_{18+\nu_{23}} - \nu_{18}$  and  $2\nu_{18+\nu_{23}} - 2\nu_{18}$ ). Without direct spectroscopic information about this state, an approximation was needed. Therefore, the rotational and centrifugal distortion constants from the  $\nu_{18+\nu_{23}}$  state (another combination state of similar energy) (Chapter 4) were used to predict the rotational spacing of the energy levels in the  $\nu_{18+\nu_{24}}$  state. The hot combination band ( $\nu_{18+\nu_{24}} - \nu_{18}$ ) involves the asymmetric stretch of C-C and is somewhat analogous to the asymmetric stretch of C-O ( $\nu_{24}$ ) therefore, the spectroscopic parameters of the  $\nu_{18+\nu_{23}}$  vibrational state are expected to be most similar to the spectroscopic parameters from the  $\nu_{18+\nu_{24}}$  state. With the band center approximated as  $997\text{ cm}^{-1}$ , the rovibrational energies along with those in the  $\nu_{23}$  state were combined to build the reduced energy diagram in Fig (6.3).

As the band center ( $G_v$ ) of  $\nu_{18+\nu_{24}}$  is not known, various values were tested to see which would provide crossing of the correct progressions in Fig (6.3). For a value of  $997\text{ cm}^{-1}$ , crossings between  $\nu_{23}$  and  $\nu_{18+\nu_{24}}$  in the energy diagram were found to explain perturbations seen in the  $\nu_{23}$  band in Fig (4.4). For example, this diagram shows that the progression of rovibrational states that is labeled with  $\nu_{23}/J_1$ , the dashed black curve from the  $\nu_{23}$  state, intersects with the progression of rovibrational levels labeled  $\nu_{18+\nu_{24}}/J_2$ , the solid blue curve from the  $\nu_{18+\nu_{24}}$  state, at about quantum number  $J=30$  which show that the rovibrational energy levels  $30_1$  in the  $\nu_{23}$  state and  $30_2$  in the  $\nu_{18+\nu_{24}}$  state are

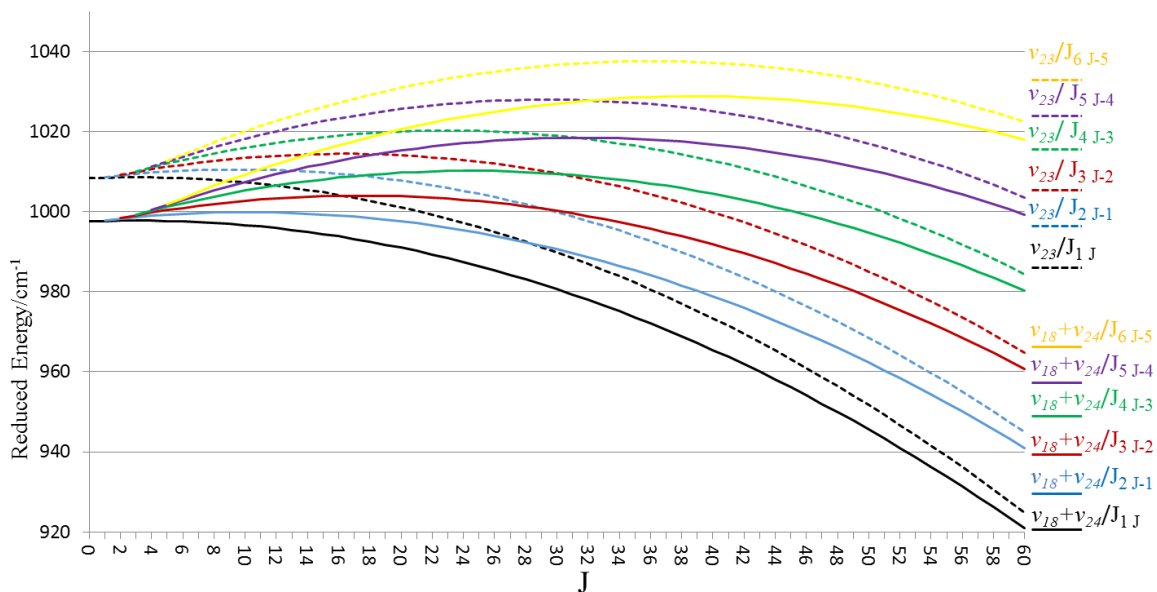


**Figure 6.3:** Reduced energies ( $\text{cm}^{-1}$ ) of levels with quantum number  $J \leq 60$  and  $K_a \leq 60$  of the states  $\nu_{18}+\nu_{24}$  at  $997 \text{ cm}^{-1}$   $\nu_{23}$  at  $1008 \text{ cm}^{-1}$ .

close in energy. In addition, these energy levels differ by  $\Delta K_a=1$  which corresponds to a first order *b-type* Coriolis interaction. In a similar fashion, the other perturbations in Fig (4.4) can be explained also.

## 6.4 Global analysis

When the first order Coriolis coupling constant  $G_b$  was included in the model Hamiltonian in a simultaneous fit of the three bands  $\nu_{23}$ ,  $\nu_6$  and  $\nu_{18}+\nu_{24} - 2\nu_{18}$ , it allowed the assignment of more than a thousand additional rovibrational transitions in the  $\nu_{23}$  band affected by Coriolis interactions between the  $\nu_{23}$  and  $\nu_{18}+\nu_{24}$  states shown in Fig (4.4). A total of 2328 rovibrational transitions in the  $\nu_{23}$  band with values of the quantum number  $J$  extending from 4 through 51 and values  $K_a$  up to 28 were then fit.

Table 6.3 reports the spectroscopic parameters obtained for a global fit of the three bands ( $\nu_{23}$ ,  $\nu_6$ ,  $\nu_{18+\nu_{24}} - 2\nu_{18}$ ) to a total of 3452 transitions using Watson's A-reduced Hamiltonian in the  $I'$  representation<sup>2</sup> in Pickett's SPFIT program.<sup>3</sup> Only the band origin of  $\nu_{18+\nu_{24}} - 2\nu_{18}$  and the Coriolis coupling constant  $G_b$  between the  $\nu_{23}$  and  $\nu_{18+\nu_{24}}$  vibrational states could be determined for the lower state as no rovibrational transitions could be assigned for this hot combination band. The rms error value of this global fit was  $0.000221 \text{ cm}^{-1}$ . Fig (6.4) shows a segment of the high resolution infrared spectrum of oxetane in which some perturbed rovibrational transitions in the  $\nu_{23}$  band (and its related hot combination bands) are presented. This part of the spectrum is compared to a simulation using PGOPHER<sup>6</sup> without the inclusion of Coriolis interaction terms to the model Hamiltonian. In this region, it can be seen that the rovibrational transitions are shifted from their predicted positions.

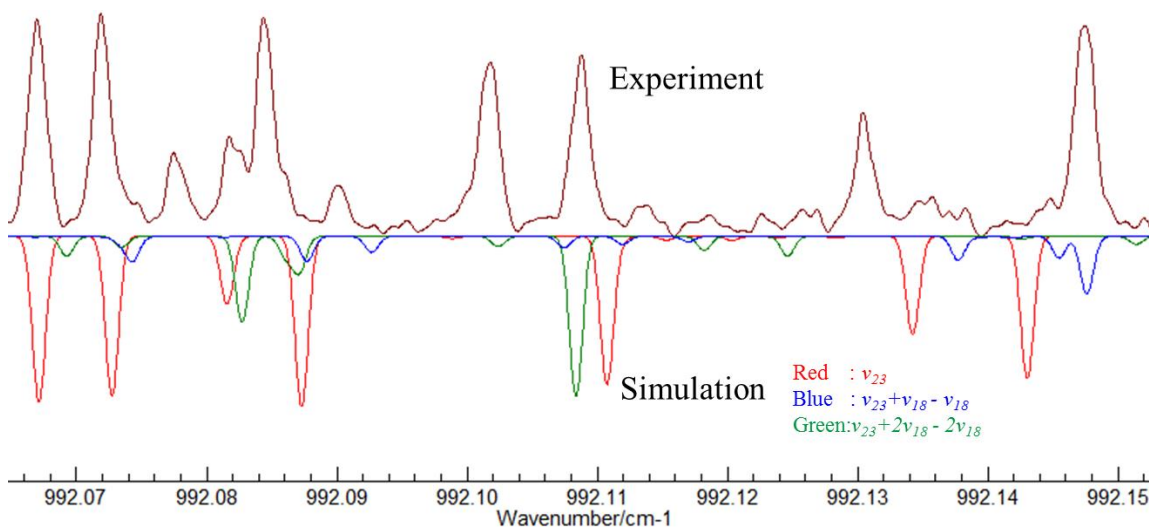


**Figure 6.4:** A comparison between the simulated and the observed spectrum of the  $\nu_{23}$  band without including the Coriolis interactions terms in the model Hamiltonian used.

**Table (6.3):** Spectroscopic constants ( $\text{cm}^{-1}$ ) for the G.S.,  $\nu_{18}$ ,  $\nu_{18}+\nu_{24}$ ,  $\nu_{23}$ , and  $\nu_6$  of oxetane.

	G.S. <sup>(6)</sup>	$\nu_{18}$ <sup>(6)</sup>	$\nu_{18}+\nu_{24}$	$\nu_{23}$	$\nu_6$
$G_\nu$	0	52.920348	997.54543(68)	1008.364520(19)	1033.405418(28)
<b>Rotational Constants</b>					
$A$	0.40179332	0.402209858	0.4022555	0.40033830(72)	0.4006200(11)
$B$	0.391405984	0.391155554	0.3897205	0.39010458(60)	0.3903015(10)
$C$	0.224510678	0.22589666	0.22620929	0.224581154(50)	0.224064344(58)
<b>Quartic Centrifugal Distortion Constants (<math>\times 10^8</math>)</b>					
$A_J$	16.5254	16.6282	18.261	17.1122(23)	16.1298(23)
$A_{JK}$	-4.68	-21.5803	-32.39	-2.894(16)	-2.757(16)
$A_K$	15.23	32.248	91.42	8.032(29)	13.240(30)
$\delta_j$	5.4815	5.3811	5.3811	5.4815	5.4815
$\delta_k$	-2.779	5.9528	5.9528	-2.779	-2.779
<b>Sextic Centrifugal Distortion Constants (<math>\times 10^{12}</math>)</b>					
$\Phi_J$	0.627	0.537	0.537	0.627	0.627
$\Phi_{JK}$	0.800	-1.79	-1.79	0.800	0.800
$\Phi_{KJ}$	1.236	1.93	1.93	1.236	1.236
$\Phi_K$	-2.2	-0.397	-0.397	-2.2	-2.2
$\varphi_j$	0.10	0.097	0.097	0.10	0.10
$\varphi_{jk}$	-0.897	0.54	0.54	-0.897	-0.897
$\varphi_k$	-0.19	0.871	0.871	-0.19	-0.19
$G_b(\nu_{18}+\nu_{24}, \nu_{23})/\text{cm}^{-1}$			-6.5115(93) $\times 10^{-3}$		
$F_{ab}(\nu_{23}, \nu_6)/\text{cm}^{-1}$				-9.6593(15) $\times 10^{-4}$	
rms error			0.000221		
No. transitions			2328		1124

Values in grey are fixed to values from reference <sup>4</sup>

Fig (6.5) shows the same segment of the spectrum as in Fig (6.4), however, the simulation was produced with the inclusion of the Coriolis interaction terms in the model Hamiltonian and assignment of many perturbed rovibrational transitions that followed the treatment of the perturbations. It can be seen in the following figure that the simulation of the  $\nu_{23}$  band accounts for the perturbed rovibrational transitions. This means that the inclusion of the Coriolis interaction parameters allows precise calculation of the rovibrational levels energies in the  $\nu_{23}$  vibrational state. As a result, it allowed the assignments of hundreds of perturbed transitions in the in the  $\nu_{23}$  and  $\nu_6$  states.

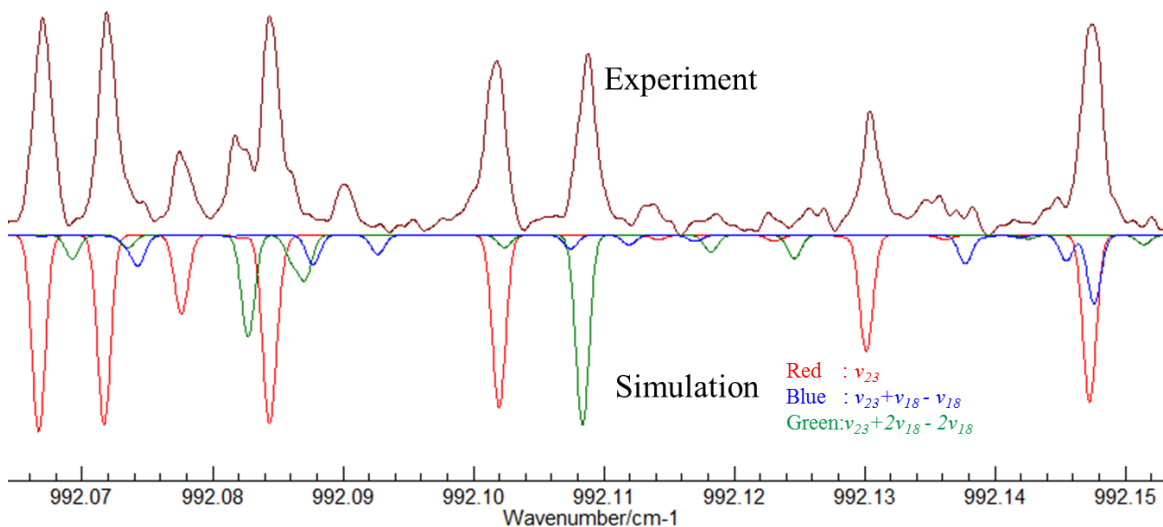


**Figure 6.5:** A comparison between the simulated and the observed spectrum of the  $\nu_{23}$  band after including the Coriolis interactions terms in the model Hamiltonian used.

## 6.5 Summary

Since the analysis of the C-O asymmetric stretch  $\nu_{23}$  fundamental at  $1008\text{ cm}^{-1}$  in chapters 4 and 5 showed that many of the rovibrational energy levels in the  $\nu_{23}$  state interact with levels from two other vibrational states, one higher and one lower in energy, the source of these perturbations was analyzed. Rovibrational analysis of the C-C symmetric stretch fundamental ( $\nu_6$ ) in Chapter 5 was found to be the higher perturbing state via a second order *c-type* Coriolis interaction. The investigation of possible states as candidates for the lower perturbing state, as described in this chapter, was then performed and it was found that the state coupled between the ring puckering and the C-C asymmetric stretch modes ( $\nu_{18}+\nu_{24}$ ) was a plausible candidate. These states were found to interact via first order *b-type* Coriolis forces. When the coupling constant  $G_b$  was included in the model Hamiltonian in a simultaneous fit of the three bands ( $\nu_{23}$ ,  $\nu_6$  and  $\nu_{18}+\nu_{24} - 2\nu_{18}$ ) it allowed the assignment of more than a thousand perturbed rovibrational transitions in the  $\nu_{23}$  state that are caused by Coriolis interactions between  $\nu_{23}$  and  $\nu_{18}+\nu_{24}$ .

## References

- (1) Kydd, R.A.; Wieser, H.; Kiefer, W. *Spectrochim. Acta.* **1983**, 39A, 173.
- (2) Watson, J.K.G. In *Vibrational Spectra and Structure*; Durig, J. Ed; Vol. VI; Elsevier: Amsterdam, 1977.
- (3) Pickett, H.M. *J. Mol. Spectrosc.* **1991**, 148, 371.
- (4) Moruzzi, G.; Kunzmann, M.; Winnewisser, B.; Winnewisser, M. *J. Mol. Spectrosc.* **2003**, 219, 152.
- (5) Loomis, F.W.; Wood, R.W. *Phys. Rev.* **1928**, 32, 223.
- (6) Western, C.M. *J. Quant. Spectrosc. Ra.* **2016**, 186, 221.

## Chapter 7: Summary and future work

In this work, the high resolution infrared spectrum of oxetane between 400 and 1180  $\text{cm}^{-1}$  was recorded at the Canadian Light Source (CLS) using synchrotron radiation as the light source. No high resolution infrared study was attempted for oxetane before this work except for the ring puckering mode which was subjected to spectroscopic studies over decades due to the complexity of this vibration.<sup>1-14</sup> The rovibrational analysis performed in this study showed that the ring puckering motion has a tremendous effect on the spectrum under study through congestion (high density of transitions) and perturbations caused by many states close in energy. Due to ring puckering, many more vibrational transitions appear in addition to what was suggested in the quantum mechanical calculations performed in this work and in the previous low resolution infrared studies.<sup>10</sup> The vibrational energy levels of ring puckering in oxetane are closely spaced<sup>3,8,13-15</sup> which allows a noteworthy distribution of oxetane molecules among the first few vibrational states of this normal mode at room temperature. This distribution results in many hot bands that initiate in excited vibrational states of ring puckering. Coupling of the ring puckering with other normal modes results in hot and combination bands to appear in the spectrum under study. At the same time, this coupling introduces additional vibrational states that oxetane can occupy and these states are packed within a short window which increases the probability of perturbations to occur.

Through the analysis of the high resolution infrared spectrum of oxetane, rotational structure of the vibrational bands was revealed which provided information that cannot be achieved using low resolution infrared techniques for the vibrational assignment. Overlapping or even superimposed rovibrational bands were analysed in the high

resolution spectra with precise determination of their band centers. Moreover, rovibrational analysis in this work allowed unambiguous assignment of the underlying normal modes due to the fact that large numbers of rovibrational transitions initiate in rotational levels above the ground vibrational state that can be described precisely using spectroscopic constants from previous microwave studies. Furthermore, rovibrational transitions obey quantum mechanical selection rules which provide information about the symmetry of the vibration confirming the vibrational assignment.

Rovibrational analysis in this study allowed the vibrational assignment of many more bands compared to literature<sup>10,16</sup> which include hot and combination bands and re-assignment of fundamentals that were previously incorrectly determined. The ring deformation fundamental mode, for example, is now correctly assigned at  $839\text{ cm}^{-1}$  rather than  $785\text{ cm}^{-1}$ <sup>10</sup>. The vibrational assignment of other fundamental bands in the literature was confirmed in this study; however, more accurate band origins are provided here. Several hot and combination bands were assigned in this work through rovibrational analysis : the hot bands of the C-O asymmetric stretch  $\nu_{18}+\nu_{23} - \nu_{18}$  at  $1002\text{ cm}^{-1}$  and  $2\nu_{18}+\nu_{23} - 2\nu_{18}$  at  $999\text{ cm}^{-1}$ , the C-C asymmetric stretch hot band  $\nu_{18}+\nu_{24} - \nu_{18}$  at  $944\text{ cm}^{-1}$ , the C-O symmetric stretch hot band  $\nu_7+\nu_{18} - \nu_{18}$  at  $864\text{ cm}^{-1}$  and the combination bands between the ring puckering and the  $\beta$ -CH<sub>2</sub>-rocking normal modes  $\nu_{17}+\nu_{18}$  at  $754\text{ cm}^{-1}$ ,  $\nu_{17}+2\nu_{18} - \nu_{18}$  at  $784\text{ cm}^{-1}$ ,  $\nu_{17}+3\nu_{18} - 2\nu_{18}$  at  $785\text{ cm}^{-1}$  and  $\nu_{17}+4\nu_{18} - 3\nu_{18}$  at  $786\text{ cm}^{-1}$ .

Frequency calculations using MP2 and DFT methods were performed and compared to the experimental results obtained from this work. The anharmonic frequency calculations using the MP2 method showed better agreement with the experiment, however, the calculated frequencies using this method predicts the ring puckering

fundamental to be 65% higher than the experimental value.<sup>3,8,13-15</sup> None of the methods used for frequency calculations systematically reproduces the experimental results. The spectroscopic constants including the rotational and centrifugal distortion constants for many vibrational states in addition to the precisely determined band centers allowed the unambiguous assignment of vibrations and revealed that many bands arise due to coupling of the ring puckering with other modes. All this information can be used as benchmark data by theoreticians to develop methods that better describe molecules with such low frequency vibrations arising from such a complex underlying potential.

In addition, the congestion seen in the spectrum and the perturbations which extend over large number of transitions made the analysis challenging. These perturbations are caused by Coriolis interactions which occur between rovibrational energy levels that are close. Analysis of perturbations in the C-O asymmetric fundamental  $\nu_{23}$  at  $1008\text{ cm}^{-1}$  showed that rovibrational energy levels in the  $\nu_{23}$  state interact with rovibrational energy levels from two other vibrational states, one that originates at higher and the other at lower energy than the  $\nu_{23}$  state. The upper vibrational state was found to be to the first excited vibrational state ( $\nu_6$ ) of the symmetric stretch of C-C while the lower is the coupled state between ring puckering and the C-C asymmetric stretch ( $\nu_{18}+\nu_{24}$ ).

Analysis of the Coriolis interactions described above represents the first time that interactions have been treated in oxetane and that gives an idea about Coriolis interactions among other states in this molecule and can lead to the full assignment of the high resolution infrared spectrum of this molecule. Also, this analysis showed how a very low frequency vibration affects the spectrum of higher frequency vibrations and that tells us what to expect in the spectrum of similar molecules that have low frequency modes.

Furthermore, Coriolis interactions complicate the analysis of high resolution spectra. Therefore, identifying such interactions in molecules will allow a better understanding of them and improve their modeling. As a result, the analysis of high resolution spectra becomes easier or possible for difficult cases.

Although Coriolis interactions introduce challenges for the analysis of the spectrum, they provide more information according to Mills.<sup>17</sup> They provide valuable data for force constant calculations in order to calculate vibrational frequencies using the force field. In addition, Coriolis interactions allow a more complete vibrational assignment by providing information about inactive or undetectable vibrations such as  $\nu_{18}+\nu_{24}$  in this case which was not observed but whose band center is now predicted. Furthermore, these interactions are useful for the determination of the relative signs of the transition moments directly by experiment as they cause specific perturbations in the intensity of the bands which was not discussed in this work.

The ultimate goal is to fully overcome the challenges in the rovibrational assignment and to assign all the transitions in the high resolution infrared spectrum of oxetane. Therefore, the future work is to analyze the remaining untreated Coriolis interactions in this molecule. By doing so, full assignment of the high resolution spectrum of oxetane can be performed which allows for the determination of accurate spectroscopic constants for this molecule.

Although it was performed successfully, analysis of the perturbations described in this work was challenging given the large number of perturbed transitions and congestion of the spectrum. Perturbation problem in other bands needed to be simplified in order to be

solved given the large number of energy levels that are possibly interacting. Recording the spectrum at low temperature reduces the population of the ring puckering excited states but this would not significantly simplify the problem. If the spectrum were to be recorded at 230 K, the theoretical population of the first ring puckering excited state would be reduced from 0.77 at 300 K to 0.72 at 230 K relative to the ground vibrational state. The best way forward is likely to automate the assignment using computer algorithms as was recently tried for the assignment of a band of trimethylene sulfide.<sup>18</sup> At present, this technique does not incorporate Coriolis interactions but the present analysis for oxetane would provide a good test system.

Inconsistencies between the quantum mechanical calculations show that standard theory breaks down in the description of the normal modes of oxetane. This brings to the surface the necessity of finding reliable models that account for the complications caused by large amplitude motions in oxetane and other floppy molecules.

## References

- (1) Zürcher, R.F; Günthard, H.H. *Helv. Chim. Acta.* **1955**, *38*, 849.
- (2) Danti, A.; Lafferty, W. J.; Lord, R.C. *J. Chem. Phys.* **1960**, *33*, 294.
- (3) Chan, S.I.; Borgers, T.R.; Russell, J.W.; Strauss, H.L; Gwinn. W.D. *J. Chem. Phys.* **1966**, *44*, 1103.
- (4) Ueda, T.; Shimanouchi, T. *J. Chem. Phys.* **1967**, *47*, 5018.
- (5) Green, W.H. *J. Chem. Phys.* **1970**, *52*, 2156.
- (6) Wieser, H.; Danyluk, M. *Can. J. Chem.* **1972**, *50*, 2761.
- (7) Wieser, H.; Danyluk, M.; Kydd, R.A. *J. Mol. Spectrosc.* **1972**, *43*, 382.
- (8) Jokisaari, J.; Kauppinen, J. *J. Chem. Phys.* **1973**, *59*, 2260.
- (9) Wieser, H.; Danyluk, M.; Kydd, R.A.; Kiefer, W.; Bernstein, H.J. *J. Chem. Phys.* **1974**, *61*, 4380.
- (10) Kydd, R.A.; Wieser, H.; Kiefer, W. *Spectrochim. Acta.* **1983**, *39A*, 173.
- (11) Lesarri, A.; Blanco, S.; Lopez, J.C. *J. Mol. Struct.* **1995**, *354*, 237.
- (12) Turnbull, D.M.; Sowa, M.G.; Henry, B.R. *J. Phys. Chem.* **1996**, *100*, 13433.
- (13) Winnewisser, M.; Kunzmann, M.; Winnewisser, B. *J. Mol. Spectrosc.* **2001**, *561*, 152.
- (14) Moruzzi, G.; Kunzmann, M.; Winnewisser, B. ; Winnewisser, M. *J. Mol. Spectrosc.* **2003**, *219*, 152.
- (15) Kydd, R.A.; Wieser, H.; Danyluk, M. *J. Mol. Spectrosc.* **1972**, *44*, 14.
- (16) Banhegyi, G.; Play, P.; Fogarasi, G. *Spectrochim. Acta.* **1983**, *39A*, 761.
- (17) Mills, I.M. *Pure Appl. Chem.* **1965**, *11*, 325.
- (18) van Wijngaarden, J.; Desmond, D.; Meerts, W.L. *J. Mol. Spectrosc.* **2015**, *315*, 107.